Title
Synthesis and Characterization of Rare-Earth Tellurides and Their Composites For High-Temperature Thermoelectric Applications

Author
Cheikh, Dean

Publication Date
2017

Peer reviewed|Thesis/dissertation

UNIVERSITY OF CALIFORNIA

Los Angeles

Synthesis and Characterization of Rare-Earth Tellurides and Their Composites For High-Temperature Thermoelectric Applications

A dissertation submitted in partial satisfaction of the

requirements for the degree Doctor of Philosophy

in Materials Science and Engineering

by

Dean Cheikh

2017

ABSTRACT OF THE DISSERTATION

Synthesis and Characterization of Rare-Earth Tellurides and Their Composites

For High-Temperature Thermoelectric Applications

by

Dean Cheikh

Doctor of Philosophy in Materials Science and Engineering

University of California, Los Angeles, 2017

Professor Bruce S. Dunn, Chair

Radioisotope thermoelectric generators (RTGs) are solid-state energy conversion devices and have been a vital power generation technology for deep space missions conducted by the National Aeronautics and Space Administration (NASA). At the heart of these generators are thermoelectric materials that convert heat given off by a radioisotope decay into electricity through the Seebeck effect. While these systems have demonstrated long-term reliability, the current state-of-practice materials have thermoelectric figures of merit, *ZT*, near 1, leading to low system level efficiencies of ~6.5%. The figure of merit is defined as $ZT = \frac{\sigma S^2}{\kappa} T$ where σ, S, κ, and T are electrical conductivity, Seebeck coefficient, thermal conductivity, and temperature, respectively. Development of higher *ZT* materials would enable future NASA missions to perform a greater number of scientific experiments and extend mission lifetimes.

Lanthanum telluride ($La_{3-x}Te_4$) is a state-of-the-art *n*-type high-temperature thermoelectric material, with a *ZT* of 1.1 at 1275 K. It has been demonstrated that the electrical resistivity and Seebeck coefficient of this material can be decoupled when nickel inclusions are added to form a composite. This new phenomenon, known as composite assisted funneling of electrons (CAFE), allows for the resistivity of the composite to decrease while leaving the Seebeck coefficient unaffected when 12-15 vol% nickel was incorporated.

The initial work presented in this dissertation focused on microstructural modifications to $La_{3-x}Te_4$-Ni composites to attain a better understanding of the CAFE mechanism. This investigation was conducted by varying the size of the nickel particles compared to what were used in the previous composite study. A 60% increase in *ZT* to a value of 1.9 at 1200 K for the composites with the smallest Ni particle size was obtained due to an increased Seebeck coefficient and decreased thermal conductivity.

The next study focused on the extension of the CAFE effect in $La_{3-x}Te_4$ to use inclusions other than nickel. Cobalt of a similar size to the nickel in the initial $La_{3-x}Te_4$-Ni composite work was used. A series of $La_{3-x}Te_4$-Co composites were synthesized and their thermoelectric properties characterized. A gradual decrease in resistivity was observed above 8 vol% cobalt, suggesting the CAFE mechanism was occurring. An 18% increase to the Seebeck coefficient was observed between 5-8 vol% cobalt, likely due to contamination on the cobalt powder, altering the carrier concentration of the matrix. The increase to the Seebeck coefficient allowed for a *ZT* of 1.5 at 1225 K to be achieved at 5 vol% cobalt.

The final investigation in this dissertation focused on the synthesis and thermoelectric characterization of praseodymium telluride ($Pr_{3-x}Te_4$). Density functional theory (DFT)

calculations predicted a large peak in the density of states (DOS) of $Pr_{3-x}Te_4$ at its Fermi level compared to $La_{3-x}Te_4$, due to the *4f* electrons of praseodymium. This change in the band structure was predicted to increase the Seebeck coefficient of $Pr_{3-x}Te_4$ over $La_{3-x}Te_4$. A series of $Pr_{3-x}Te_4$ with varying vacancy concentrations were mechanochemically synthesized and characterized. A 25% improvement in the Seebeck coefficient and 25% decrease in the thermal conductivity compared to $La_{3-x}Te_4$ was observed. The thermoelectric properties were found to optimize at a composition of $Pr_{2.74}Te_4$, reaching a *ZT* of 1.7 at 1200 K.

The dissertation of Dean Cheikh is approved.

Sabah K. Bux

Richard B. Kaner

Jaime Marian

Y. Sungtaek Ju

Bruce S. Dunn, Committee Chair

University of California, Los Angeles

2017

Ad astra

Table of Contents

List of Figures

List of Tables

Acknowledgements

It takes a village to make a scientist and I have been fortunate to be a part of two world-class institutions, UCLA and JPL, during my graduate work. I would first like to thank Professor Bruce Dunn for the opportunity to complete my degree under his supervision. His mentorship, encouragement, and scientific rigor are all things I have benefitted from greatly. Next I thank Dr. Sabah Bux at JPL for taking me on as a graduate student, her constant support in and outside of lab, and her friendship. The many patient hours she spent teaching me and high expectations have forged me in to the researcher I am today. No graduate student has had better advisors.

I thank Dr. Jean-Pierre Fleurial for his input to this work and allowing me to break things in his lab. His unparalleled expertise and chemical intuition have been invaluable to the completion of this work. I would also like to thank my committee members Professors Richard Kaner, Jaime Marian, and Sungtaek Ju for their critiques and recommendations.

Many thanks to my predecessor Dr. James Ma for his input to the composite portion of this work and for being a friend over the years. The skills I acquired under your supervision were essential to synthesizing these challenging materials, and your intermittent existential crises always made me always question what it means to make a measurement.

Special thanks to Dr. Kathleen Lee for her contributions to all things X-ray related in this work, editorial skills, and phenomenal baked goods. I am truly grateful for her patience in teaching me Rietveld analysis and tolerating my shenanigans.

Brea Hogan and Steven Gomez deserve recognition for their contributions to the rare-earth telluride portion of this work, and for being exemplary undergraduate students. It was

always a struggle finding enough work to keep them busy in lab and I have grown as a mentor trying to keep up with both of you.

This work was carried out at JPL and I am grateful for all those who have aided me through this endeavor. Many thanks to George Nakatsukasa for sharing his vast knowledge of equipment, always having the right tool when I needed it, and early morning Corvette videos. I thank Dr. Trinh Vo and Dr. Paul von Allmen for the computational modelling presented in this work. I would like to acknowledge Dr. Pawan Gogna and Greg Gerig for their assistance with high temperature measurements. Thank you to Dr. Chi Ma for his aid with EMPA and SEM. I thank Dr. Fivos Drymiotis, Dr. Kurt Star, Prof. Eric Toberer at the Colorado School of Mines, Prof. Alexandra Zevalkink at Michigan State, Prof. Susan Kauzlarich at UC Davis, Prof. Shahab Derakhshan at CSULB, Prof. Jeff Snyder at Northwestern, and Dr. Christofer Whiting at UDRI for their numerous forms of assistance and making group meetings enjoyable. Thanks to Imperial Overlord Dr. Bryan Mcenerney for his various forms of support and mentorship. Thank you to Dr. Chris Turner for his SPS input and frequent car related escapades. To Caitlin, Kevin, Jen, Brian, Ike, Billy, Sutinee, Coney, Francisco, Tom, and Maggie, thank you all for making the lab a more lively place.

UCLA has been my home for nearly a decade and I have been fortunate to cross paths with many extraordinary people there. I would like to thank the members of Professor Dunn's lab for their help over the years. I thank Dr. Jesse Ko for getting me started in the Dunn Lab, being a model graduate student, and being a friend. Thank you to Dr. Esther Lan for your kind suggestions and keeping the lab paperwork streamlined. To the former Dunn Lab members, Dr. Danielle Casillas, Dr. Dan Wilkinson, Dr. Jimmy Kim, Dr. Leland Smith, Dr. Rita Blaik, Dr. Daniel Membrano, Dr. Ryan Maloney, Dr. Janet Hur, Dr. Guillaume Muller, Dr. Xavier

Petrissans Dr. Wade Richarson, Dr. Steve Jonas and Prof. Vicky Doan-Nguyen, thank you for all your help and insights. To the current members of Dunn Lab, Jon “PKLA” Lau, Ryan “Pickle” DeBlock, David “The Gorilla” Ashby, Danielle Butts, Chris Choi, Dr. Matt Lai, and Dr. Quilong Wei, I thank you for the helpful scientific discussions, camaraderie, and great memories. I am grateful for the other friendships I have made or maintained throughout my graduate degree. Jose, Ryan, Phil, Blaire, Brett, Mark, Tait, Terri, Elliot, Carrie, Mitch, Dave, Heinz, Keren, Sean, Cory, Dan, and Gary, thank you for all the good times.

I reserve the greatest thanks for my family. To Mohamed, Alexander, Nina, Hemi, and my parents, thank you for always being there for me and keeping me grounded. To the rest of the family, thank you all for your support.

Chapter 4 presents material based on the work “Praseodymium Telluride: A High-Temperature, High *ZT* Thermoelectric Material”, which is currently under peer review for publication. It was co-authored with Brea Hogan who performed synthesis and characterization, Dr. Trinh Vo and Dr. Paul von Allmen who performed all DFT calculations and computational modelling, Dr. Kathleen Lee who provided technical discussion, performed XRD and aided with Rietveld refinement, David Smiadak and Prof. Alexandra Zevalkink who performed RUS measurements and analysis, and Prof. Bruce Dunn, Dr. Jean-Pierre Fleurial and Dr. Sabah Bux were co-principle investigators. I performed synthesis, characterization and Rietveld analysis.

This work was performed at the California Institute of Technology/Jet Propulsion Laboratory under contract with the National Aeronautics and Space Administration. This work was supported by the NASA Science Missions Directorate under the Radioisotope Power Systems Program’s Thermoelectric Technology Development Project.

VITA

2013	Bachelor of Science, Materials Engineering *University of California, Los Angeles*
2013-2017	Graduate Student Researcher Department of Materials Science and Engineering *University of California, Los Angeles*
2013-2017	Graduate Student Researcher Thermal Energy Conversion Research and Advancement Group *NASA Jet Propulsion Laboratory*
2015	Master of Science, Materials Science and Engineering *University of California, Los Angeles*

Publications and Presentations

D. Cheikh, B. E. Hogan, T. Vo, P. von Allmen, K. Lee, D. Smiadak, A. Zevalkink, B. S. Dunn, J.-P. Fleurial, and S. K. Bux, "Praseodymium Telluride: A High-Temperature, High *ZT* Thermoelectric Material" (2017) *Manuscript Submitted*

D. Cheikh, B. E. Hogan, T. Vo, P. von Allmen, B. S. Dunn, J.-P. Fleurial, and S. K. Bux, "Vacancy Controlled Thermoelectric Performance of Mechanochemically Synthesized $Pr_{3-x}Te_4$" 2017 North American Solid State Chemistry Conference, Goleta, California (Oral Presentation)

D. Cheikh, J. M. Ma, P. von Allmen, T. Vo, B. S. Dunn, J.-P. Fleurial, and S. K. Bux, "*ZT* Enhancement in Transition Metal Composited $La_{3-x}Te_4$ via Composite Assisted Funneling of Electrons" 2017 International Conference on Thermoelectrics, Pasadena, California (Poster Presentation)

B. E. Hogan, D. Cheikh, T. Vo, P. von Allmen, B. S. Dunn, J.-P. Fleurial, and S. K. Bux "Low-Temperature Synthesis and Thermoelectric Performance of Praseodymium Telluride, Pr_3Te_4, Series" 2017 International Conference on Thermoelectrics, Pasadena, California (Poster Presentation)

C. Whiting, T. Vo, S. Bux, and D. Cheikh "Actinide Based Thermoelectrics – Standing Up a Facility to Process Depleted Uranium into Thermoelectric Materials" 2017 International Conference on Thermoelectrics, Pasadena, California (Poster Presentation)

D. Cheikh, S. K. Bux, J. M. Ma, P. Von Allmen, T. Vo, J.-P. Fleurial, and B. S. Dunn, "Improved Composite Assisted Funneling of Electrons in Nickel Composited $La_{3-x}Te_4$ via Particle Size Reduction," 2017 Nuclear and Emerging Technologies for Space conference, Orlando, Florida (Oral Presentation)

D. Cheikh, J. M. Ma, P. Von Allmen, T. Vo, S. K. Bux, J.-P. Fleurial, and B. S. Dunn, "Impact of Microstructure on Composite Assisted Funneling of Electrons in Nickel Composited $La_{3-x}Te_4$." 2015 Fall Materials Research Society conference, Boston, Massachusetts (Oral Presentation)

Chapter 1: Introduction to Thermoelectric Materials and Applications

1.1. Fundamentals of Thermoelectric Materials

Thermoelectric materials are solid-state energy conversion devices that convert thermal energy into electricity or vice versa. Conversion of heat to electricity, which utilizes the Seebeck effect, occurs when a temperature gradient is applied to a material and the subsequent thermal diffusion of charge carriers generates a voltage across the material. The converse approach leads to the creation of a temperature gradient from an applied electric potential, known as the Peltier effect. These energy conversion characteristics have made thermoelectric materials attractive for potential use in applications such as waste heat recovery in automobiles and power plants, cooling for microelectronics, and wine coolers.[1-3]

Thermoelectric devices utilize the configurations shown in Figure 1.1 for power generation or heating and cooling. To maximize efficiency, *n*-type and *p*-type legs are placed electrically in series and thermally in parallel. For power generation, majority charge carriers are thermally excited at the hot side and then diffuse to the cold side. When connected to a load, a current is produced and can be used to perform electrical work. Conversely, in the heating/cooling configuration, an electric potential is applied to the segments and the charge carriers pump heat from one side of the couple to the other.

Thermoelectric generators (TEGs) utilize thermoelectric devices in the power generation configuration to convert heat to electricity. The electrical efficiency of a TEG (η_e) is given by:

$$\eta_e = \frac{I(S\Delta T - IR_L)}{IST_h + \kappa\Delta T - 0.5I^2R_i} \tag{1.1}$$

where I is current, S is the Seebeck coefficient, T_{hot} is the temperature of the hot side, ΔT is the temperature difference between the hot and cold side, R_L is the load connected to the TEG, κ is thermal conductivity, and R_i is the internal resistance of the legs.

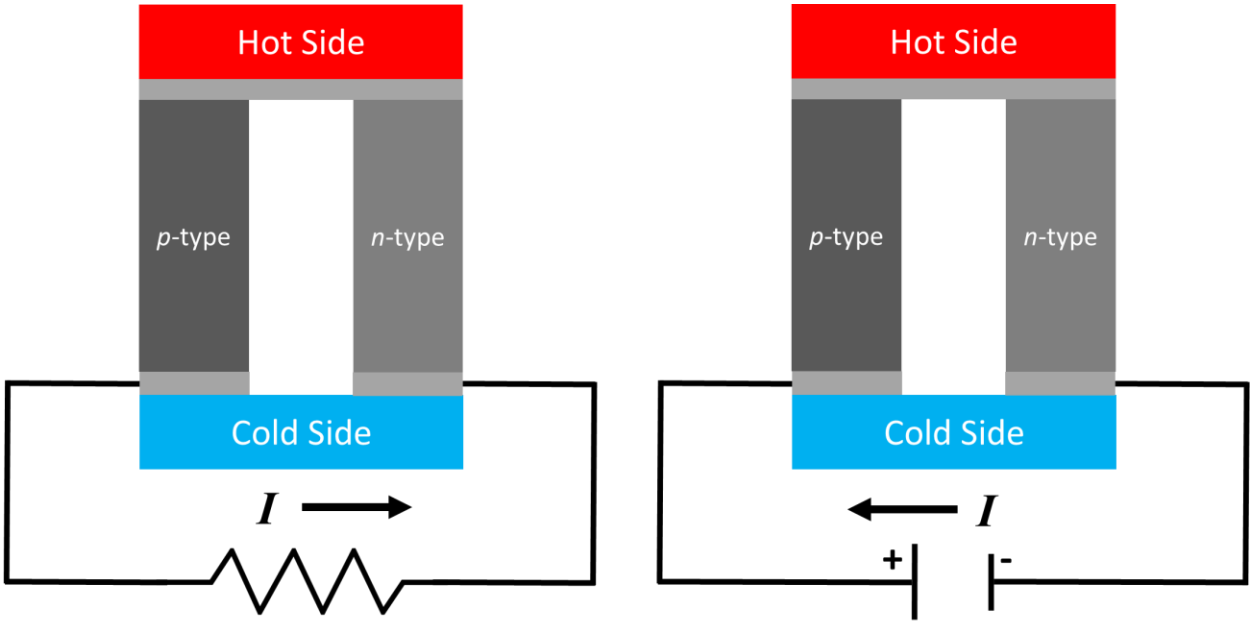

Figure 1.1 Schematic of typical thermoelectric couples with *n*-type and *p*-type segments in configurations for power generation (left) and heating/cooling (right).

The power output (P) of a TEG is also given by:

$$P = \frac{S\Delta T^2 R_L}{(R_i+R_L)^2} \tag{1.2}$$

From Equation 1.2, the power output is maximized when the internal resistance is made to match the load connected to the TEG. When this condition is imposed on Equation 1.1, the maximum efficiency of a TEG is given by:

$$\eta_{max} = \frac{T_{hot} - T_{cold}}{T_{hot}} \frac{\sqrt{1+ZT}-1}{\sqrt{1+ZT}+\frac{T_{cold}}{T_{hot}}} \tag{1.3}$$

ZT is known as the thermoelectric dimensionless figure of merit and is defined as:

$$ZT = \frac{\sigma S^2}{\kappa} T \tag{1.4}$$

where σ is the electrical conductivity. The device efficiency with a cold side temperature of 300 K is plotted in Figure 1.2 for a various *ZT* values. It can be seen that η increases with *ZT* and as *ZT* goes to infinity, the device efficiency approaches the Carnot efficiency.

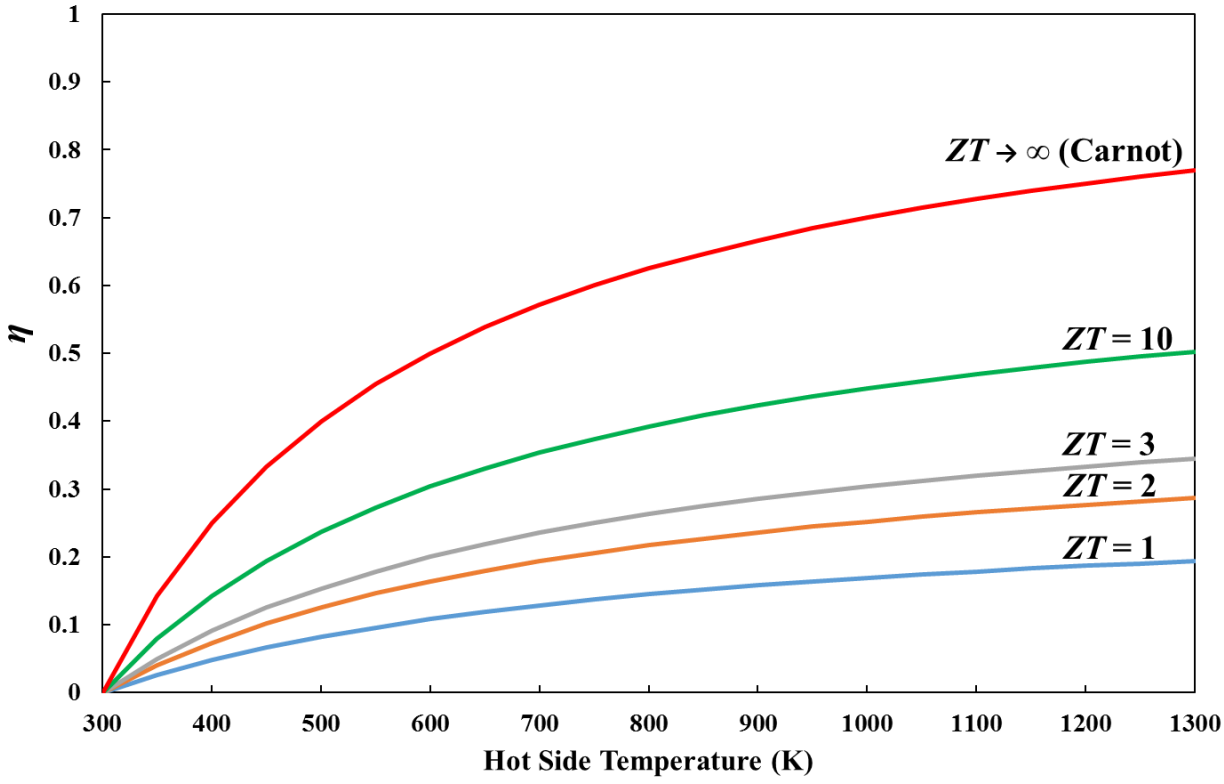

Figure 1.2 Thermoelectric device efficiency as a function of hot side temperature for several values of *ZT*. The cold side temperature is 300 K. *ZT* = ∞ corresponds to the Carnot efficiency.

In order to increase the total device efficiency, *ZT* must be increased or the Carnot efficiency must be increased (Equation 1.3). Increasing the Carnot efficiency is challenging due to practical constraints on TEGs, e.g., limits to the operating temperatures of the hot and cold sides and material constraints due to melting or decomposition temperatures of the thermoelectric materials. It should also be noted that η is dependent on the average values of *ZT* between T_{hot} and T_{cold} for both *p*- and *n*-type legs, not the peak *ZT* values.

Increasing *ZT* is also challenging since the variables that comprise *ZT* are coupled, and a change in one variable will often adversely affect another (Equation 1.4).[5-7] This is due to the dependency of the electronic terms, σ, *S*, and the thermal transport component, κ, on the carrier concentration of the material. The electrical conductivity of a material will generally increase linearly with the carrier concentration:

$$\sigma = \frac{1}{\rho} = ne\mu \tag{1.5}$$

where ρ is the electrical resistivity, *n* is carrier concentration, *e* is fundamental charge of an electron, and μ is the mobility of the charge carriers. Conversely, increasing the carrier concentration of the material will result in a decrease in the Seebeck coefficient. The Mott formula can be used to model the Seebeck coefficient of metals and is given by:

$$S = \frac{2k_B^2 m^* T}{3e\hbar^2}\left(\frac{\pi}{3n}\right)^{\frac{2}{3}} \tag{1.6}$$

where k_B is the Boltzmann constant, m^* is the effective mass of the charge carrier, and $\hbar$ is the reduced Planck constant.[8] Increasing the carrier concentration will simultaneously increase the electronic contribution to the thermal conductivity. The total thermal conductivity is the sum of

the lattice contribution, κ_L, and the heat carried by electrons, κ_e.[5] The electronic contribution to thermal conductivity can be estimated using the Wiedemann-Franz law:

$$\kappa_e = L\sigma T = ne\mu LT \tag{1.7}$$

where L is the Lorenz number which is dependent on the Fermi level and can range from 1.5-2.6 x 10^{-8} $\frac{W\Omega}{K^2}$.[9] As a result of these competing effects, the ZT for any given material system will have a peak value at an optimum carrier concentration. For many systems, the optimal carrier concentration is in the degenerate semiconductor range of 10^{19} – 10^{21} cm^{-3} (Figure 1.3).[1,5] For these reasons, there has been much interest in degenerate semiconductors, which can be doped to adjust their carrier concentrations.[5,6,10]

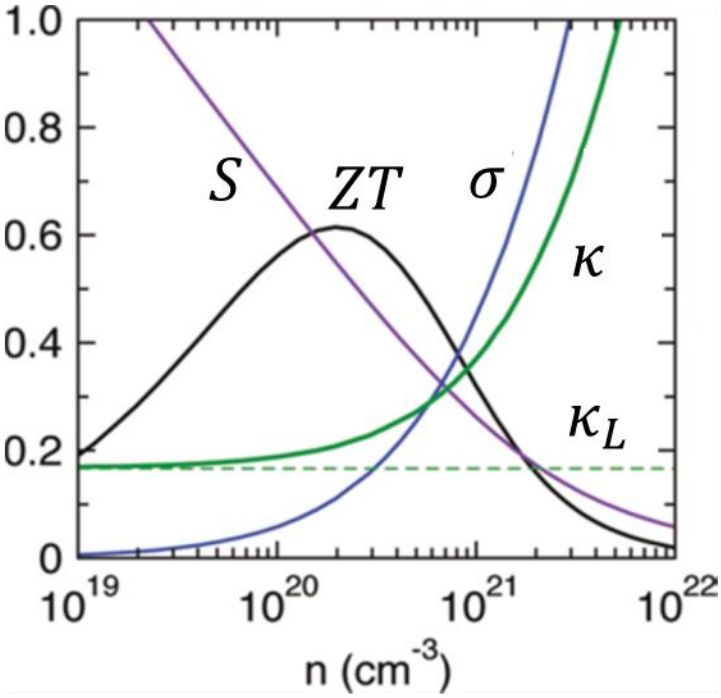

Figure 1.3 Dependence of thermoelectric properties on carrier concentration, n.[6]

1.2. Heritage of Thermoelectrics in Space

Radioisotope thermoelectric generators (RTGs) utilize thermoelectric materials to convert heat produced from a decaying isotope into electrical power. They have been used on 18 NASA missions over the last 50 years without failure. Typically, RTGs are used on missons where photovoltaics or electrochemical systems are not feasible due to lack of solar flux, long mission lifetimes, environments with day/night cycles, or where settling dust could impair the effectiveness of solar cells. RTGs are all solid-state devices and, as a result, are incredibly reliable due to a high level of redundancy and lack of moving parts. The long lifetimes of RTGs are evidenced by the Voyager 1 and 2 missions, which have been operating continuously for 40 years.[11] As future missions of the National Aeronautics and Space Administration (NASA) are targeting longer mission durations, larger scientific payloads, and worlds with more extreme environments, improvements to RTG technology is vital for the future of space exploration.

1.3. State-of-The-Art High Temperature Thermoelectric Materials

Historically, materials that have been at the heart of all of the RTGs for the past 50 years have been *n*- and *p*-type $Si_{1-x}Ge_x$, *n*-type PbTe, *p*-type PbSnTe, or *p*-type Te-Ag-Ge-Sb (TAGS).[4, 12, 13] While these materials have demonstrated high reliability, a limiting factor of these systems is that they exhibit low thermal-to-electrical conversion efficiency, with beginning-of-life (BOL) RTG efficiencies between 3-7%.[12,14] Increasing the efficiencies of the thermoelectric materials used in RTGs is critical for future deep space exploration, as it would allow for larger scientific payloads, decrease the amount of limited radioisotope fuel used, and reduce the weight of future RTGs for a given power output.

Figure 1.4 shows *ZT* as a function of temperature for the current state-of-the-art materials under investigation by the Thermal Energy Conversion Research and Advancement Group at the Jet Propulsion Laboratory. It can be seen that the heritage RTG materials have average *ZT* values significantly lower that 1 (approximately 0.80 for PbTe/TAGS across a 811 K-483K temperature range and 0.55 for Si-Ge alloys over a 1273 K-573 K temperature range). However, there have been several materials recently identified which have *ZT* values well over 1, with some reaching 1.6.[12]

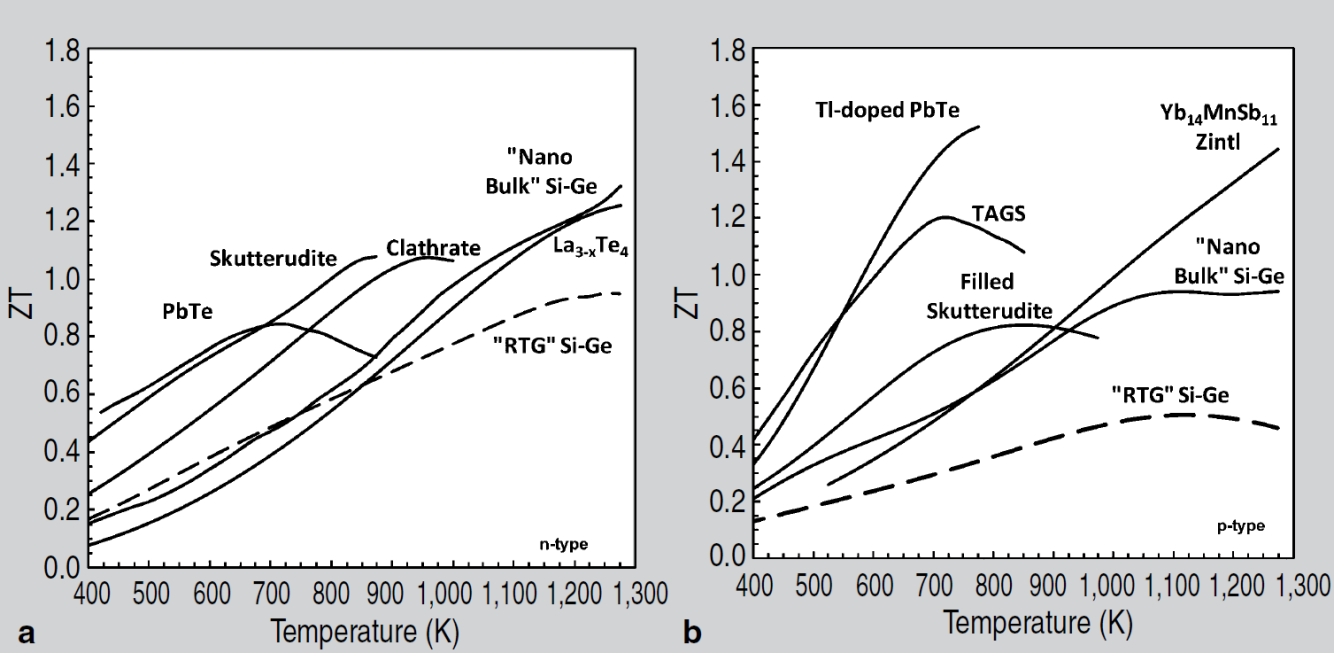

Figure 1.4 *ZT* values for current state-of-the-art (a) *n*-type and (b) *p*-type bulk thermoelectric materials under investigation at the Jet Propulsion Laboratory.[12]

Materials with large *ZT*s in the high temperature regime fall into one of two materials selection strategies. The first is to identify materials with complex crystal structures so they have inherently low lattice thermal conductivities. $Yb_{14}MnSb_{11}$ and $La_{3-x}Te_4$ exemplify this as their thermal conductivities are approximately 0.7 and 2 $Wm^{-1}K^{-1}$ at at room temperature,

respectively.[15,16] Their low thermal conductivities, in addition to their desirable electronic properties, result in some of the highest *ZT* values reported for bulk materials. The second material selection strategy is to identify thermoelectric materials with desirable electronic properties and then modify the microstructure to reduce the thermal conductivity. This strategy was employed on $Si_{1-x}Ge_x$ alloys, where the size of the grains in the alloy was reduced by extended ball milling to lower the thermal conductivity.[17,18] The result was a 250% increase in *ZT* when compared to heritage $Si_{1-x}Ge_x$.

1.4. $La_{3-x}Te_4$ as a Thermoelectric Material

Lanthanum telluride ($La_{3-x}Te_4$) is a state-of-the-art high-temperature, *n*-type thermoelectric material, which possesses a peak *ZT* of 1.1 at 1275 K at the optimal vacancy concentration of $x = 0.23$.[16] $La_{3-x}Te_4$ material exists in the Th_3P_4 structure type, contains 28 atoms per unit cell ($Z = 4$), and have Te atoms inside distorted octahedra of La atoms (Figure 1.5). $La_{3-x}Te_4$ has a defect structure, which is able to accommodate vacancies on the rare earth site, where up to one of every nine La atoms may be absent. The complexity of the crystal structure leads to a intrinsically low thermal conductivity values in the range of of 1-2 $Wm^{-1}K^{-1}$ at room temperature depending on the vacancy concentration.[19] The carrier concentration of this system is controlled by the number of cation vacancies and is given by:

$$n = n_{max}(1 - 3x) \tag{1.8}$$

where n_{max} is 4.5 x 10^{21} cm^{-3}. As a result of this dependence, the system can be doped to optimize its electronic properties.[15] When $x = 0$ (La_3Te_4), the material behaves as a degenerate semiconductor and the electronic properties are metallic in nature with respect to temperature. When $x = 0.33$ ($La_{2.667}Te_4$, also written as La_2Te_3 or $LaTe_{1.5}$), the material acts as an intrinsic

semiconductor. The optimized defect stoichiometry to attain the maximum ZT = 1.1 occurs when x = 0.23 ($LaTe_{1.46}$).[16] This makes $La_{3-x}Te_4$ one of the highest performance *n*-type materials in the temperature range between 1273 K-800 K.[12]

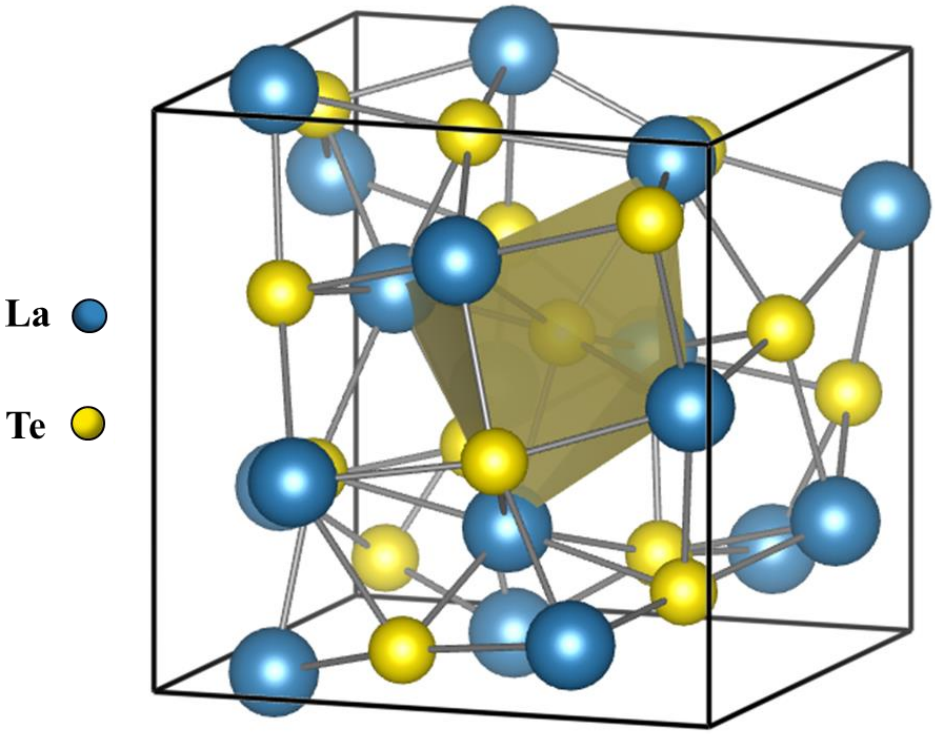

Figure 1.5 Crystal structure of La_3Te_4. Lanthanum atoms are represented in blue and tellurium atoms by yellow. The tellurium atoms sit inside distorted octahedra of lanthanum atoms.

$La_{3-x}Te_4$ and other rare-earth chalcogenides were initially challenging to synthesize with reproducible results due to the use of melt syntheses or solid-state reactions.[20-23] The large differences in melting points between tellurium and lanthanum, 722 K and 1193 K respectively, would lead to loss of tellurium into the vapor phase, altering the stoichiometry of the products. Additionally, oxidation of lanthanum and $La_{3-x}Te_4$ was problematic, especially at the elevated

processing temperatures. These processing issues were circumvented through the application of powder metallurgy techniques to synthesize and compact $La_{3-x}Te_4$.[16]

1.5. Dissertation Objectives

The research presented in this dissertation is focused on the thermoelectric characterization of four rare-earth chalcogenide systems. The first is the $La_{3-x}Te_4$-Ni system. The influence of Ni morphology on the composite assisted funneling of electrons (CAFE) mechanism was studied. This was performed by using Ni particles of varying sizes compared to the previous inclusion size used during discovery of this phenomenon. The impact of these altered microstructures on the materials' thermoelectric properties was investigated.

Second, in an effort to observe if the CAFE mechanism could be utilized with inclusions other than nickel, the $La_{3-x}Te_4$-Co system was also investigated. Cobalt, with similar starting size and morphology to the previous $La_{3-x}Te_4$-Ni work, was used and a series of composites were made with similar loading fractions to the initial $La_{3-x}Te_4$-Ni study. The thermoelectric properties of these composites were measured.

Finally, evaluation of rare-earth chalcogenides where lanthanum was not a constituent was also performed, specifically the thermoelectric characterization of $Pr_{3-x}Te_4$. This work was motivated by theoretical calculations, which predict an increased Seebeck coefficient due to introduction of additional states near the Fermi level from the *4f* electrons of praseodymium. $Pr_{3-x}Te_4$ compacts with various vacancy concentrations were prepared via mechanochemical synthesis and their properties were measured.

1.6. References

[1] D. M. Rowe, *CRC Handbook of Thermoelectric Materials*, CRC Press, 1995

[2] F. J. DiSalvo, *Science*, **1999**, *285*, 703.

[3] J-P. Fleurial, A. Borshchevsky, and T. Caillat, *AIP Conference Preceedings*, **1997** *387*, 293.

[4] C. Wood, *Reports on the Progress of Physics*, **1988**, *51*, 459.

[5] G. J. Snyder and E. S. Toberer, *Nature Materials*, **2008**, *7*, 105.

[6] E. S. Toberer, A. F. May, G. J. Snyder, *Chem. Mater.*, **2010**, *22*, 624.

[7] S. K. Bux, J-P. Fleurial, and R. B. Kaner, *Chem. Comm.*, **2010**, 46, 8311.

[8] M. Cutler, J. F. Leavy, and R. L. Fitzpatrick, *Phys. Rev.*, **1964**, *133*, A1143.

[9] A. J. Minnich, M. S. Dresselhaus, Z. F. Ren, and G. Chen, *Energy Environ. Sci.*, **2009**, *2*, 466.

[10] S. R. Brown, S. M. Kauzalrich, F. Gascoin, G.J. Synder, *Chem. Mater.*, **2006**, *18*, 1873.

[11] A. Angrum, NASA and JPL website, Voyager spacecraft lifetime summary, http://voyager.jpl.nasa.gov/spacecraft/spacecraftlife.html (Accessed September 2017).

[12] J.-P. Fleurial, *Journal of the Mineral*, **2009**, *61*, 79

[13] J. Yang and T. Caillat, *MRS Bulletin*, **2006**, *31*, 224.

[14] C. B. Vining and J-P. Fleurial, *A Critical Review of Space Nuclear Power and Propulsion 1984-1993*, ed. M. El-Genk (New York: AIP, 1994), **1993**, 87.

[15] S. R. Brown, S. M. Kauzalrich, F. Gascoin, and G.J. Synder, *Chem. Mater.*, **2006**, *18*, 1873.

[16] A. F. May, J.-P. Fleurial, and G. J. Snyder, *Phys. Rev. B*, **2008**, *78*, 125205.

[17] S. Bux, J. P. Fleurial, R. Blair, P. Gogna, T. Caillat and R. Kaner, in Materials Research Society Spring 2009 Meeting, ed. J. Yang, G. S. Nolas, K. Koumoto and Y. Grin, Materials Research Society, San Francisco, CA, **2009**, 1166-N1102.

[18] S. K. Bux, R. G. Blair, P. K. Gogna, H. Lee, G. Chen, M. S. Dresselhaus, R. B. Kaner and J.-P. Fleurial, *Adv. Funct. Mater.*, **2009**, 19, 2445.

[19] J. M. Ma, *Improving the Mechanical Strength and Power Conversion Efficiency of High Temperature Thermoelectrics*, Doctoral Dissertation, University of California, Los Angeles, **2014**

[20] K. A. Gschneidner, J. F. Nakahara, B. J. Beaudry, and T. Takeshita, *Mat. Res. Soc. Symp. Proc.*, **1987**, *97*, 359.

[21] L. R. Danielson, V. Raag, and C. Wood, in *Intersociety Energy Conversion Engineering Conference*, Miami, FL, **1985**, 531.

[22] A. A. Eliseev, E. I. Yarembash, Y. G. Kuznetsov, E. S. Vigileva, A. A. Reshchikova, and L. I. Anotonoa, *Russ. J. Inorg. Chem.*, **1964**, *9*, 482.

[23] T. H. Ramsey, H. Steinfink, and E. J. Weiss, Inorg. Chem.**, 1965**, *4*, 1154.

Chapter 2: *ZT* Enhancement in $La_{3-x}Te_4$-Ni Composites via Particle Size Reduction

2.1. Introduction to Composite Assisted Funneling of Electrons in $La_{3-x}Te_4$-Ni Composites

The thermal-to-electrical conversion efficiency of thermoelectric materials is determined by the temperature gradient across the material, ΔT, and the dimensionless thermoelectric figure of merit, $ZT = S^2T/\rho\kappa$. Therefore, to improve the efficiencies of these materials, the Seebeck coefficient must be increased or the electrical resistivity and thermal conductivity must decrease. As discussed in Chapter 1, exclusively changing one property favorably is challenging due to the dependency of S, ρ, and κ on the material's carrier concentration. Consequently, a positive change in one property will often detrimentally affect another.[1]

One strategy to circumvent the issue of coupled transport properties is to fabricate composite materials that have desirable properties. The ideal thermoelectric material is said to have properties of a "phonon glass electron crystal" having the low thermal conductivity of a glass, the electrical conductivity of a metal, and the Seebeck coefficient of an insulator. [1-4] From a practical standpoint, it is often challenging to fabricate composite materials in such a way that their properties combine in a favorable manner. Additionally, reactions between inclusions and the matrix or growth of the inclusion phase are of concern due to the elevated working temperatures and long-term operation of the materials.[5]

It is still of interest to identify composite systems which avoid these issues of particle coarsening and reactions between the matrix and inclusion. However, one hurdle is that previous modelling of isotropic composite systems using effective medium theory has determined that the *ZT* of the composite cannot be greater than the individual *ZT* values of any of the constituent phases.[6] Subsequent calculations predicted that while *ZT* cannot be improved, the power factor,

σS^2, of a composite can theoretically be improved using tailored inclusion geometries, such as parallel rods or core shell particles.[7]

Despite these theoretical limitations, a large amount of experimental research has still been conducted on compositing thermoelectric materials to improve their properties.[8-11] Selection of inclusion and matrix materials typically utilize one of two strategies. The first is to reduce the thermal conductivity of the composite through the addition of inclusions which promote phonon scattering.[8,9] Inclusions are typically chosen such that they have thermal conductivities significantly lower than the matrix material in order to minimize the thermal conductivity of the composite while maximizing the differences in thermal conductivity to enhance phonon scattering. However, the inclusions will also increase electron scattering and lead to increased electrical resistivity. A second strategy is to add conductive particles to reduce the electrical resistivity of the composite. While the resistivity can be decreased through this method, the Seebeck coefficient and thermal conductivity are adversely affected and no gain in *ZT* is observed.[10,11]

Previous research performed at the Jet Propulsion Laboratory had investigated compositing 2.2-3 μm Ni particles with a $La_{3-x}Te_4$ matrix in order to improve the mechanical robustness of the material.[5,12] While the Ni particles were found to improve the fracture toughness of the composites, it was also found that the Seebeck coefficient and electrical resistivity were decoupled for samples with 12-15% Ni loading in a $LaTe_{1.46}$ matrix.[5] The electrical resistivities of the composites remain invariant up to 10 vol% Ni, after which it decreases (Figure 2.1(a)). The Seebeck coefficients of the composites remain unchanged until above 15 vol% loading (Figure 2.1(b)). However, the thermal conductivity begins to increase in composites with Ni loadings greater than 5 vol% (Figure 2.1(c)). As a result, the *ZT* of the

$LaTe_{1.46}$-Ni composites remain at approximately 1.2 until the Ni loading fraction is increased above 15 vol% (Figure 2.1(d)).

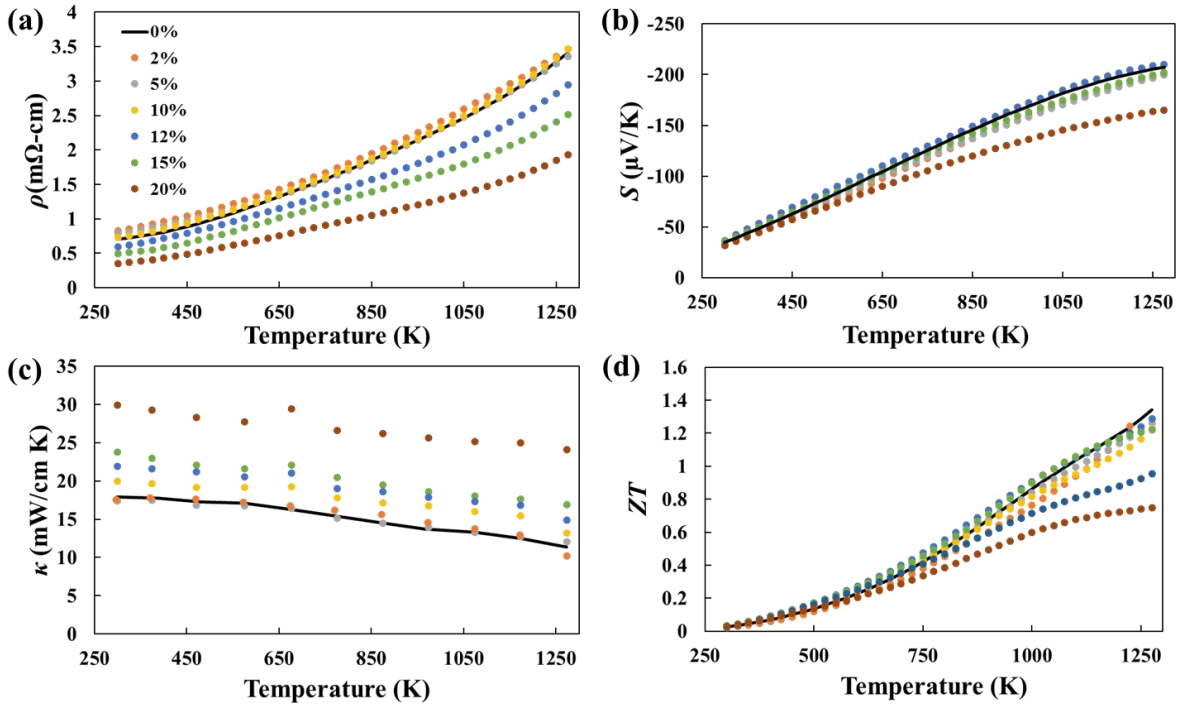

Figure 2.1 Thermoelectric properties of $LaTe_{1.46}$-Ni composites ranging from 0-20 vol%. (a) Electrical resistivity, (b) Seebeck coefficient, (c) total thermal conductivity, and (d) dimensionless figure of merit.[12]

The mechanism responsible for the gradual decrease in electrical resistivity has been termed "composite-assisted funneling of electrons (CAFE)" where the drop in electrical resistivity is a result of the formation of low resistance pathways by the Ni inclusions. Monte Carlo simulations were used to solve for thermal and electrical continuity and shows the electrical current density is highest between Ni inclusions (Figure 2.2(a)).[12] The minimum threshold for the amount of Ni required to decrease the resistivity of the composite suggests that there is a proximity criterion between the Ni particles.[12] However, the CAFE mechanism is

distinct from percolation seen in other systems because the reduction in resistivity occurs gradually and at loading fractions much lower than those required for traditional percolation.[12,13] Additionally the CAFE phenomenon observed is also distinct from effective medium theory. The delayed onset of reduction in the Seebeck coefficient with respect to reduction in electrical resistivity is a result of large differences in the thermal conductivities between the inclusions and matrix. Since the thermal conductivity of Ni is significantly larger than that of the $LaTe_{1.46}$ matrix, the Ni particles act as thermal shunts resulting in smaller temperature differences across the inclusions. Therefore, from an electrical standpoint, the Ni inclusions behave similar to voids which have been shown to have little impact on the Seebeck coefficient of bulk materials.[14]

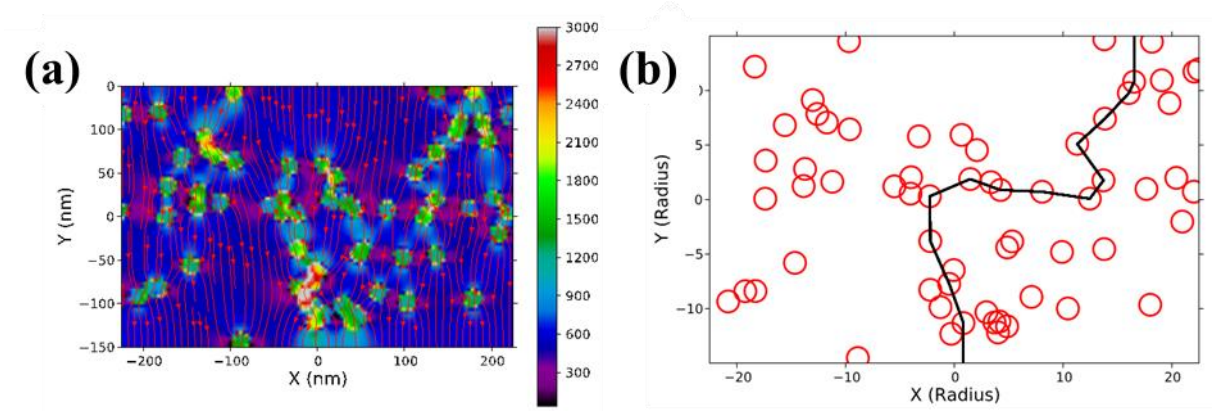

Figure 2.2 Monte Carlo simulations of $LaTe_{1.46}$-Ni composites. (a) Contour plot of the electrical current density for a $La_{3-x}Te_4$ matrix material with 63 Ni inclusions. (b) The black line denotes the shortest path between the top and bottom boundaries across the Ni inclusions (red circles) with neighboring distances not exceeding 4.4x the inclusion radius.[12]

While the 2D Monte Carlo simulations in Figure 2.2 support the existence of the CAFE mechanism, the proximity criterion for the Ni particles is currently not well defined. The computational model assumes that in order for current to preferentially pass from one Ni particle to another, the Ni particles must be within 4.4x the radius of another Ni particle. The validity of

this assumption is still under investigation and warrants further computational study. Additionally, the role of Ni particle morphology in the CAFE mechanism has not yet been investigated. For these reasons, the initial particle size of the Ni inclusions was varied from the nanometer range to particles hundreds of microns in diameter while keeping the volume fraction of Ni constant. Decreasing the Ni particle size was expected to increase the electrical resistivity and decrease the thermal conductivity of the composites due to the larger number of interfaces present in the composite. Conversely, the larger Ni particles were expected to decrease the electrical resistivity and increase the thermal conductivity due to the smaller number of Ni/$LaTe_{1.46}$ interfaces.

2.2. Synthetic Methods

In this study lanthanum telluride was made using a previously reported mechanochemical synthetic procedure with a stoichiometry of $LaTe_{1.46}$ for optimal thermoelectric properties.[15] All manipulations of the starting elements and synthesized powders were handled in an Ar-filled glovebox (H_2O < 1 ppm, O_2 < 0.1 ppm). Elemental La (99.9%, metals basis, HEFA Rare Earth) was combined with Te (99.999%, 5N Plus) and sealed under argon in a stainless steel vial with stainless steel balls. The vial was then placed in a ball mill and milled until a homogeneous $LaTe_{1.46}$ powder was synthesized. The same batch of $LaTe_{1.46}$ parent powder was used for all composites to ensure a constant carrier concentration in the matrix. Ni powders were procured from Alfa Aesar with the following particle sizes: 2.2-3 μm (99.9%, metals basis), 5-15 μm (99.8%, metals basis), 80-150 nm (99.8%, metals basis), and -50+100 mesh (300-150 μm, 99.7%, metals basis). The as-received powders likely had oxide on the surface, which detrimentally affected the thermoelectric performance of the composites. For this reason, the Ni particles were treated in a reducing atmosphere of forming gas (7% H_2 in Ar) and heated to

reduce the surface NiO. 15 vol% of Ni powder was then blended with the $LaTe_{1.46}$ powder to homogenously disperse the Ni particles. The blended powder was loaded into a 12.7 mm graphite die and the powders were compacted through spark plasma sintering (SPS) at temperatures above 1200 °C.

The sintered compacts had densities greater than 98% of the theoretical density, measured using the Archimedes method. Scanning electron microscopy (SEM) was performed on the Ni powders before and after reduction to ensure the particle size did not change. Back-scattered electron (BSE) SEM was performed on the composites after sintering to observe the differences in the Ni microstructures. The volume fractions of the nickel inclusions were calculated using ImageJ analysis software on the SEM images.

Temperature-dependent electrical resistivity was measured using a combined 4-point probe/Hall effect system.[16] The high-temperature Seebeck coefficient was measured using a custom-fabricated system.[17] Thermal diffusivity measurements were carried out using a commercial Netzsch LFA 457 laser flash analysis system. Differential scanning calorimetry (DSC) was performed to measure the heat capacity of the composites using a Netzsch DSC 404. Experimental error in electrical resistivity, Seebeck, and thermal conductivity were found to be approximately 5, 20, and 10 % respectively, resulting in a propagated error in *ZT* of 30%.

2.3. Thermoelectric Properties of $La_{3-x}Te_4$-Ni Composites with Varying Ni Particle Sizes and Morphologies

To ensure the starting particles sizes were dissimilar and no changes occurred during the oxide reduction, SEM was performed on the as-received and the reduced Ni powders. The initial Ni powder size is in good agreement with expected size from the manufacturer (Figure 2.3(a-d)).

In addition to the powders being different sizes the morphologies also varied, ranging from more spherical particles for the 80-150 nm and 5-15 µm powders to having more textured surfaces for the 2.2-3 µm and 150 – 300 µm powders. There were no changes to the powder sizes or morphologies of the Ni powders post-reduction (Figure 2.3(e-h)).

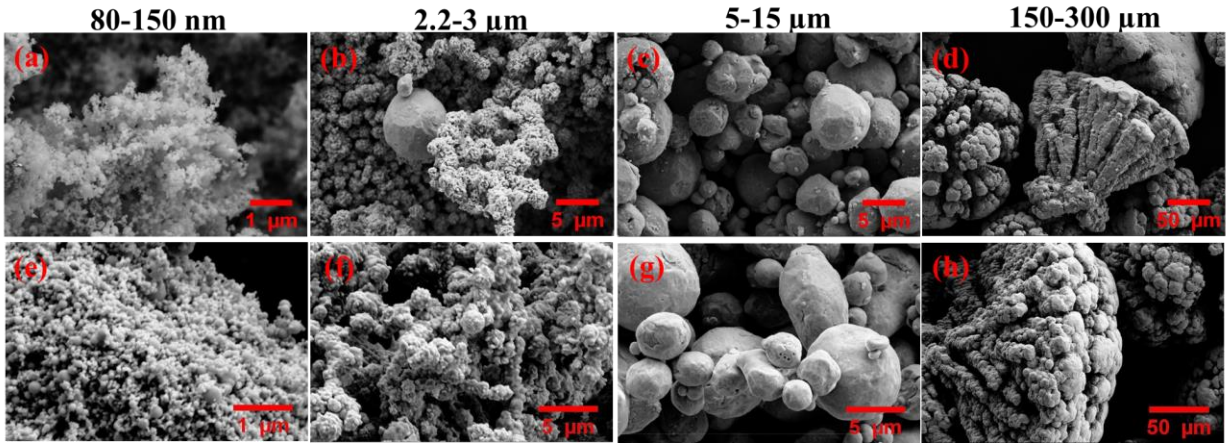

Figure 2.3 SEM images of Ni powders as-received (a-d) and post-reduction (e-f). Particle sizes were in good agreement with the manufacturer's advertised size. No particle growth or changes to the surfaces were observed.

After compaction, the samples were polished and the microstructures were analyzed using BSE SEM. Figure 2.4 compares the microstructure of the composites made with nickel as-received and nickel which had undergone the oxide reduction process. The reduction of the nickel particles did not significantly alter the microstructure, which was also observed in the composites made with other nickel particle sizes. Additionally, there was no observable reaction between the nickel particles and the $LaTe_{1.46}$ matrix. This is consistent with the results from prior investigations of the interface between the Ni inclusions and matrix.[5]

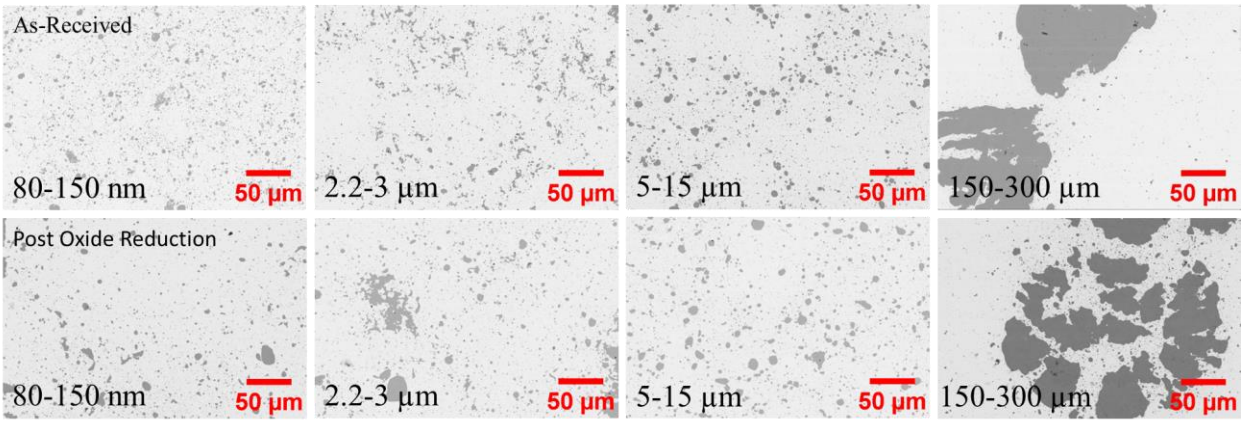

Figure 2.4 BSE SEM micrographs of 2.2-3 µm composites with as-received (a) and post oxide reduction (b) powders. No major changes to the microstructure of the Ni inclusions were observed.

A comparison of the microstructures for the samples that underwent the reduction process is shown in Figure 2.5. The light regions in the images are the $LaTe_{1.46}$ matrix and the dark regions correspond to the Ni inclusions. This contrast is expected due to both La and Te having higher atomic numbers (*Z*) than Ni, which would make them appear brighter in BSE mode. The starting Ni particle size influences the sizes of the Ni inclusions after densification (Figure 2.5). Table 2.1 presents the calculated area coverage of the Ni particles and all are in good agreement with the nominal value of 15%. The 80-150 nm, 2.2-3 µm, and 5-15 µm samples show similar microstructure in terms of size and dispersion, however the inclusions in the 5-15 µm sample appear to be more spherical and better dispersed than in the 2.2-3 µm samples that were previously studied. The microstructure of the 80-150 nm sample contains some larger inclusions, similar to those seen in the 2.2-3 µm and 5-15 µm composite samples, in addition to much smaller Ni particles, on the order of 1 µm or less, which are not present in the other samples. The

inclusions in the 150-300 µm composite are much larger than in any other composite, although there are smaller particles dispersed amongst the larger Ni particles.

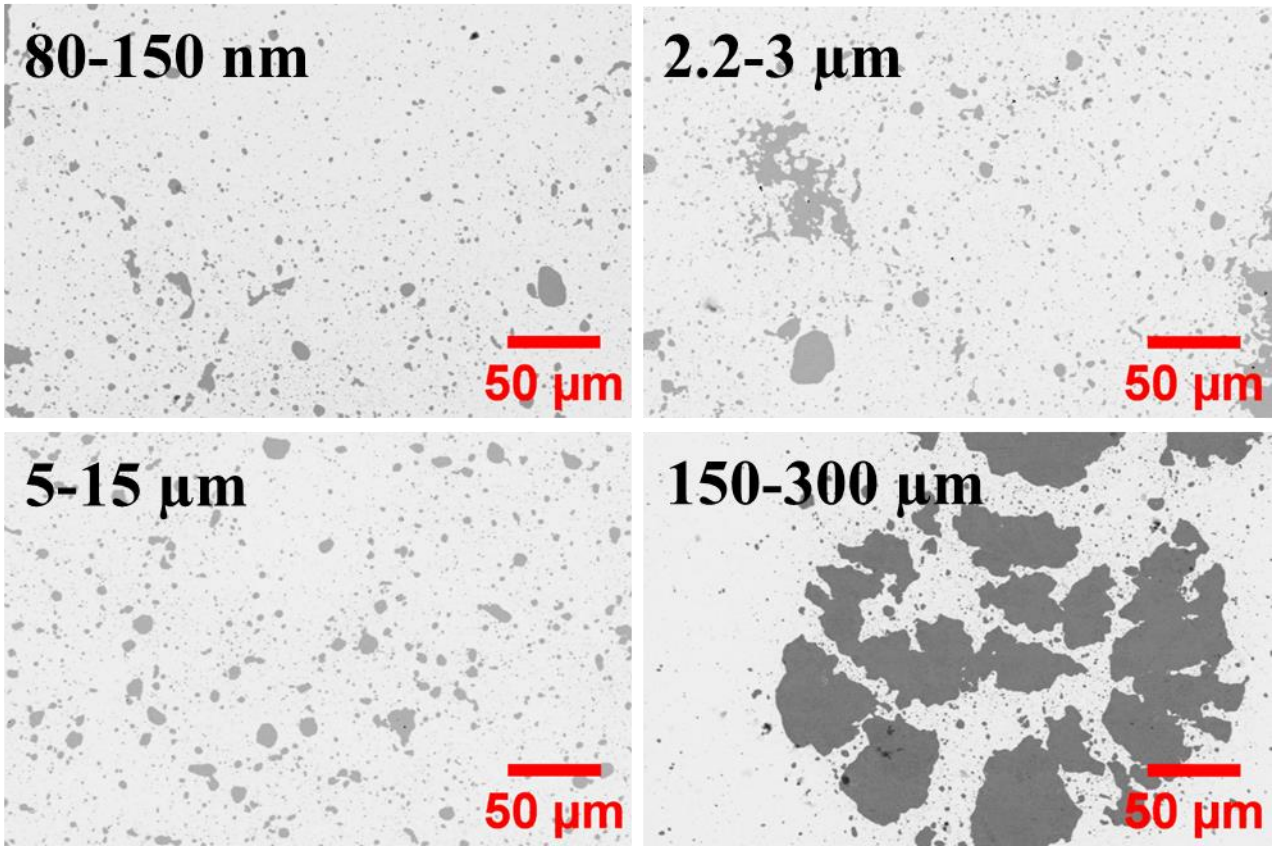

Figure 2.5 Back-scattered SEM images of $LaTe_{1.46}$-Ni composites using different nickel starting particle sizes.

Ni Starting Morphology	Calculated Ni Inclusion %
80-150 nm	15.2
2.2-3 µm	17.4
5-15 µm	17.2
150-300 µm	13.8

Table 2.1 Ni inclusion percentage calculated from SEM micrographs. The values match well with the nominal Ni fraction of 15 vol%.

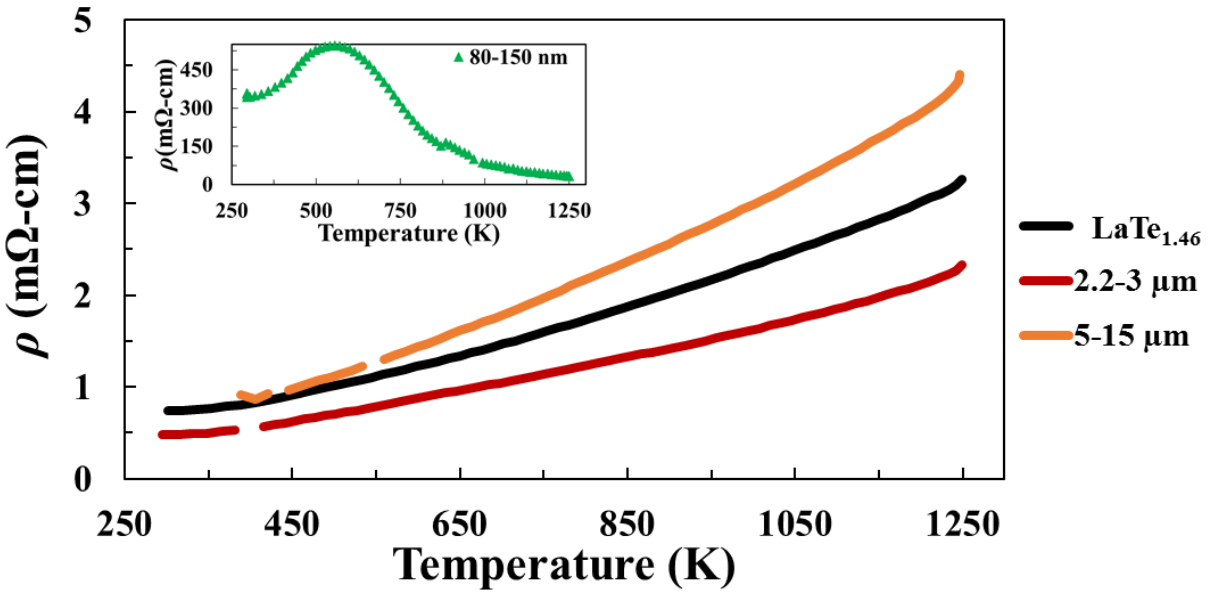

Figure 2.6 Temperature-dependent resistivity for $LaTe_{1.46}$-Ni composites made with the as-received nickel powders. The resistivity of the 80-150 nm (inset) and 5-15 µm composites were found to increase the resistivity of the composites. Ohmic contacts for the 150-300 µm sample could not be made due to the composite having an exceptionally high resistivity.

With exception of the 2.2-3 µm nickel, composites made with the as-received nickel powders were all found to have temperature-dependent resistivities higher than that of $LaTe_{1.46}$ (Figure 2.6). Addition of the as-received 5-15 µm nickel powder increase the resistivity by 33%

compared to the parent. The 80-150 nm composite (inset of Figure 2.6) exhibited significantly increased resistivity values, reaching as high as 100's of mΩ-cm. Resistivity data on the 150-300 μm composite was not collected due to the exceptionally high resistivity of the sample preventing Ohmic contacts being made. It was hypothesized that the increases in resistivity resulted from the nickel powders having a surface oxide, acquired either during synthesis of the powders or during transport from the vendor. As lanthanum is significantly more electropositive than nickel, the lanthanum could remove oxygen from the oxide layer resulting in a loss of charge carriers from the $LaTe_{1.46}$ matrix and cause the increased resistivity of the composites. For subsequent composites, the nickel powders were first treated in a reducing atmosphere of 7% H_2 in argon to remove the oxide layer.[18]

Temperature-dependent electrical resistivities and Seebeck coefficients for the reduced composites are shown in Figure 2.7 from 300-1275 K. All composites had resistivities lower than that of the baseline $LaTe_{1.46}$ sample (Figure 2.7(a)). The resistivity of the 5-15 μm composite had similar values to the parent $LaTe_{1.46}$ at high-temperature. An intermediate drop in resistivity was observed for the 80-150 nm composite, which was more resistive than the baseline 2.2-3 μm composite. The reduced 2.2-3 μm and 150-300 μm composites had very similar resistivities to one another. The corresponding Seebeck coefficients for the reduced 2.2-3 μm and 150-300 μm samples both decreased below the $LaTe_{1.46}$ values, which trend with what would be expected given their decreased resistivities (Figure 2.7(b)). This likely indicates that the samples have become conductive enough that the resistivities and Seebeck coefficients are no longer decoupled. Significant increases in the Seebeck coefficients for the 5-15 μm and 80-150 nm composites were observed.

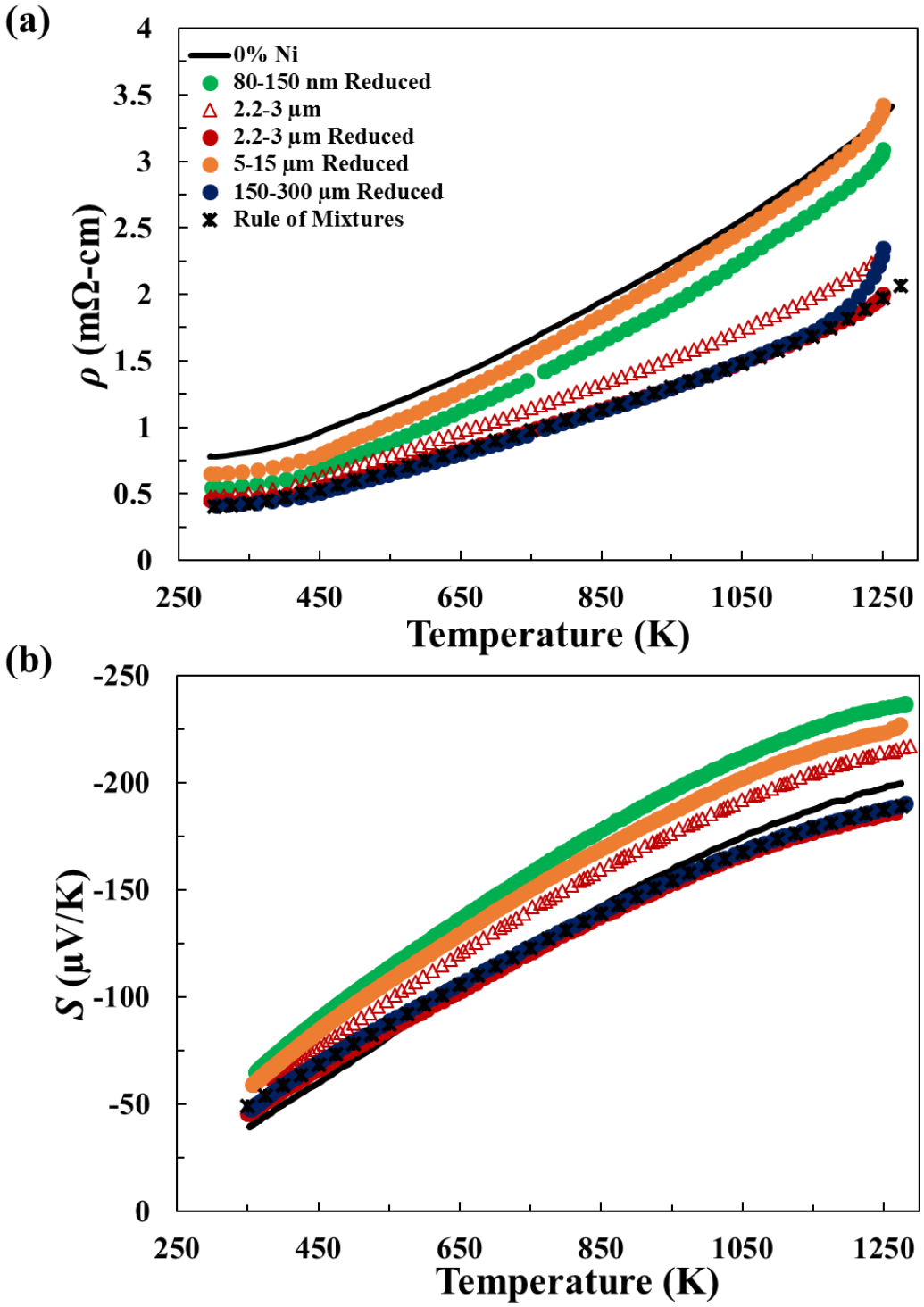

Figure 2.7 Temperature-dependent (a) electrical resistivities and (b) Seebeck coefficients of the composites.

The underlying cause of this increase is still under investigation. A possible explanation is a small amount of nickel oxide remained on the surface of the two nickel powders after the reduction process. This residual oxide would result in a decreased carrier concentration, resulting in the observed increased Seebeck coefficient. A decrease in the carrier concentration should also result in the composites having increased resistivities compared to the parent material. However, the increased resistivity could be then offset by the CAFE effect, which would explain why the 80-150 nm and 5-15 μm samples had resistivities higher than the other composites but still below the baseline $LaTe_{1.46}$.

The power factor for each composite was calculated by combining the Seebeck coefficient and electrical resistivity. Despite large increases in Seebeck coefficients for the samples made with 80-150 nm and 5-15 μm Ni particles, the baseline 2.2-3 μm composite exhibits the highest power factor above 900 K (Figure 2.8). However, the power factor of the 80-150 nm composite was the largest at temperatures below 900 K. All samples exhibited power factors much higher than that of the parent $LaTe_{1.46}$ sample. This supports the theoretical predictions of improved power factors of composites made by Bergman and Fel.[7]

In order to calculate the thermal conductivities of the composites, the high-temperature specific heat capacity (c_p) of the 2.2-3 μm composite was measured. The experimental heat capacity is flat, as expected, and agrees well with the heat capacity estimated using a rule of mixtures between $LaTe_{1.46}$ and pure nickel (Figure 2.9).

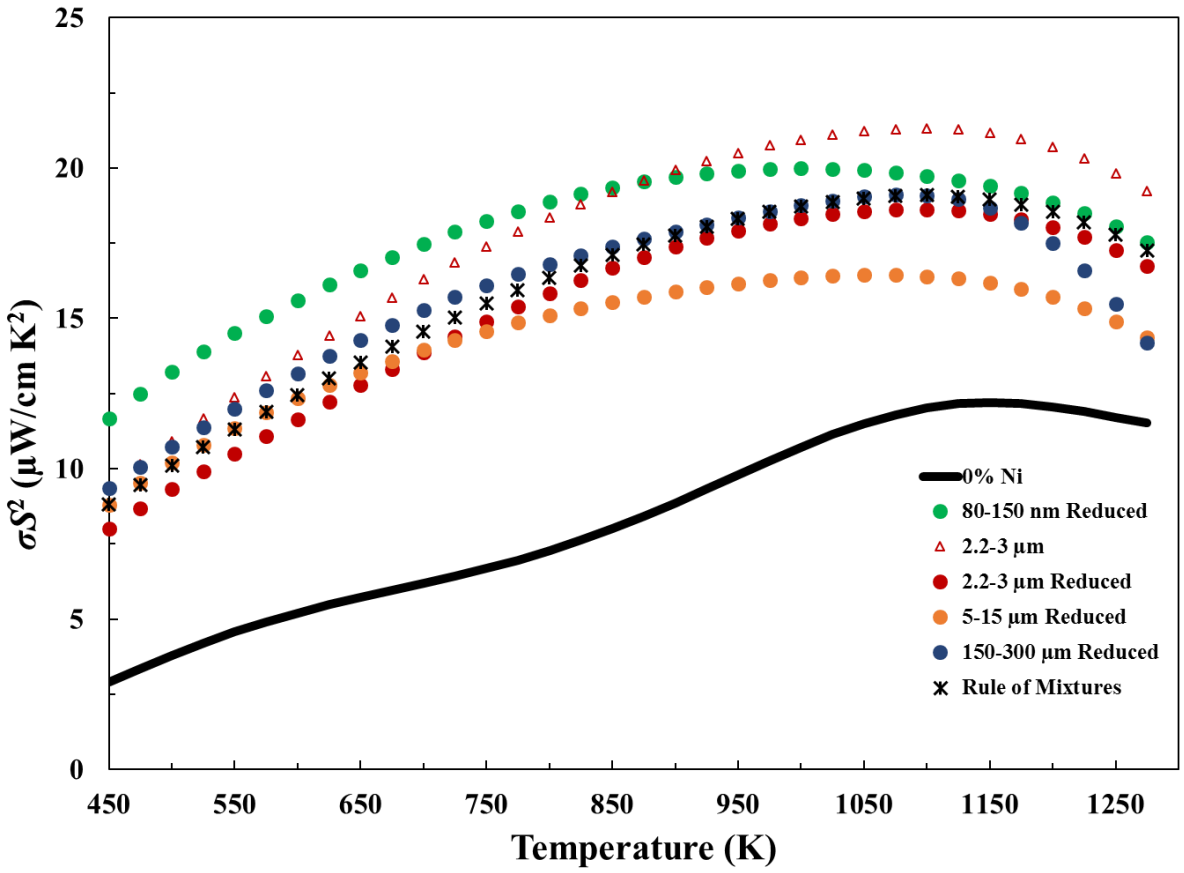

Figure 2.8 Temperature-dependent power factor for $LaTe_{1.46}$-Ni composites.

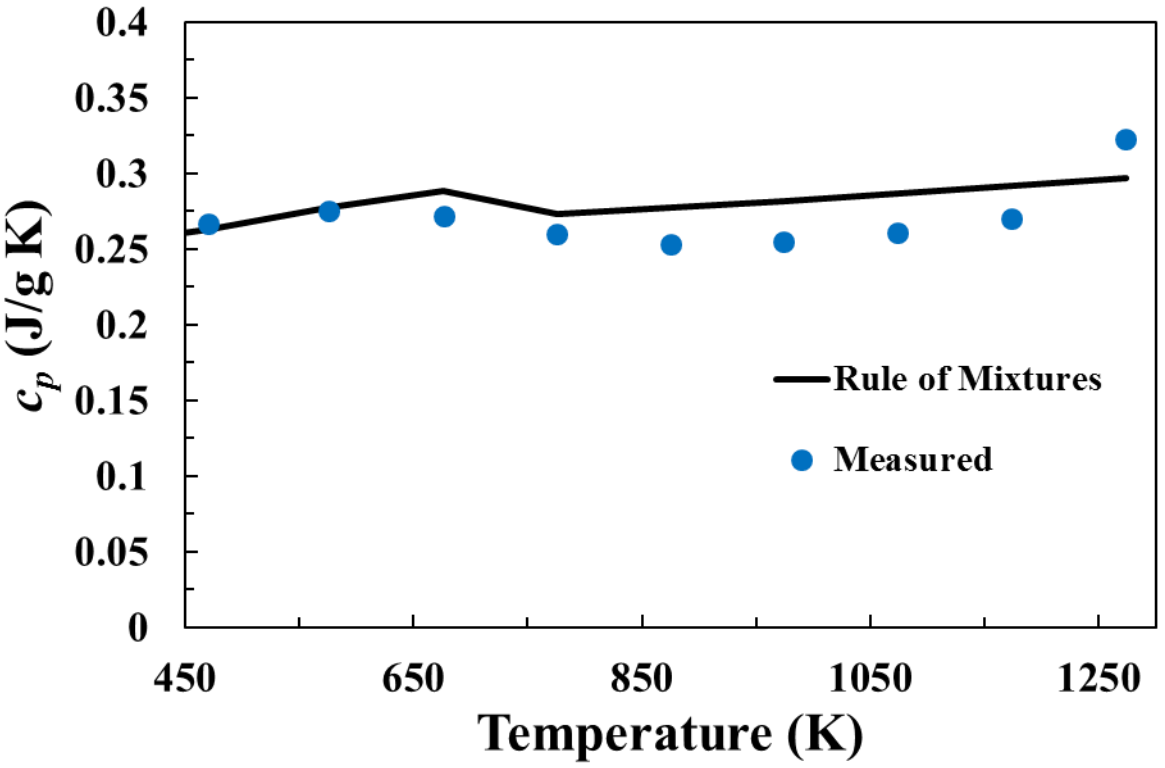

Figure 2.9 High-temperature specific heat capacity of the 2.2-3 μm composite. The heat capacity is in good agreement with the estimated heat capacity calculated using the rule of mixtures.

The thermal conductivities of the composites were calculated by combining the measured heat capacity with thermal diffusivity measurements (Figure 2.10). Open circles denote the lattice thermal conductivities calculated from the Wiedemann-Franz law using a temperature-dependent Lorenz number generated using a single parabolic band approximation.[19] The total and lattice thermal conductivities of the reduced 2.2-3 μm composite are similar to the baseline 2.2-3 μm composite even though it had a lower electrical resistivity. The remaining composites had thermal conductivities lower than the baseline composite, with the 80-150 nm and 5-15 μm composites having total and lattice thermal conductivities lower than the baseline $LaTe_{1.46}$ sample. Reduction in thermal conductivity for the 80-150 nm sample is unexpected due

to the decreased resistivity of the sample. The reduction in its lattice thermal conductivity suggests that there may be an additional phonon scattering mechanism present, but the source is unclear, though it may be due to phonon scattering by the nanoscale inclusions. The low lattice thermal conductivity of the 150-300 μm sample is most likely a result of the sample deviating from the Wiedemann-Franz law. Calculating a temperature-dependent Lorenz number using the single parabolic band model for a multiband system has limitations as $La_{3-x}Te_4$ has multiple bands near the Fermi level.[20]

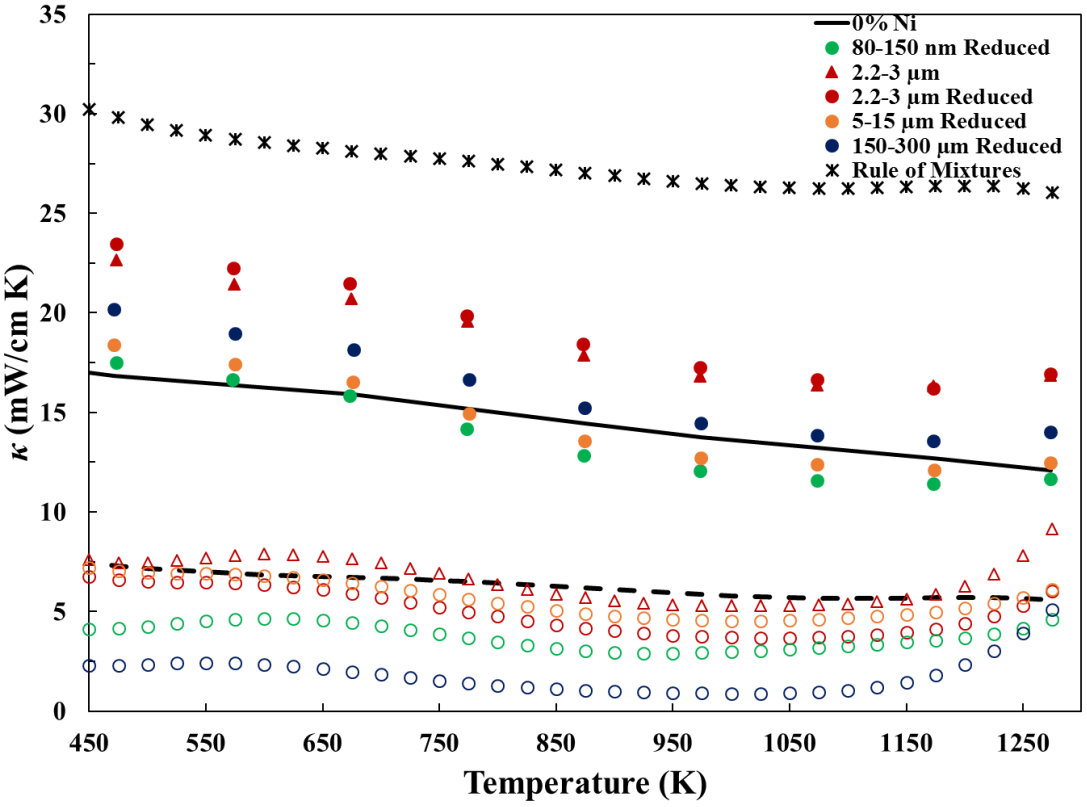

Figure 2.10 High-temperature thermal conductivities of the samples. Open symbols represent the lattice contribution to the thermal conductivity calculated using the Wiedemann-Franz law. The dashed black line denotes the lattice contribution to the thermal conductivity for the $LaTe_{1.46}$ sample.

The dimensionless figure of merit was calculated by combining all of the measured thermoelectric properties (Figure 2.11). The reduced 2.2-3 μm sample had the lowest *ZT* of all of the composites, but still had a peak *ZT* similar to that of the parent $LaTe_{1.46}$. The baseline 2.2-3 μm (as-received), 5-15 μm, and 150-300 μm samples all had similar *ZT* values that were 25% higher than the baseline $LaTe_{1.46}$ at 1200 K. The improvement of *ZT* for the 5-15 μm composite is due to the decreased thermal conductivity and increased Seebeck coefficient, whereas the 150-300 μm composite benefitted from a greatly decreased electrical resistivity and a slightly decreased thermal conductivity. The 80-150 nm composite reaches a peak *ZT* of 1.9 at 1200 K, which is a 66% increase over $LaTe_{1.46}$. This is a direct result of all three thermoelectric properties changing favorably in the composite.

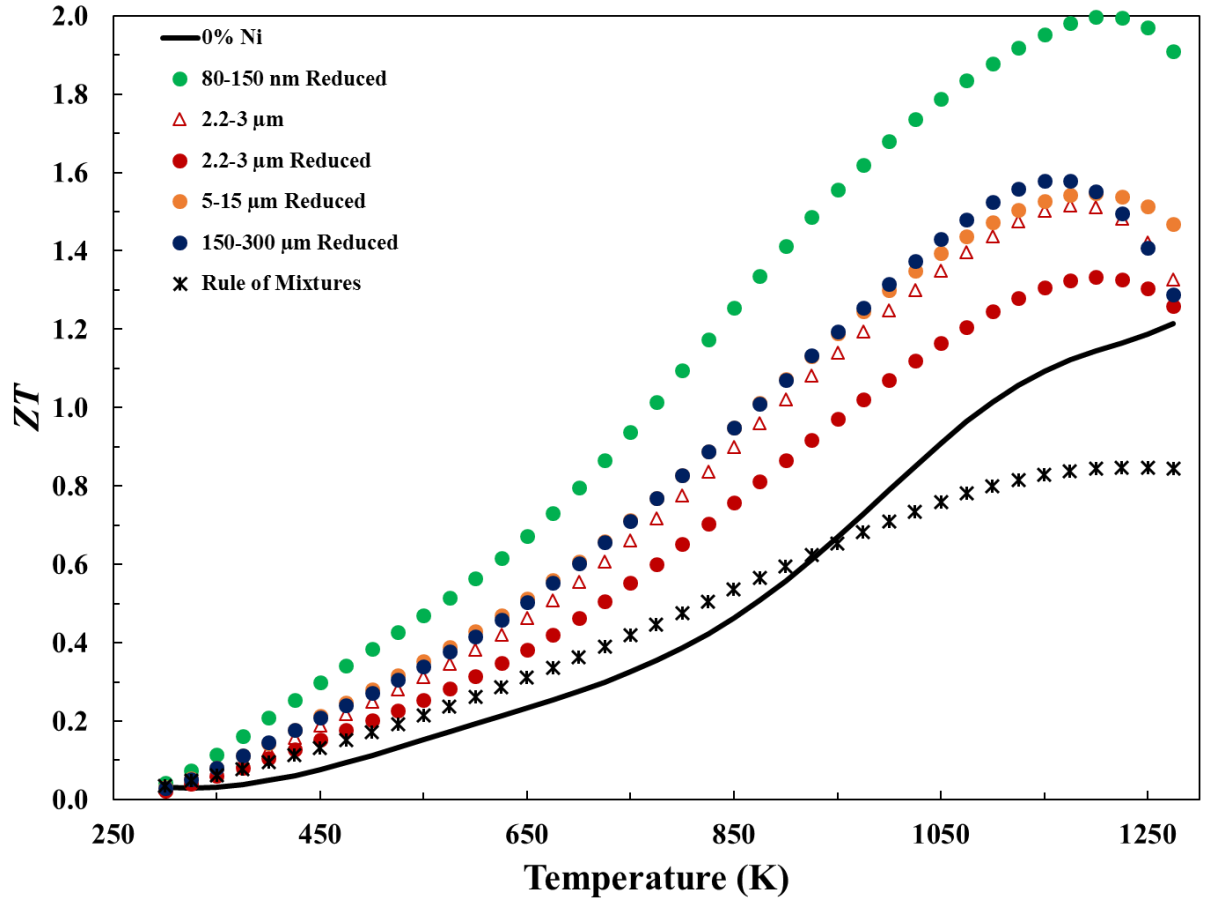

Figure 2.11 Thermoelectric figure of merit as a function of temperature for $LaTe_{1.46}$-Ni composites. A propagated error of 30% in *ZT* was calculated.

2.4. Conclusions

$LaTe_{1.46}$-Ni composites with larger and smaller nickel inclusions compared to previous studies were successfully synthesized and their thermoelectric properties measured. At an equivalent volume fraction, larger nickel particle sizes were found to decrease the thermal conductivity while leaving the power factor unaffected. This resulted in *ZT* values which were similar to the starting baseline composite used in this study. Composites made with smaller Ni particle size were found to increase resistivity and Seebeck coefficient, while also resulting in a

decreased thermal conductivity. As all three thermoelectric properties trended favorably, the 80-150 nm composite was shown to have a 66% increase in *ZT*. The increases in resistivities and Seebeck coefficients were attributed to residual surface oxide on the nickel particles even after the reduction process. The competing effects of the CAFE mechanism to lower the composite resistivity, the oxide lowering the carrier concentration of the matrix, and enhanced phonon scattering due to a smaller inclusion size enable a *ZT* to 1.9 to be achieved at 1200 K.

2.5. References

[1] G. J. Snyder and E. S. Toberer, *Nature Materials*, **2008**, *7*, 105.

[2] D. M. Rowe, *CRC Handbook of Thermoelectric Materials*, CRC Press, 1995

[3] B. C. Sales, D. Mandrus, B. C. Chakoumakos, V. Keppens, and J. R. Thompson, *Phys. Rev. B*, **1997**, *56*, 23.

[4] G. J. Snyder, M. Christensen, E. Nishibori, T. Caillat and B. B. Iversen, *Nat. Mat.*, **2004**, *3*, 458.

[5] J. M. Ma, *Improving the Mechanical Strength and Power Conversion Efficiency of High Temperature Thermoelectrics*, Doctoral Dissertation, University of California, Los Angeles, **2014**

[6] D. J. Bergman and O. Levy, *J. Appl. Phys.* **1991**, *70*, 6821.

[7] D. J. Bergman and L. G. Fel, *J. Appl. Phys.*, **1999**, *85*, 12.

[8] K. T. Kim, H. Y. Koo, G.-G. Lee, G. H. Ha, *Materials Letters*, **2012**, *85*, 141.

[9] M.S. Dresselhaus, G. Chen, Z.F. Ren, G. Dresselhaus, A. Henry, and J.-P. Fleurial, *JOM*, **2009**, *61*, 86. (Nanocomposites)

[10] K. T. Kim, S. Y. Choi, E. H. Shin, K. S. Moon, H. Y. Koo, G.-G. Lee, G. H. Ha, *Carbon*, **2013**, *52*, 541.

[11] J. P. Heremans, and C. M. Jaworski, *Appl. Phys. Lett.*, **2008**, *93*, 122107.

[12] J. M. Ma, P. von Allmen, S. V. Prikhodko, T. Vo, R. B. Kaner, S. K. Bux, and J-P. Fleruial, "Composite Assisted Funneling of Electrons (CAFE) for Improved Performance of Bulk Thermoelectric Materials" *Submission Pending*.

[13] D. E. Aldrich and Z. Fan, *Mat. Char.*, **2001**, *47*, 167.

[14] D. M. Rowe, *J. Phys. D.*, **1975**, *8*, 1092.

[15] A. F. May, J.-P. Fleurial, and G. J. Snyder, *Phys. Rev. B*, **2008**, *78*, 125205.

[16] K. A. Borup, E. S. Toberer, L. D. Zoltan, G, Nakatsukasa, M. Errico, J.P. Fleurial, B. Iversen, and G. J. Snyder, *Rev. of Sci. Inst.*, **2012**, *83*, 123902.

[17] C. Wood, D. Zoltan, and G. Stapfer, *Rev. Sci. Inst.*, **1985**, *56*, 5.

[18] J. T. Richardson, R. Scates, and M. V. Twigg, *Applied Catalysis A: General*, **2003**, *246* 137.

[19] H.-S. Kim, Z. M. Gibbs, Y. Tang, H. Wang and G. J. Snyder, *APL Mater.*, **2015**, *3*, 041506.

[20] A. F. May, D. J. Singh, and G. J. Snyder, **2009**, *Phys. Rev. B*, 79, 153101.

Chapter 3: *ZT* Enhancement of $La_{3-x}Te_4$-Co Composites

3.1. Introduction

Extensive research has been conducted on improving of the dimensionless figure of merit, $ZT = S^2T/\rho\kappa$, of thermoelectric materials through the use of composites.[1-5] Composites have been studied in an attempt to make materials with "phonon glass electron crystal" properties.[6] One strategy to accomplish this is to introduce inclusions into a material with desirable electronic properties to promote phonon scattering, thereby decreasing the thermal conductivity of the composite.[1,2] The second approach is to add conductive inclusions to a low thermal conductivity matrix to decrease the electrical resistivity.[3,4] However, the effectiveness of these two strategies has been limited, as the secondary phase will often detrimentally affect the interconnected properties, degrading the *ZT* of the composite.

As discussed in Chapter 2, it was found that addition of 2.2-3 μm nickel inclusions to $La_{3-x}Te_4$ lowered the electrical resistivity while leaving the Seebeck coefficient unaffected for volume fractions of nickel between 12-15%.[5] This resulted in the composites having similar *ZT* values as the parent $LaTe_{1.46}$ while improving mechanical robustness. *ZT* did not increase as the gains in the power factors (σS^2) were offset by the increased thermal conductivities of the composites.[7] Decoupling of the electronic transport properties in this system was attributed to a new mechanism, composite assisted funneling of electrons (CAFE).[7] Nickel inclusions formed low resistance pathways for electrons to travel along, leading to the observed decreased resistivity.

Thus far, the CAFE mechanism has only been observed in $La_{3-x}Te_4$-Ni composites. While *ZT* is an important parameter when designing devices, other considerations, such as chemical

compatibility and thermomechanical properties, must be taken in to account to maximize device efficiency and robustness.[8-11] Therefore, extension of the CAFE effect utilizing inclusions other than nickel is of interest to allow for flexibility when choosing composite materials for future thermoelectric devices.

In the research presented here, $La_{3-x}Te_4$-Co composites were investigated to determine if the CAFE mechanism occurs in systems with inclusions other than nickel. Cobalt was chosen as an alternative to nickel due to both metals having similar electrical, thermal, and mechanical properties.[12] Due to the similarities in their properties, it was expected that the $La_{3-x}Te_4$-Co composites would display similar electronic and thermal properties to those previously reported for $La_{3-x}Te_4$-Ni composites.

3.2. Synthetic Methods

Lanthanum telluride powder was synthesized using a previously established mechanochemical procedure with a stoichiometry of $LaTe_{1.46}$ for optimum thermoelectric properties.[13] All manipulations of the starting elements and synthesized powders were performed in an argon filled glovebox (H_2O < 1 ppm, O_2 < 0.1 ppm). Elemental lanthanum (99.9%, metals basis, HEFA Rare Earth) was combined with tellurium (99.999%, 5N Plus) and sealed under argon in a stainless steel vial with stainless steel balls. The vial was then placed in a ball mill and milled until a homogeneous $LaTe_{1.46}$ product was synthesized. The same $LaTe_{1.46}$ parent powder was used for all composites to ensure a constant carrier concentration in the matrix. 1.6 μm cobalt powder (99.9%, Alfa Aesar) was used as-received. This starting particle size was chosen as it was similar in size to a previous composite study using nickel powder.[5] Cobalt powder was blended with the parent $LaTe_{1.46}$ with volume fractions of: 2, 5, 8, 10, 12, and 15%. The blended

powder was loaded into a 12.7 mm graphite die and the powders were compacted through spark plasma sintering (SPS) at temperatures above 1200 °C. The sintered compacts had densities greater than 98% of the theoretical density, measured using the Archimedes method.

A Zeiss 1550 VP SEM was used to perform scanning electron microscopy (SEM) on the Co powder to observe the morphology. Back-scattered electron (BSE) SEM was performed on the compacted composites to compare the cobalt microstructure to that previously observed in the Ni composites. The volume fractions of the nickel inclusions were calculated using ImageJ analysis software on the SEM images. Powder X-ray diffraction (PXRD) data was collected with a Phillips PANalytical X'Pert Pro diffractometer using Cu K_α radiation on compacts ground using a mortar and pestle. Due to the high moisture and air sensitivities of the $LaTe_{1.46}$-Co powders, the powders were sealed with 1 mm thick Kapton film (McMaster-Carr) on a Si zero background holder under argon.

A custom built combined 4-point probe and Hall Effect system was used to measure the electrical resistivity.[14] The high-temperature Seebeck coefficient was measured using a custom-fabricated system.[15] Thermal diffusivity measurements were carried out using a commercial Netzsch LFA 457 laser flash analysis system. Differential scanning calorimetry (DSC) was performed to measure the heat capacity of the composites using a Netzsch DSC 404. Experimental error in electrical resistivity, Seebeck, and thermal conductivity were found to be approximately 5, 20, and 10 % respectively, resulting in a propagated error in *ZT* of 30%.

3.3. Microstructure and Thermoelectric Properties of $La_{3-x}Te_4$-Co Composites

Scanning electron microscopy was performed on the cobalt powder to compare the starting morphology to that of the nickel powder used in the previous $La_{3-x}Te_4$-Ni composite

study.[5] Micrographs of the powders are shown in Figure 3.1 and the observed morphologies of the powders were found to be different. The nickel powder is comprised of spherical particles with highly textured surfaces that agglomerate into longer chains (Figure 3.1(a)). The cobalt powder also has strand morphology, but appear more uniform and is not composed of smaller particles like the nickel powder (Figure 3.1(b)). However, despite differences in particle morphologies, the sizes of the cobalt and nickel powders were similar.

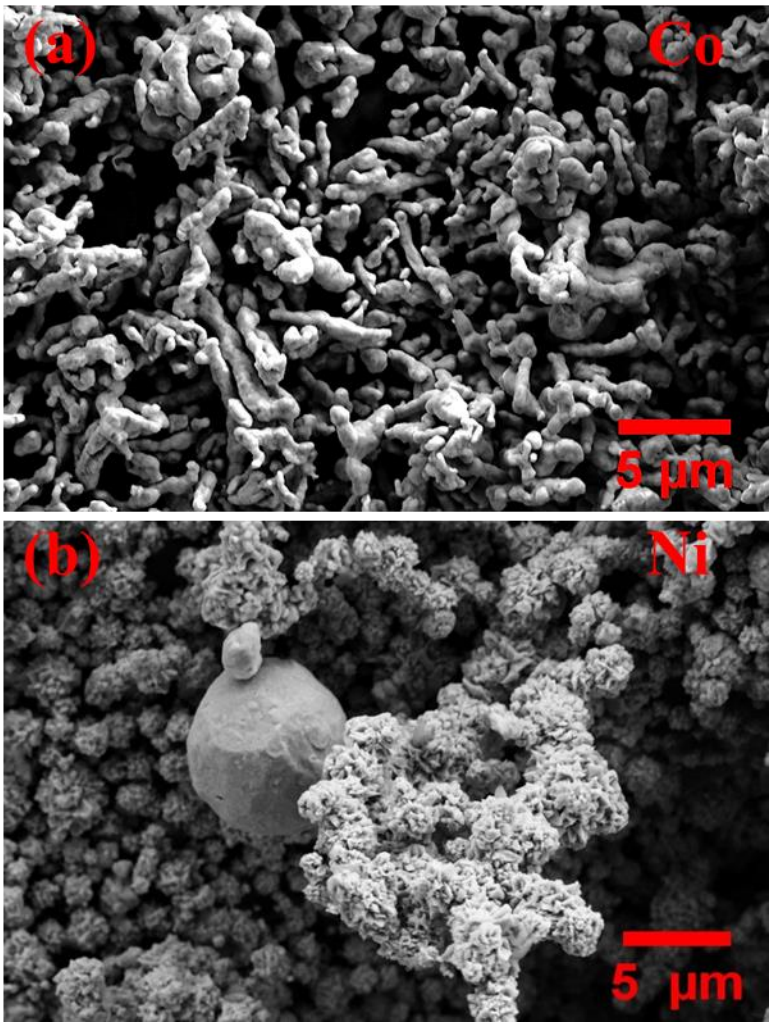

Figure 3.1 Secondary electron SEM images of (a) 1.6 µm cobalt and (b) 2.2-3 µm nickel. The powders are similar in size but differ in morphology. The nickel powder is made of long chains

of connected spherical particles. Conversely, the cobalt powder has similarly sized strands as the nickel particles, but were monolithic.

Compacted samples were polished and BSE SEM was performed to analyze the microstructures of the composites. Images of the composite's microstructures are shown in Figure 3.2. The light regions are the $LaTe_{1.46}$ matrix and the dark regions are the cobalt inclusions. This contrast is expected as cobalt has a lower atomic number (*Z*) than lanthanum and tellurium, making cobalt appear darker in BSE mode. From the images no secondary phases were observed. Image analysis was performed and the Co inclusion percentage was found to match well with the nominal values of the composites (Table 3.1) While the cobalt inclusions were dispersed throughout the samples, regions were observed where limited amounts cobalt were detected (Figure 3.2(d)). For comparison, BSE SEM images of cobalt and nickel composites are shown in Figure 3.3(a) and (b), respectively. This segregation of the metal inclusions was not observed in the Ni composites.

Co Nominal %	Calculated Co %
2	3.5
5	5.6
8	9.4
10	11.6
12	13.3
15	17.6

Table 3.1 Calculated Co inclusion percentages compared to nominal values. All calculated values match well with the expected values.

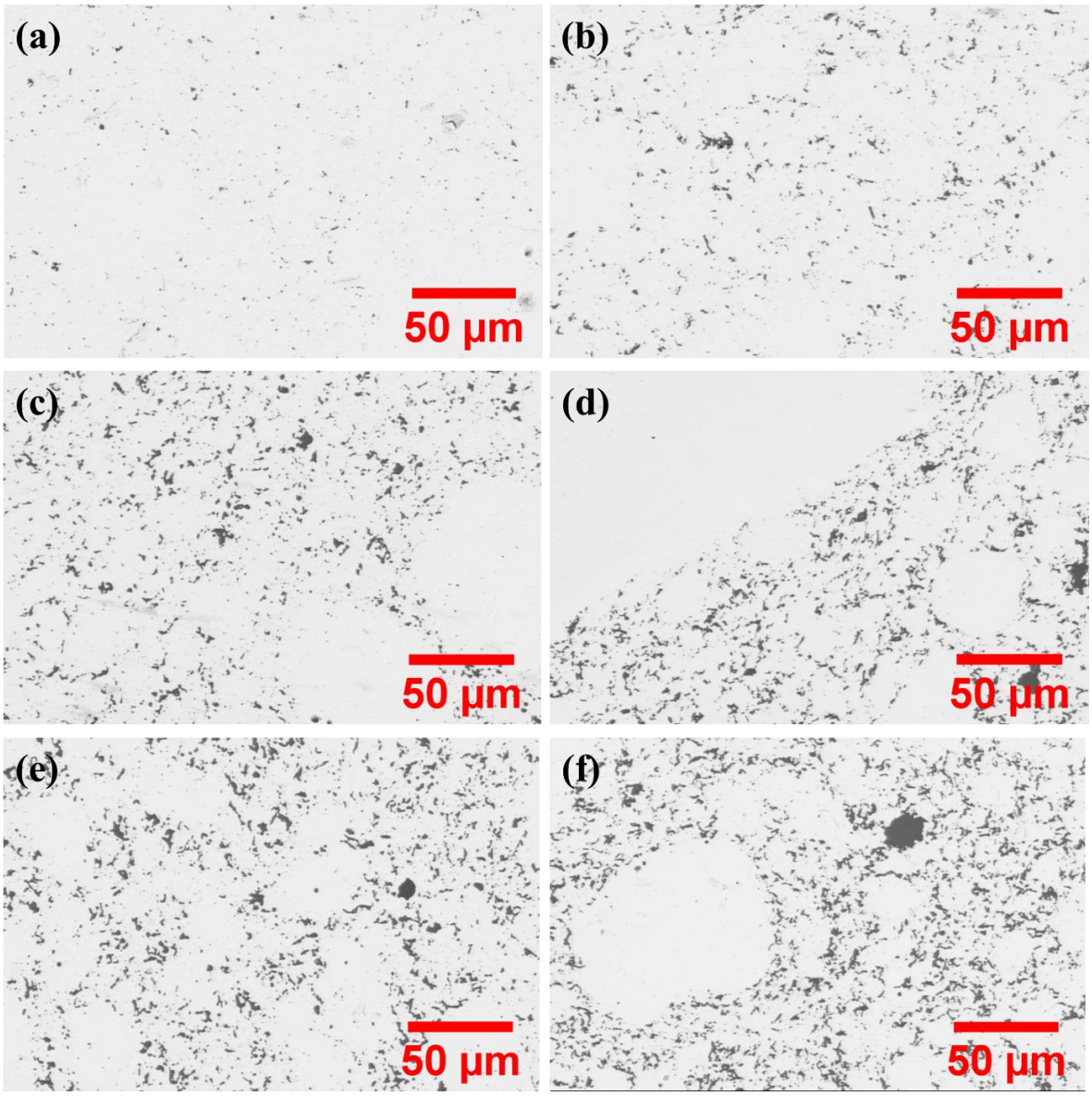

Figure 3.2 BSE SEM images of $LaTe_{1.46}$-Co composites with cobalt volumes fractions of (a) 2%, (b) 5%, (c) 8%, (d) 10%, (e) 12%, and (f) 15%. The cobalt content increases with increasing nominal cobalt volume percentage, as expected. While the cobalt appears to be well-dispersed, regions with limited amounts of cobalt were also observed.

While the properties of cobalt and nickel are similar in many aspects, they differ in their room temperature crystal structures. At standard pressure, cobalt undergoes a phase transition from hexagonal closed packed (HCP) to face centered cubic (FCC) at 723 K.[16] In contrast, nickel has no phase transition and is exclusively FCC.[17] The difference in the composite microstructure was initially attributed to differences in the crystal structures of the metallic inclusions. However, the cobalt present in the PXRD pattern has the FCC structure (Figure 3.4). The existence of the FCC phase at room temperature suggests that the cooling rates used during densification were rapid enough to quench in the FCC structure. Since both Ni and Co inclusions have the same structure in the composites, the origin of the differences in the microstructures is unknown and is under further investigation.

Temperature-dependent electrical resistivity measurements of the composites are shown in Figure 3.5(a). Near room temperature, the resistivities of the composites were similar to the parent $LaTe_{1.46}$ and then began to decrease at 8 vol% and above. This decrease in resistivity occurs at a lower inclusion volume fraction than what was seen in the previously studied $LaTe_{1.46}$-Ni composites, where the onset of CAFE occurred at 12 vol%.[5] Additionally, above 1100 K the resistivities of the samples were higher than $LaTe_{1.46}$ for the 2-8 vol% composites and similar to the parent powder at 10 and 12 vol%. The increased high-temperature resistivities for most of the composites suggest a reaction occurred with an impurity in the cobalt powder that altered the carrier concentration of the $LaTe_{1.46}$ matrix. Similar to what was observed in Chapter 2 with the $LaTe_{1.46}$-Ni composites, it is hypothesized that an oxide layer exists on the surface of the as-received cobalt powder. This oxide is thought to react with the $LaTe_{1.46}$ matrix during compaction, in which the lanthanum atoms pull oxygen from CoO. The oxidation of the lanthanum results in a loss of free carriers in the matrix. However, the gradual decrease in high-

temperature resistivity with increasing cobalt vol% suggest that the CAFE mechanism is occurring, but it is competing with the loss of charge carriers from reaction with the CoO .

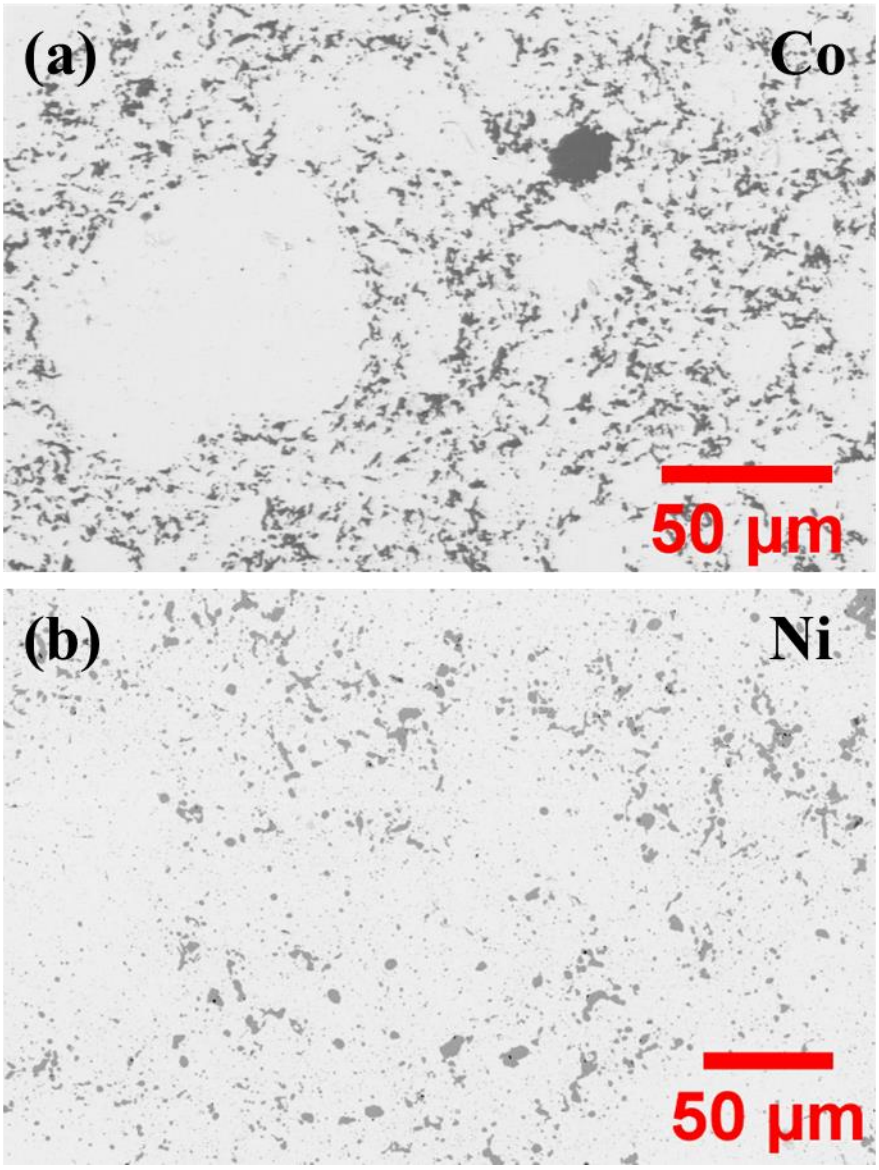

Figure 3.3 BSE SEM micrographs of 15 vol% (a) $LaTe_{1.46}$-Co and (b) $LaTe_{1.46}$-Ni composites. Large regions can be seen where small amounts cobalt are detected (a). Segregation of the inclusions and matrix was not observed in for the $LaTe_{1.46}$-Ni composites.

Further evidence of altered carrier concentrations in the matrix was seen in the temperature-dependent Seebeck coefficients of the composites (Figure 3.5(b)). The Seebeck coefficients increased above that of $LaTe_{1.46}$ for the 2-12 vol% composites, with an 18% increase in *S* occurring between 5 and 8 vol%. Considering the Mott equation for the Seebeck coefficient of metallically conducting materials, $S = \frac{2k_B^2 m^* T}{3e\hbar^2}(\frac{\pi}{3n})^{\frac{2}{3}}$, reduction of the carrier concentration, *n*, due to reactions with the Co surface oxide would cause an increase in *S*.[18] Above 10 vol% the Seebeck coefficient began to decrease from the maximum value, with the 15% composite's Seebeck decreasing significantly below that of the baseline material. This dramatic decrease in *S* and the electrical resistivity indicated that the electronic properties had become coupled and the CAFE mechanism was no longer observed in the $LaTe_{1.46}$-Co system above 12 vol%.

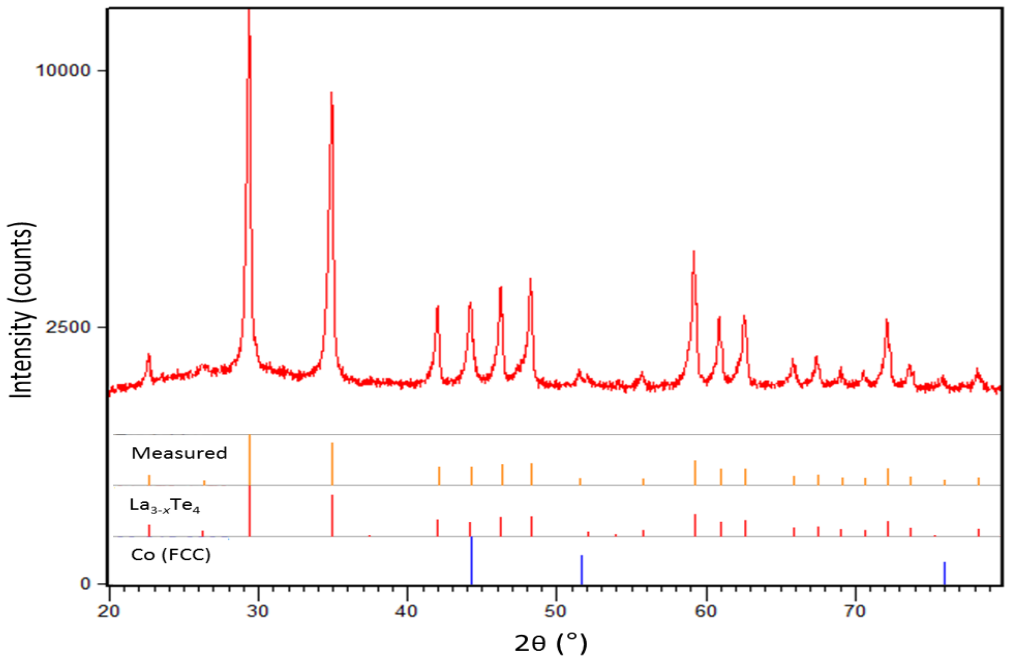

Figure 3.4 PXRD pattern of the $LaTe_{1.46}$-Co composite containing 12% cobalt. The peaks in the pattern match that of $La_{3-x}Te_4$ and the cobalt face-centered cubic (FCC) phase. No evidence of

the low temperature hexagonal closed packed (HCP) phase was observed. Reference patterns for $La_{3-x}Te_4$ and FCC Co are shown at the bottom.

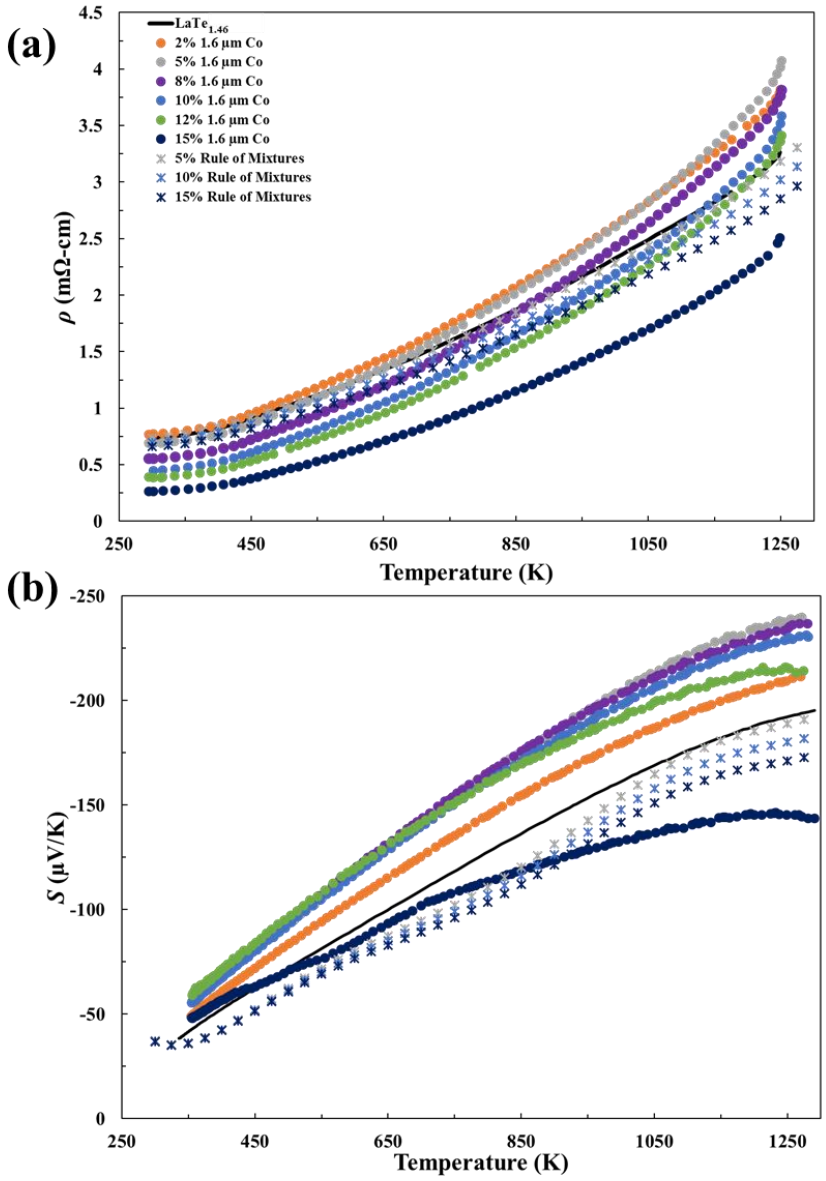

Figure 3.5 Temperature-dependent (a) electrical resistivity and (b) Seebeck coefficient measurements. A reduction in the low temperature resistivity occurred at 8%, but composites with 12% cobalt and below had resistivities higher than $LaTe_{1.46}$ at elevated temperature. The Seebeck coefficient increased over $LaTe_{1.46}$ for the 2-12% composites, peaking at 5 and 8 vol%.

The power factor (σS^2) of the composites was calculated from resistivity and Seebeck measurements (Figure 3.6). All samples exhibited higher power factors than $LaTe_{1.46}$ below 1000 K. Above 1000 K, the 15% composite had the lowest power factor of all measured samples due to its Seebeck coefficient being relatively flat until 1275 K. For the 2-12 vol% samples, σS^2 increased with increasing cobalt concentration. A significant increase occurs between 2 and 5% resulting from the corresponding increase in the Seebeck coefficients. The 12% composite exhibited the highest power factor of 18.8 μW cm^{-2} K^{-2} at 775 K, representing a 60% improvement over the peak value for $LaTe_{1.46}$. However, in the temperature range of interest (>1200 K), the power factors for the 5-12% composites were all similar, ~14 μW cm^{-2} K^{-2}, which is 20% higher than the parent $LaTe_{1.46}$.

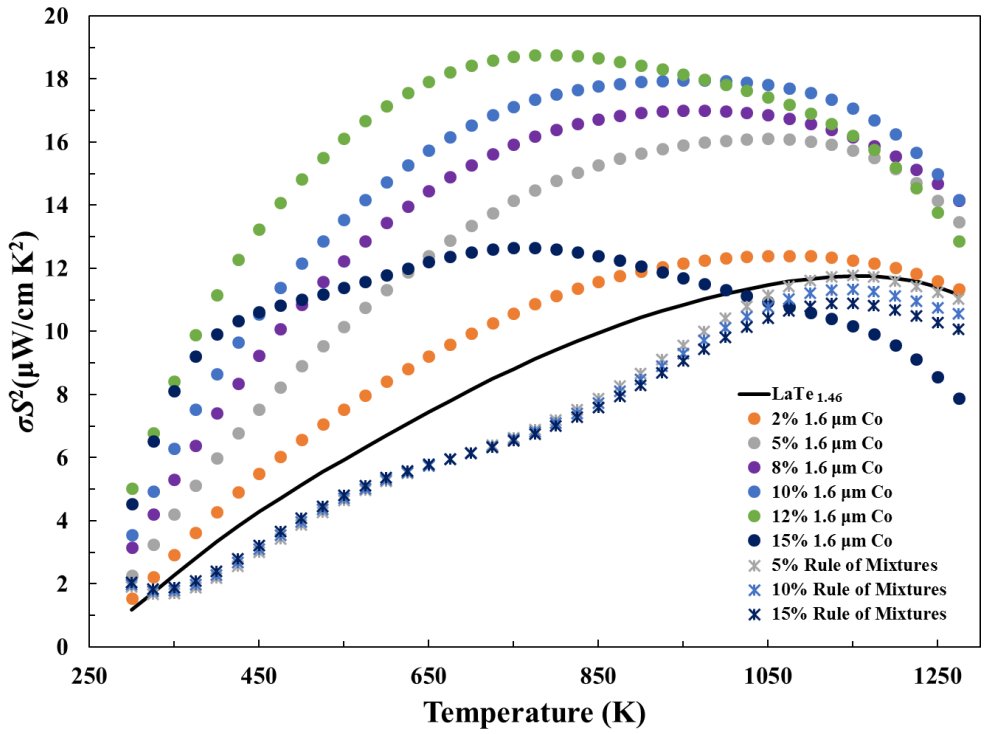

Figure 3.6 Temperature-dependent power factor (σS^2) for $LaTe_{1.46}$-Co composites from 0-15 vol%.

The specific heat capacity (c_p) of the 8% cobalt composite was measured using differential scanning calorimetry (Figure 3.7). As expected, the specific heat capacity is relatively constant as the temperature range investigated was significantly above the Debye temperatures of lanthanum telluride and cobalt.[13,19] Also plotted is the estimated specific heat calculated using the rule of mixtures, which combined the measured values of $LaTe_{1.46}$ and values for cobalt obtained from the National Institute of Standards and Technology (NIST).[21] The measured and estimated heat capacity values were found to be in good agreement with one another, similar to what was observed in Chapter 2 with the 15% $LaTe_{1.46}$-Ni composites. Since the rule of mixtures was a good approximation for temperature-dependent heat capacities, the approximated specific heat capacities were used in subsequent calculations.

Thermal diffusivity (D) and density (ρ) measurements were performed on the composites and the thermal conductivities were calculated using the relationship $\kappa = c_p \rho D$ (Figure 3.8). From 0-8 vol% cobalt, the thermal conductivities of the composites are similar to that of the parent $LaTe_{1.46}$. At 10 vol% and above, the thermal conductivities increased with increasing cobalt concentration. This behavior is similar to what was seen in $LaTe_{1.46}$-Ni composites, where the thermal conductivities remained invariant until above 10 vol%.[6] The increase in thermal conductivity was expected, as the lower resistivity of the cobalt inclusions in comparison to the matrix would increase the electronic contribution to the thermal conductivity. Lattice thermal conductivities of the composites were calculated using the Wiedemann-Franz law. A temperature-dependent Lorenz number was calculated using a single parabolic band (SPB) approximation.[21] The lattice contributions for the 2 and 5% composites were similar to that of $LaTe_{1.46}$. Deviations in the thermal conductivity were observed in the 8% composite and increased with higher cobalt loading fractions. This likely results from the composites' departure

from the Wiedemann-Franz law due to the decreasing resistivities. Additionally, $La_{3-x}Te_4$ is a known multiband system, which leads to inaccuracies in the SPB model and calculated Lorenz number.[22] Therefore, taking into account only the composites with the smallest loading fractions, 2- 5%, the similarities of the lattice contributions to $LaTe_{1.46}$ suggests that the increases in the total thermal conductivities seen in the other composites are due to changes in the electronic contributions.

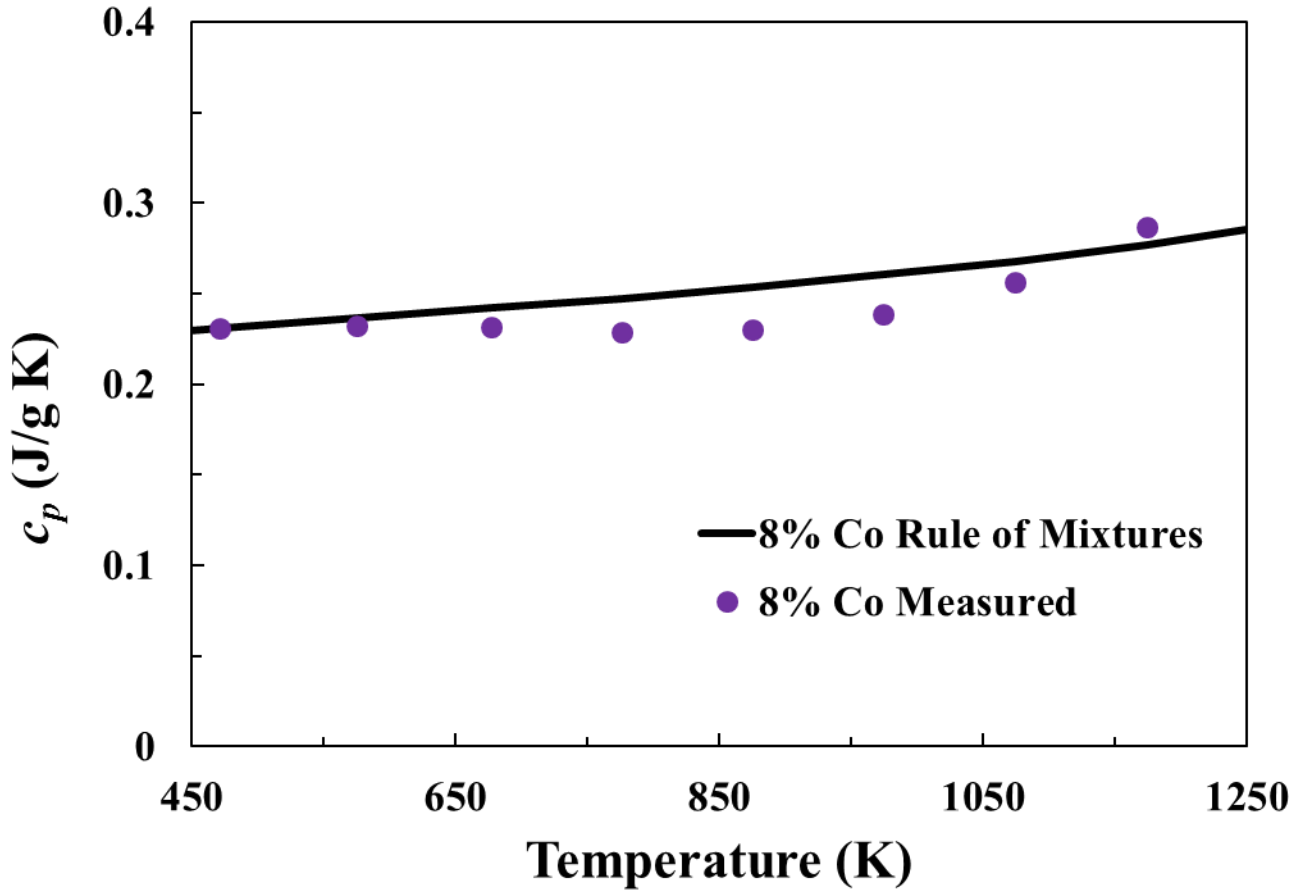

Figure 3.7 High-temperature specific heat capacity (c_p) of 8 vol% $LaTe_{1.46}$-Co composite. The measured heat capacity agreed well with the heat capacity estimated using the rule of mixtures from the heat capacities of $LaTe_{1.46}$ and cobalt.

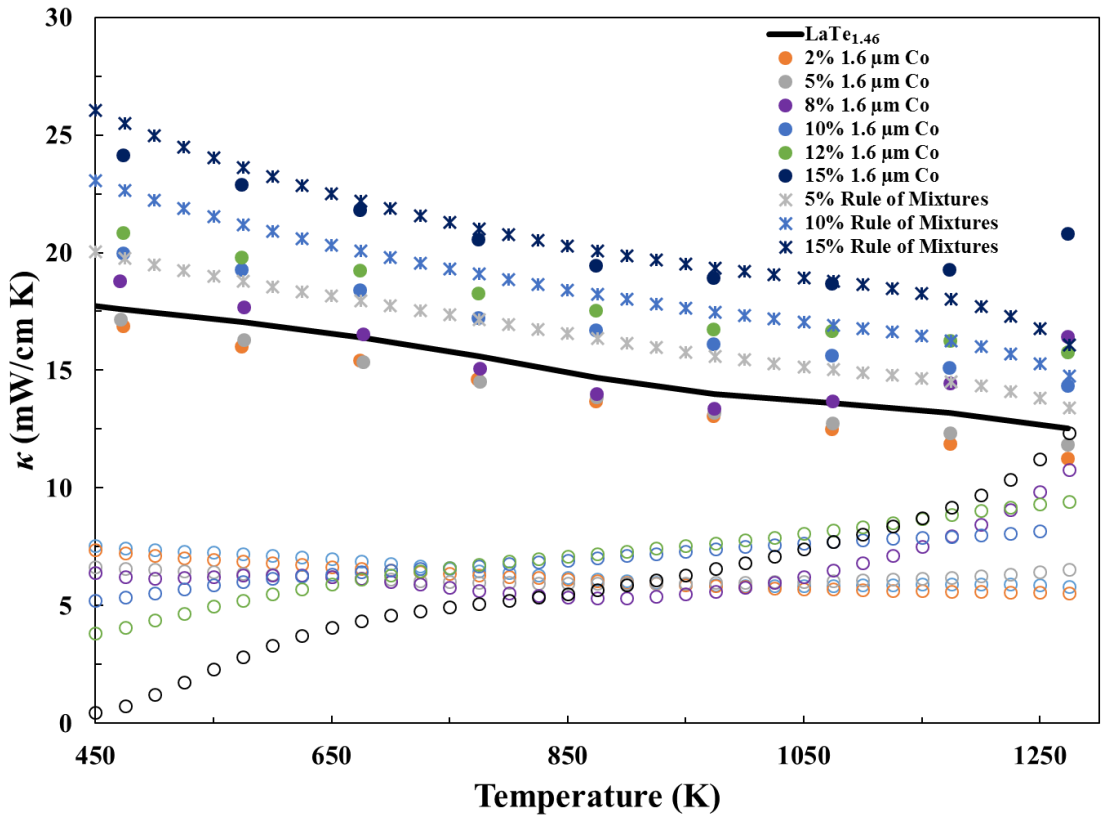

Figure 3.8 Temperature-dependent thermal conductivity of $LaTe_{1.46}$-Co composites. The lattice contributions to the total thermal conductivity were calculated using the Wiedemann-Franz law and are represented by open symbols.

ZT was calculated using the measured thermoelectric properties of the composites (Figure 3.9). A loading fraction of 15 vol% detrimentally affected *ZT* as the composite had a higher thermal conductivity and lower power factor above 1000 K. The *ZT*s of the other composites were found to have peak values similar to or higher than that of the baseline material. Optimization of *ZT* occurred at 5 vol% cobalt and achieved a maximum value of 1.5 at 1225 K. This is a 25% improvement over $LaTe_{1.46}$, largely resulting from the 18% improvement in the Seebeck coefficient and the unchanged thermal conductivity. Above 5 vol%, the other composites benefitted from increased Seebeck coefficients, but increases in the thermal

conductivities caused the *ZT*s to gradually decrease. The *ZT* of the 2% sample increased compared to the baseline due to the improved Seebeck coefficient.

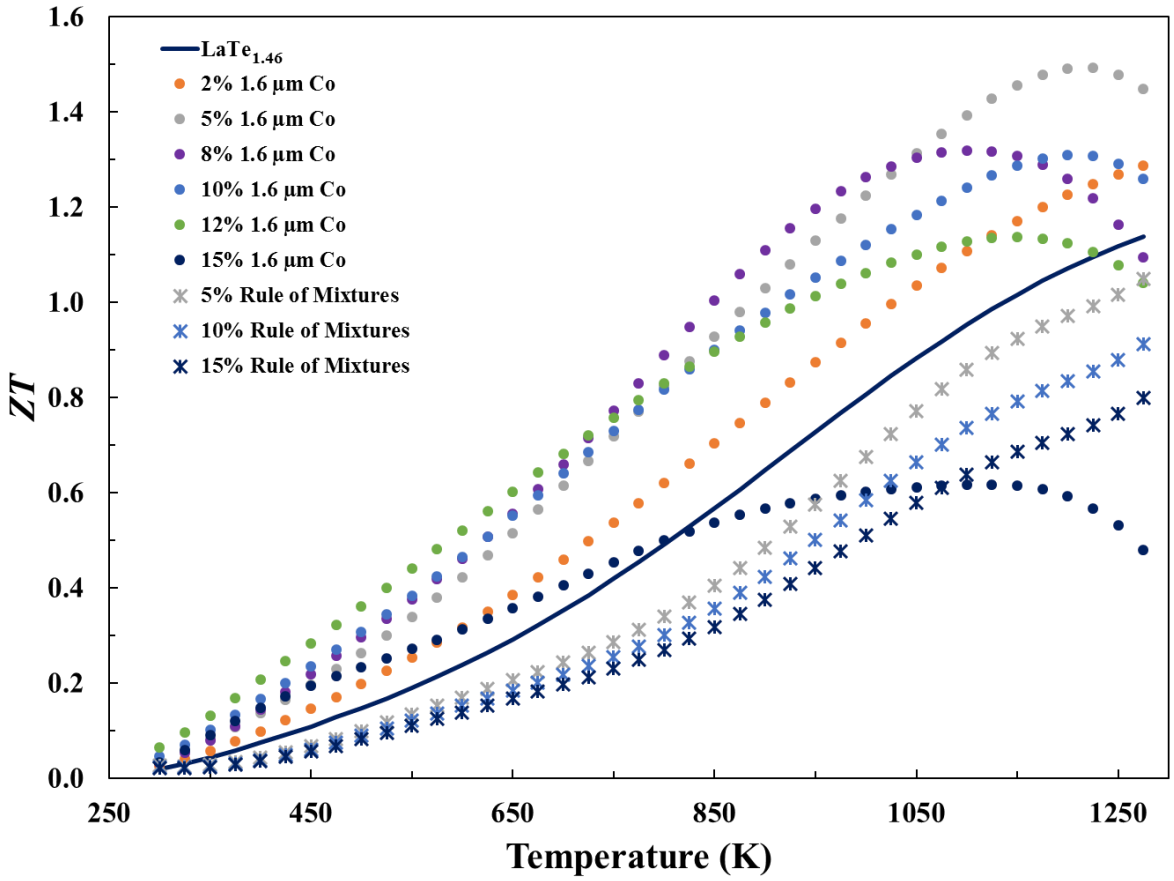

Figure 3.9 Dimensionless thermoelectric figure of merit (*ZT*) as a function of temperature for the $LaTe_{1.46}$-Co composites. A propagated error of 30% was calculated for *ZT*.

3.4. Conclusions

A series of $LaTe_{1.46}$-Co composite materials, ranging from 0-15 vol% cobalt, were synthesized and their thermoelectric properties were investigated. The microstructures of the cobalt composites were less homogeneous than the $LaTe_{1.46}$-Ni composites, and contained areas of the matrix with a minimal number of cobalt inclusions. This difference was initially attributed

to cobalt and nickel having different structures at room temperature, HCP and FCC, respectively. However, as the structure of cobalt was identified as FCC through PXRD, the reason behind the differences in microstructure is still unknown. Electrical resistivity measurements were performed and the high-temperature resistivity of the composites were found to increase compared to $LaTe_{1.46}$ but decreased with increasing cobalt vol%. This suggested competing effects were occurring between the CAFE effect and a reaction with CoO on the surface of the cobalt powder. The Seebeck coefficient of the composites also increased, showing an 18% improvement between 5-8 vol% cobalt, and then decreased as the resistivities began to decrease significantly. The increase in Seebeck coefficient further supported that a reaction occurred between the $LaTe_{1.46}$ and CoO, which altered the carrier concentration on the $LaTe_{1.46}$ matrix. The thermal conductivities of the composites above 8 vol% increased with increasing cobalt concentration. The calculated lattice contributions to the thermal conductivities were found to be similar to $LaTe_{1.46}$ for the 2 and 5%, but began to diverge at higher cobalt concentrations due to deviations from the Wiedemann-Franz law. All composites except the15 vol% sample were found to have peak *ZT* values similar to or greater than that of $LaTe_{1.46}$ due to the increased Seebeck coefficients of the composites. The 5 vol% composite had the highest *ZT,* 1.5 at 1225 K. This represents a 25% improvement of *ZT* compared to $LaTe_{.146}$.

3.5. References

[1] K. T. Kim, H. Y. Koo, G.-G. Lee, G. H. Ha, *Materials Letters*, **2012**, *85*, 141.

[2] M.S. Dresselhaus, G. Chen, Z.F. Ren, G. Dresselhaus, A. Henry, and J.-P. Fleurial, *JOM*, **2009**, *61*, 86.

[3] K. T. Kim, S. Y. Choi, E. H. Shin, K. S. Moon, H. Y. Koo, G.-G. Lee, G. H. Ha, *Carbon*, **2013**, *52*, 541.

[4] J. P. Heremans, and C. M. Jaworski, *Appl. Phys. Lett.*, **2008**, *93*, 122107.

[5] J. M. Ma, *Improving the Mechanical Strength and Power Conversion Efficiency of High Temperature Thermoelectrics*, Doctoral Dissertation, University of California, Los Angeles, **2014**

[6] G. J. Snyder and E. S. Toberer, *Nature Materials*, **2008**, *7*, 105.

[7] J. M. Ma, P. von Allmen, S. V. Prikhodko, T. Vo, R. B. Kaner, S. K. Bux, and J-P. Fleruial, "Composite Assisted Funneling of Electrons (CAFE) for Improved Performance of Bulk Thermoelectric Materials" *Submission Pending*.

[8] J.-P. Fleurial, K. Johnson, J. Mondt, J. Sakamoto, J. Snyder, C.-K. Huang, R. Blair, G. Stapfer, T. Caillat, P. Frye, W. Determan, B. Heshmatpour, M. Brooks, and K. Tuttle, *Development of Segmented Thermoelectric Multicouple Converter Technology*, **2006**, IEEE Aerospace Conference, Big Sky, MT

[9] T. Caillat, J.-P. Fleurial, G. J. Snyder, and A. Borshchevsky, *Development of High Efficiency Segmented Thermoelectric Unicouples*, **2001**, 20th International Conference on Thermoelectrics, Beijing, China

[10] G. J. Snyder and T. S. Ursell, *Physical Review Letters* **2003,** *91*, 148301.

[11] J.-P. Fleurial, B. J. Nesmith, R. C. Ewell, D. F. Woerner, G. C. Carr and L. E. Jones, *Thermoelectrics: From Space Power Systems to Terrestrial Waste Heat Recovery Applications*, **2011,** Thermoelectrics Application Workshop, DOE, San Diego, CA.

[12] W. M. Haynes, *CRC Handbook of Chemistry and Physics*, **2017**, CRC Press, 97th edition.

[13] A. F. May, J.-P. Fleurial, and G. J. Snyder, *Phys. Rev. B*, **2008**, *78*, 125205.

[14] K. A. Borup, E. S. Toberer, L. D. Zoltan, G, Nakatsukasa, M. Errico, J.P. Fleurial, B. Iversen, and G. J. Snyder, *Rev. of Sci. Inst.*, **2012**, *83*, 123902.

[15] C. Wood, D. Zoltan, and G. Stapfer, *Rev. Sci. Inst.*, **1985**, *56*, 5.

[16] F. Cardellini and G. Mazzon, *Philosophical Magazine A*, **1993**, *67*, 1289.

[17] W. D. Callister and D. G. Rethwicsh, *Fundamentals of Materials Science and Engineering*, **2010**, Wiley, 8th edition.

[18] M. Cutler, J. F. Leavy, and R. L. Fitzpatrick, *Phys. Rev.*, **1964**, *133*, A1143.

[19] G. R. Stewart, *Rev. Sci. Instrum.*, **1983**, *54*, 1.

[20] National Institute of Standards and Technology, *NIST Chemistry WebBook*, Accessed September **2015** (http://webbook.nist.gov/)

[21] H.-S. Kim, Z. M. Gibbs, Y. Tang, H. Wang and G. J. Snyder, *APL Mater.*, **2015**, *3*, 041506.

[22] A. F. May, D. J. Singh, and G. J. Snyder, **2009**, *Phys. Rev. B,* 79, 153101.

Chapter 4: Praseodymium Telluride as a High-Temperature, High *ZT* Thermoelectric Material

4.1. Introduction and Background

Band structure modifications to materials can have a profound effect on the thermoelectric performance of materials, specifically on the Seebeck coefficient.[1-4] Equation 1.6 shows that in the case of metals and degenerate semiconductors, the Seebeck coefficient is dependent on temperature and carrier concentration. A general form of equation 1.6 is the Mott relation which, for a single band metal, can be written as:

$$S = \frac{\pi^2 k_B^2 T}{3e}\left(\frac{d\ ln\ N(E)}{dE} + \frac{d \ln \tau(E) v(E)^2}{dE}\right)_{E=E_f} \quad (4.1)$$

where k_B is the Boltzmann constant, T is absolute temperature, e is the charge of an electron, N is the density of state, τ is relaxation time, ν is the average electron velocity, E is energy, and E_f is the Fermi level. Equation 4.1 shows that high band degeneracy near the Fermi level is desirable, as this will promote a sharp peak in the density of states ultimately increasing the Seebeck coefficient.

$La_{3-x}Te_4$ is able to achieve a high *ZT* of 1.1 largely in part due to its relatively high Seebeck coefficient at a high carrier concentration of approximately 1 x 10^{21} cm^{-3}.[1,5] The high Seebeck coefficient results from the sharp peak at the Fermi level near the conduction band edge in the La_3Te_4 density of states (Figure 4.1(a)). The total density of states in the conduction band is dominated by the states from the rare earth element whereas the valence band is comprised primarily of Te states (Figure 4.1(a)). The sharp peaks in the density of states for La_3Te_4 and

cerium telluride (Ce_3Te_4), coupled with the multiple flat bands near the Fermi level, result in both systems having similar thermoelectric properties and *ZT* values.[6]

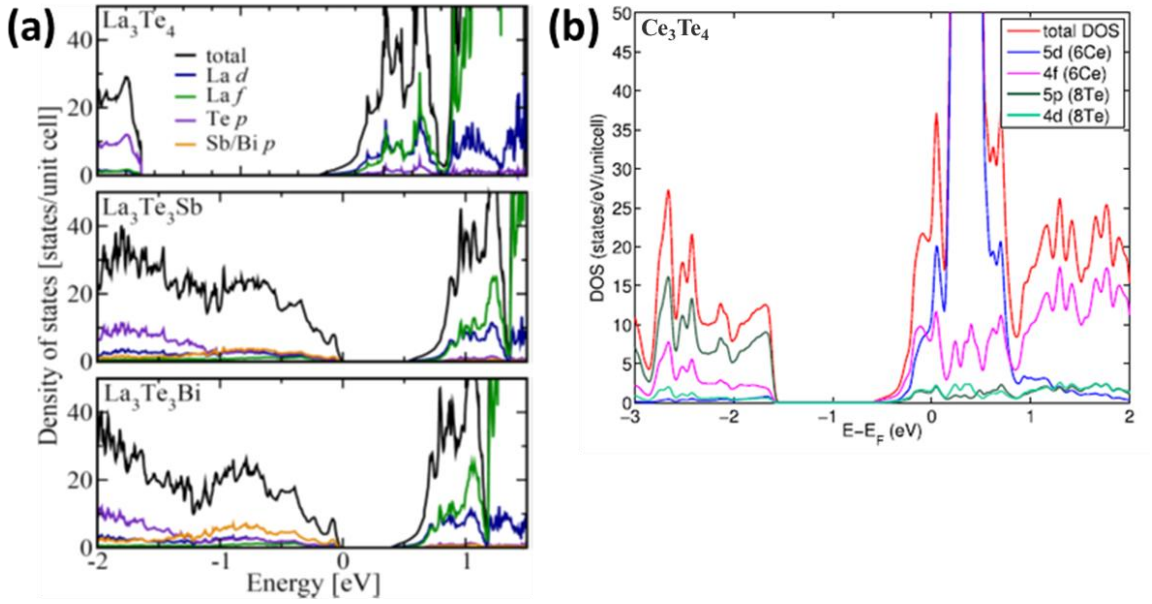

Figure 4.1 Density of states for (a) La_3Te_4 and (b) Ce_3Te_4. E_f is defined as zero in (a) and (b).[1,4]

Closer examination of the density of states for both La_3Te_4 and Ce_3Te_4 reveal that while the main contribution to the peak in the conduction band comes from the La *5d* orbital, there is also contribution from the *4f* orbitals. La has no *f* electrons, leaving the *4f* shell vacant, while Ce has one electron in the *4f* shell. As the 4*f* electrons are deep in the valence shell and lower in energy than the 5*p* or 6*s* orbitals, it is unsurprising that the *4f* contribution is limited compared to other orbitals. However, the *4f* states appear right at the Fermi level. An increase in the DOS or sharpening of the peak at the Fermi level could increase the Seebeck coefficient and thermoelectric performance of the material. One method to increase the contribution from the *4f* states is to move down the lanthanide series to praseodymium, which has a total valence of 3 electrons in the *4f* and *6s* valence shell.

Praseodymium telluride ($Pr_{3-x}Te_4$) and other rare-earth tellurides have been previously investigated for their high-temperature thermoelectric properties.[7,8] Melt or solid-state syntheses from elements were used extensively to synthesize these compounds.[9-11] However, these techniques require high temperatures (> 2000 K) and would often result in inhomogeneous samples. The large difference in the melting points between tellurium (722 K) and the rare-earth elements (1208 K for praseodymium) leads to loss of tellurium into the vapor phase, resulting in large deviations in stoichiometry from the nominal composition. Additionally, the oxygen sensitivities of the rare-earth elements and tellurides were problematic, exacerbated by the elevated temperatures required for synthesis. The lack of stoichiometric control led to reports with inconsistent properties for these compounds.[7,8] Recently, mechanochemical synthetic techniques were used to produce $La_{3-x}Te_4$ with stoichiometric control and highly reproducible thermoelectric propeties.[5] This method has yet to be applied to other rare-earth compounds and is of interest in order to verify the properties reported in previous literature.

In this work, the thermoelectric properties of $Pr_{3-x}Te_4$ were investigated. Density function theory (DFT) was used to calculate the electronic structure of Pr_3Te_4 to observe the effects of the *4f* electrons of praseodymium. It is hypothesized that the introduction of the *4f* electrons of praseodymium near the Fermi level will lead to an increase in the Seebeck coefficient compared to $La_{3-x}Te_4$. This increase in Seebeck is expected to also increase the *ZT* of $Pr_{3-x}Te_4$. A mechanochemical approach was used to synthesize samples with increasing vacancy concentrations. Compositional and microstructural analysis was performed on the compacts in addition to analysis of their electronic and thermal properties.

4.2. Pr_3Te_4 Electronic Structure

The structural relaxation and electronic properties of La_3Te_4 and Pr_3Te_4 were computed with the open source DFT software package Quantum Espresso (QE).[12] It is well known that the *f* states in rare-earth (RE) compounds are not adequately described by standard local density approximation (LDA) and generalized-gradient approximation (GGA) due to strong electronic correlation effects.[13,14] To address this shortcoming, PBE plus on-site Coulomb interaction (PBE+U) was used in this work.[15-18] The on-site Coulomb interaction serves to correct the self-interaction for the *f* electrons localized at the RE sites. Projected augmented wave (PAW) potentials generated with the AUTOPAW program were used for La, Pr with an energy cutoff of 60 Ry for the wave functions and a charge density cutoff of 540 Ry.[19-21] Since Pr_3Te_4 and La_3Te_4 are metallic, the Mazari-Vanderbilt smearing scheme is used to speed up the convergence toward self-consistency.[22] Brillouin zone k-point sampling of 13x13x13 and 17x17x17 are used for the structural relaxation and transport property calculations (Seebeck coefficient), respectively. The choice of energy cutoff and k-points is from the details of convergence tests.

Band engineering is one of the key tools for optimizing *ZT* of complex materials. An important difference between Pr_3Te_4 and La_3Te_4 is the presence of three additional *4f* electrons in praseodymium. We have studied the band structures and density of states (DOS) of these two materials to understand the extent the *4f* states affects the thermoelectric properties. Figure 4.2 compares the DOS of La_3Te_4 and Pr_3Te_4. The sharp peaks observed in the DOS of both compounds are mainly associated with the *4f* orbitals (see the discussion next paragraph). While the *4f* peak in La_3Te_4 is located far above the Fermi level, the *4f* peak in Pr_3Te_4 is situated near and at the Fermi level, resulting in a higher DOS in the energy range of interest to *n*-type thermoelectric materials. This enhancement in DOS at the Fermi level is one of the important

requirements for improving transport properties. However, for compounds containing *f* electrons, it is not always true that the transport property is increased by the presence of *f* electron. In order to have an enhanced transport property, the Fermi energy for the experimental value of the electron density should be close enough to the resonance in the DOS such that band contributions to *ZT* become dominant. An example of this observation can be found for the case of Ce_3Te_4, where the *4f* peak is too far from the Fermi level to significant contribute to Seebeck coefficient at practical experimental conditions.[4]

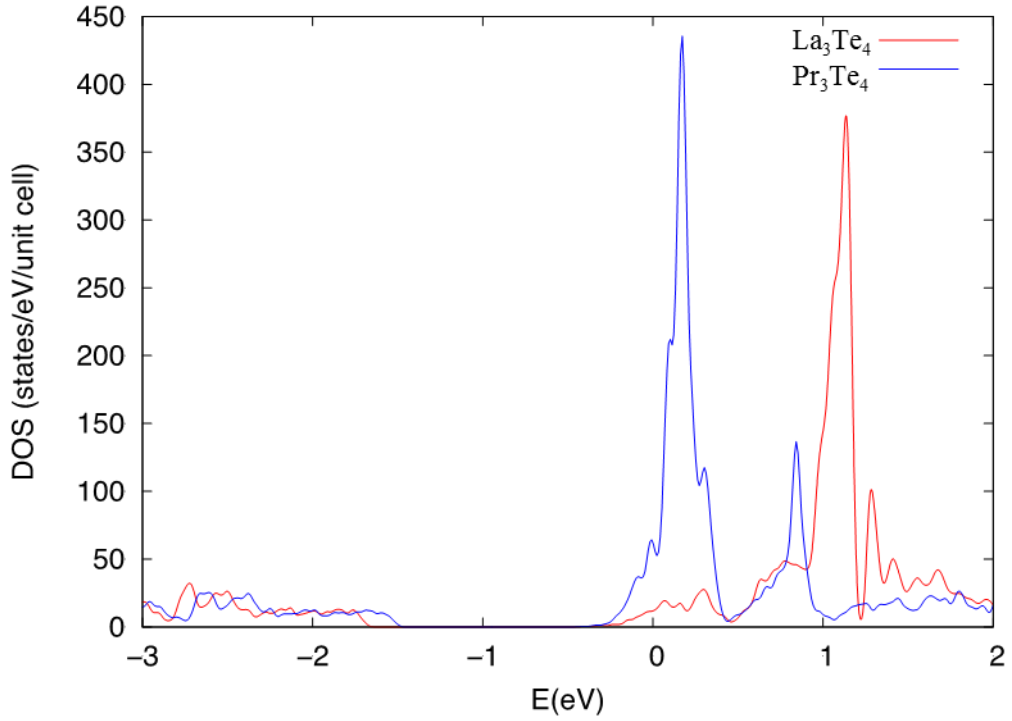

Figure 4.2 Comparison of density of states (DOS) of La_3Te_4 and Pr_3Te_4. The Fermi level is defined as $E_f = 0$ for both compounds.

The role of *4f* electrons on the electronic properties can be further investigated by comparing partial density of states (PDOS) of La_3Te_4 and Pr_3Te_4. As seen from Figure 4.3 and Figure 4.4, the main contribution to the DOS peak in the La_3Te_4 and Pr_3Te_4 comes from *4f* and *5d* orbitals of lanthanum and praseodymium, respectively. However, because the La *4f* peak in

La_3Te_4 is located far from the Fermi level, significant contribution to the DOS and thus transport property at and near the Fermi level relies mostly on La *5d* orbitals for La_3Te_4. On the other hand, although the two peaks (the large and small) observed in Pr_3Te_4 DOS are also mainly contributed by the *f* orbitals and *d* orbitals, the contribution from the *f* orbital dominates at the Fermi level. Consequently, for Pr_3Te_4 it is expected that the presence of three *4f* electrons in Pr atoms would enhance the transport properties, compared to lanthanum atoms with no electrons in the *4f* shells. In addition, Figures 4.3 and 4.4 also show a gap that separates the *f* peak from other lower energy states (with energy of less than ~1.4 eV) in both cases. The gap is ~0.91 eV for Pr_3Te_4, which is smaller than that of La_3Te_4 (~1.01 eV). While the main contribution to the DOS peak is the *4f* orbitals, far below the Fermi level in the valence band at the energy of ~ 1.4 eV, Te *5p* orbitals are found to contribute the most to the DOS.

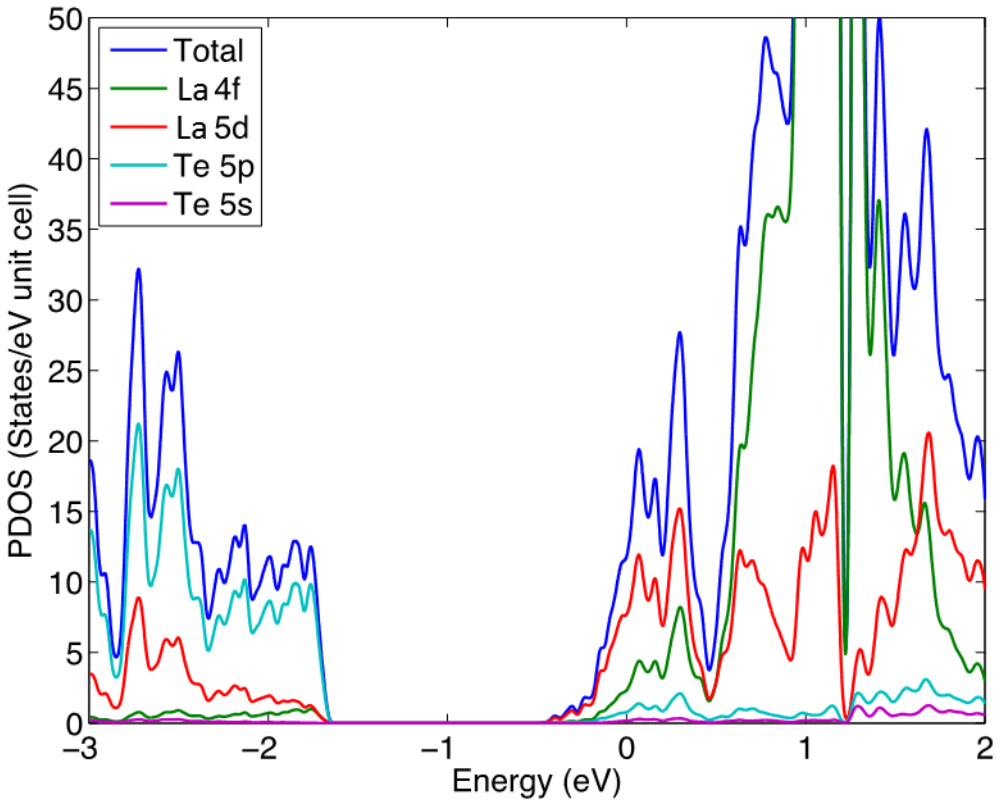

Figure 4.3 Partial density of states (PDOS) of La_3Te_4.

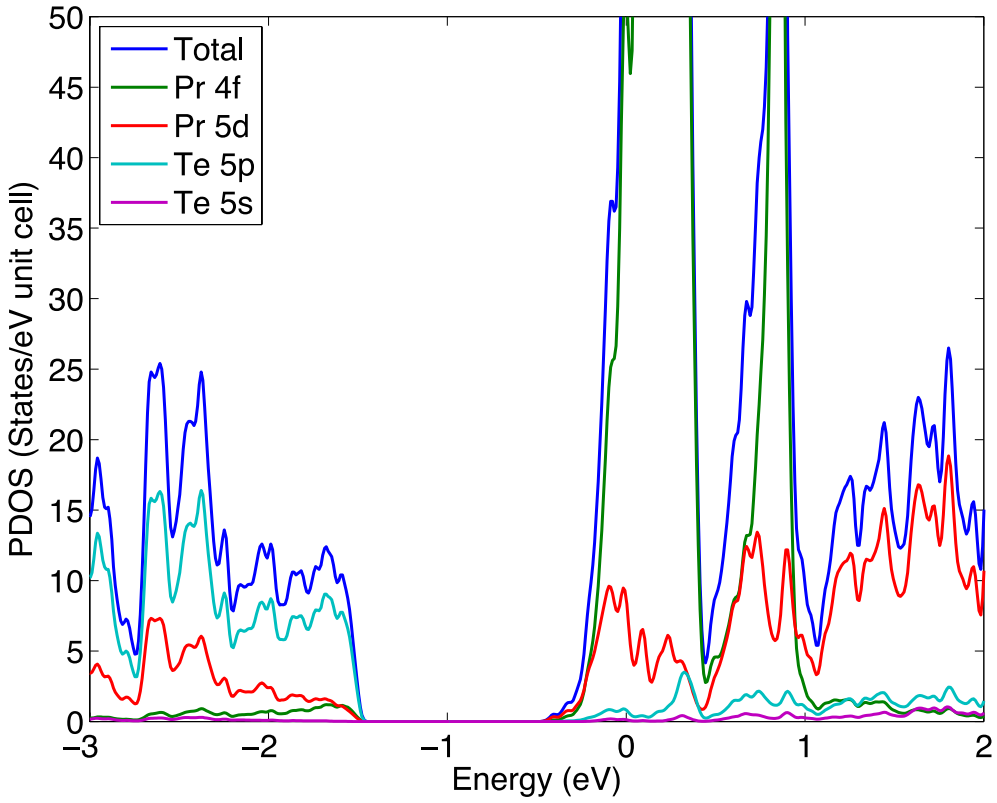

Figure 4.4 Partial density of states (PDOS) of Pr_3Te_4.

In order to have more insight into the difference in electronic properties bewteen La_3Te_4 and Pr_3Te_4, band structures of both compounds are examined. Figure 4.5 shows the band structures of La_3Te_4 and Pr_3Te_4. Slightly above the Fermi level in the band structure of Pr_3Te_4, a denser region of flat bands is observed, which originates from the *4f* orbitals of Pr atoms. Further above the Fermi level (~0.5 eV), significant changes in the band structure are also observed for the case of Pr_3Te_4, especially at the H, N, and γ points. The bands become flatter, and band degeneracy is changed dramatically. Due to the effect of *4f* orbitals, the bands at the γ point have smaller curvatures for the Pr_3Te_4 case than for La_3Te_4. Consequently, the effective masses are expected to be larger for Pr_3Te_4 than for La_3Te_4.

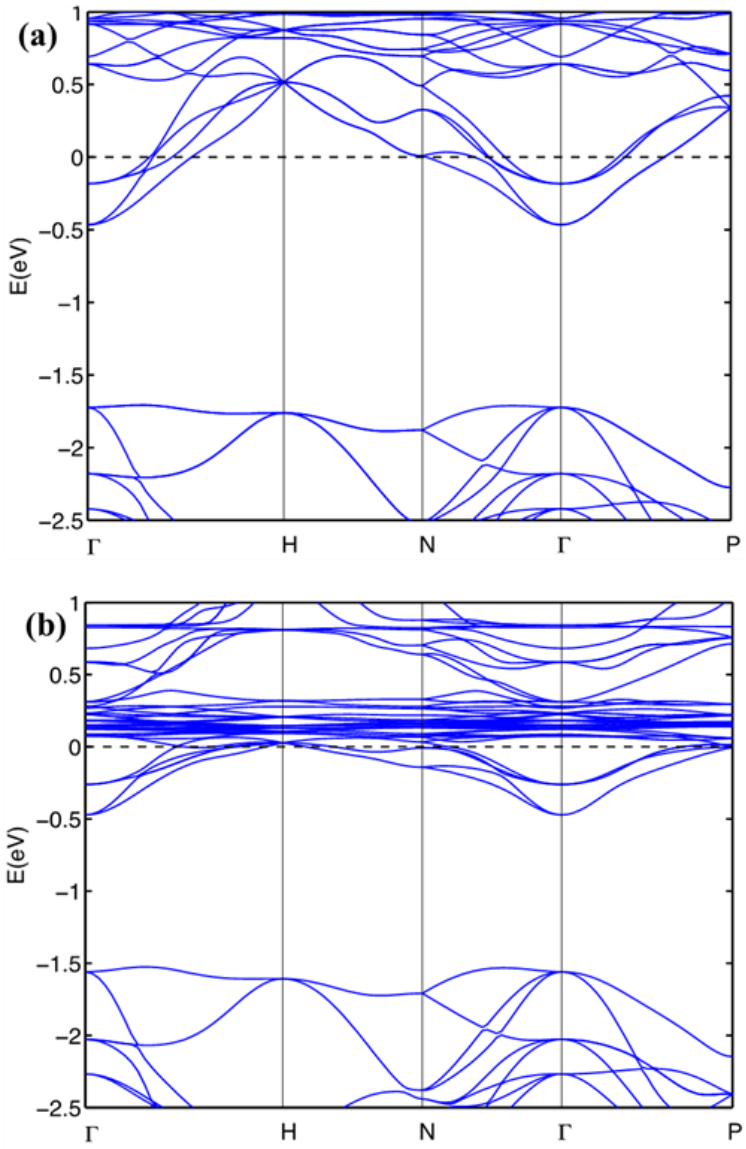

Figure 4.5 Calculated band structure diagrams of (a) La_3Te_4 and (b) Pr_3Te_4.

The Seebeck coefficients for Pr_3Te_4 and La_3Te_4 are computed using standard expressions derived from the linearized Boltzmann Transport Equation (BTE), and the rigid band approximation to describe the variation of electron concentration due to vacancies.[23-25] In the rigid band approximation, the band structure of the studied compounds is assumed to be unchanged when varying the electron concentration; only the position of the Fermi energy is adjusted. Figure 4.6 presents the Seebeck coefficients of Pr_3Te_4 as a function of temperature and

compostion. Here the Seebeck coefficient increases with increasing temperature and rare-earth vacancies. Figure 4.7 compares the Seebeck coefficient of both compounds. The plot shows larger Seebeck coefficients for Pr_3Te_4 than for La_3Te_4 for all carrier concentrations of interest (10^{20}-10^{22} cm^{-3}). The results are consistent with the increase in DOS due to the presence of *f* electrons observed near and at Fermi energy.

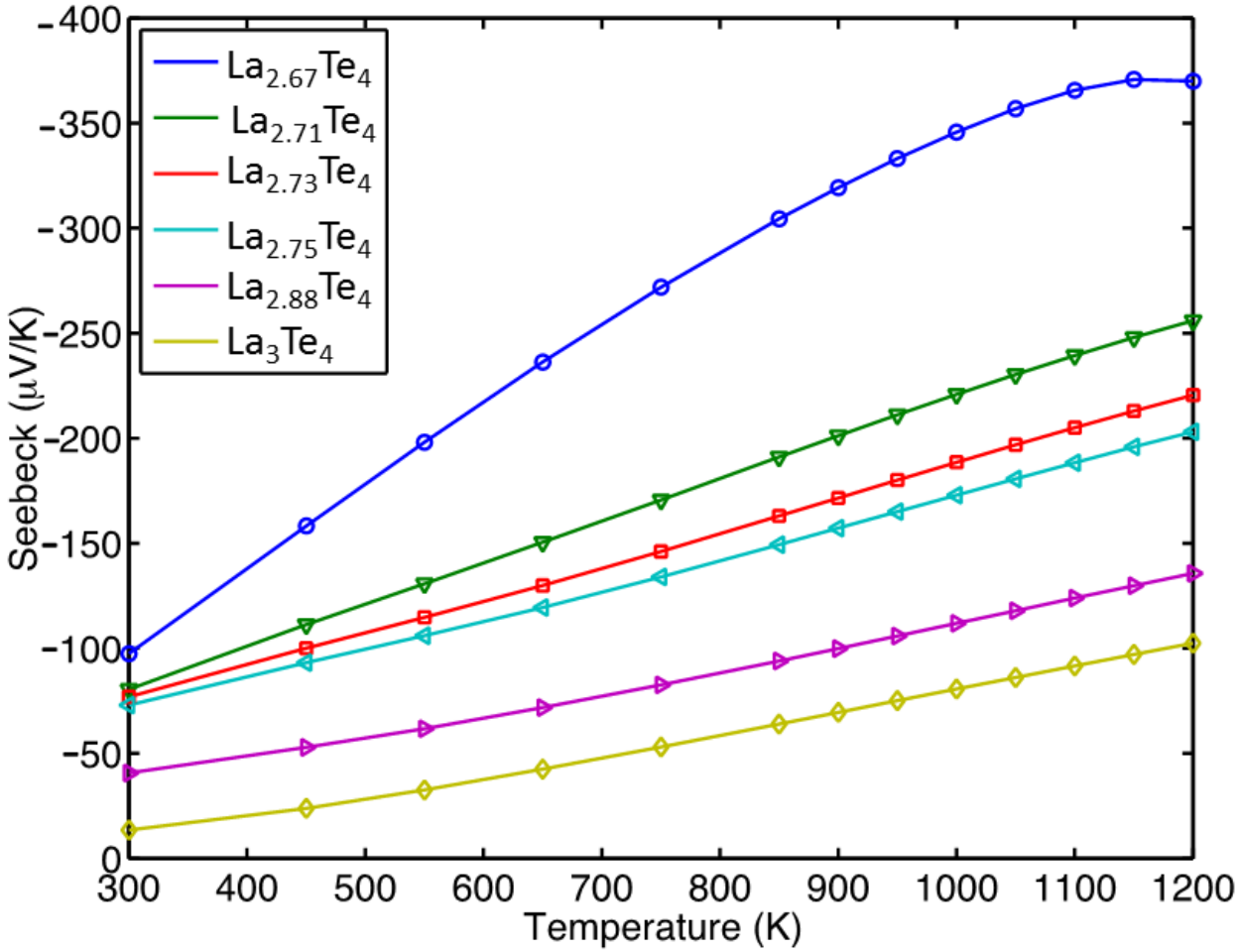

Figure 4.6 Seebeck coefficient of $Pr_{3-x}Te_4$ as a function of temperature and composition.

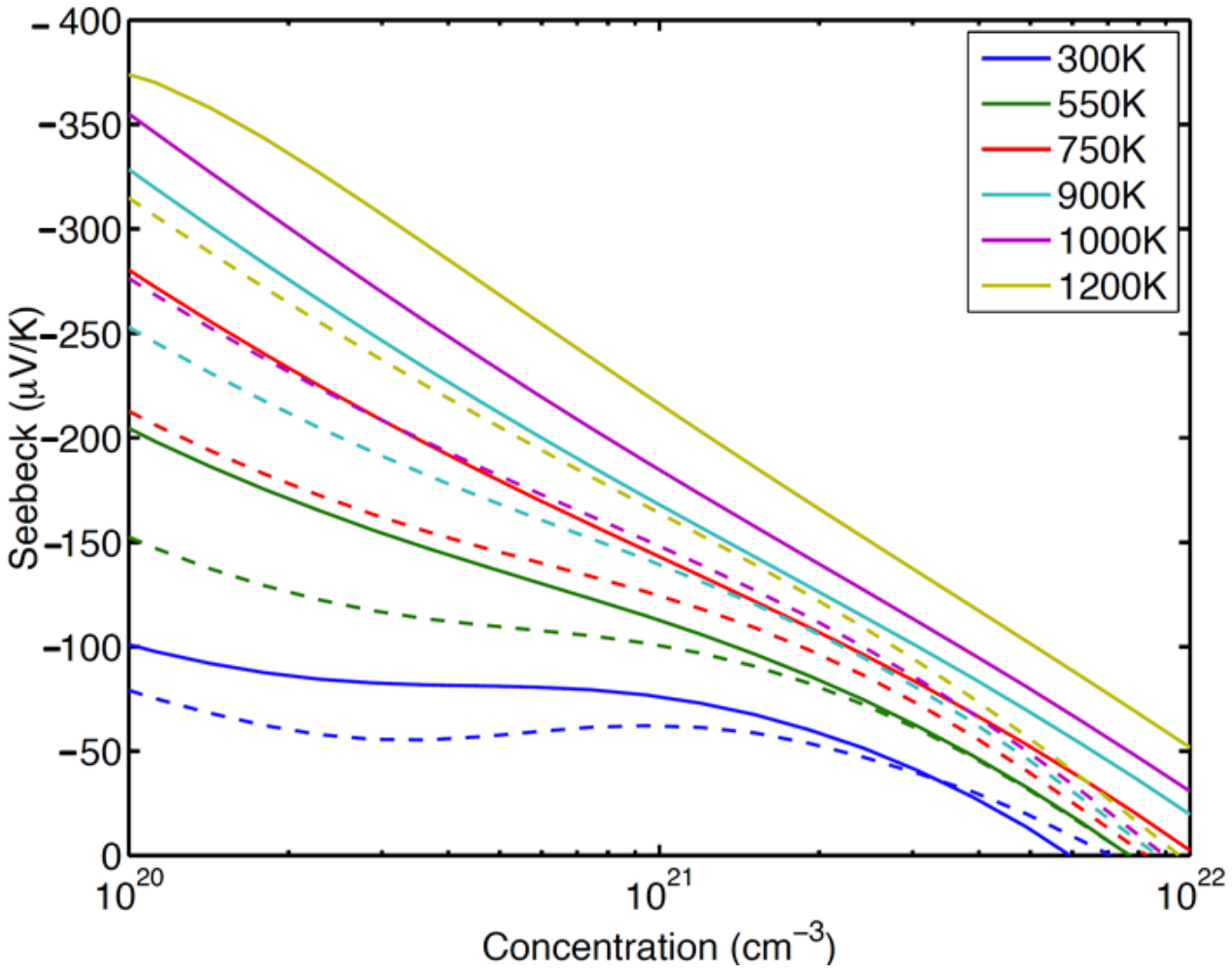

Figure 4.7 Seebeck coefficients of fully filled Pr_3Te_4 (solid line) and La_3Te_4 (dashed line) as function of carrier concentration. Pr_3Te_4 was found to have higher Seebeck coefficients in the carrier concentration and temperature ranges of interest.

4.3. Synthetic Methods

Praseodymium telluride was synthesized using a mechanochemical method previously used for making lanthanum telluride. The starting elements and synthesized powders were handled in an Ar-filled glovebox (H_2O < 1 ppm, O_2 < 0.1 ppm). Elemental Pr (99.9%, metals basis, Stanford Advanced Materials) was combined with Te (99.999%, 5N Plus) and sealed under argon in a stainless steel vial with stainless steel balls. A series of $Pr_{3-x}Te_4$ samples were prepared with varying vacancy concentrations of x = 0, 0.1, 0.14, 0.22, 0.26, 0.3, and 0.33. The vials were then placed in a ball mill and milled until a homogeneous $Pr_{3-x}Te_4$ powder was synthesized. The $Pr_{3-x}Te_4$ powders were then loaded into 12.7 mm graphite dies and compacted through spark plasma sintering (SPS) at temperatures above 1200 °C. The sintered compacts had densities greater than 98% of the theoretical density, measured using the Archimedes method.

Powder X-ray diffraction (PXRD) data was collected with a Phillips PANalytical X'Pert Pro diffractometer using Cu K_α radiation. Compacted samples were ground using a mortar and pestle and then mixed with Si powder (-325 mesh, 99.999%, Alfa Aesar) to use as an internal standard during Rietveld analysis. Due to the high air and moisture sensitivities of $Pr_{3-x}Te_4$, the powders were sealed with 1 mm thick Kapton film (McMaster-Carr) on a Si zero background holder under argon. Scans were performed over a 2θ range of 25–100°, with a 0.008° step size and a time of 4.15 seconds per step. Rietveld refinement was performed using the GSAS-II crystallographic data analysis software.[26] Structural data for the cubic phase with space group $I\bar{4}3d$ from Mitarov *et al.* was used for refinement.[27] In order to perform a stable refinement of the Pr occupancy, the occupancy on the Te position was held at 100% as no vacancies were expected.

Back-scattered electron (BSE) SEM was performed using a Zeiss 1550 VP SEM to observe phase homogeneity of the samples. Wavelength dispersive X-ray spectroscopy (WDS) using a JEOL JXA-8200 electron probe microanalyzer with $PrPO_4$ and elemental Te as standards was performed to confirm the elemental compositions of the sintered compacts. Ten points were measured for each sample and averaged to determine sample composition.

A custom built combined 4-point probe and Hall Effect system was used to measure the electrical resistivity.[28] The high-temperature Seebeck coefficient was measured using a custom-fabricated system.[29] Thermal diffusivity measurements were carried out using a commercial Netzsch LFA 457 laser flash analysis system. Differential scanning calorimetry (DSC) was performed to measure heat capacity using a Netzsch DSC 404. Experimental error in electrical resistivity, Seebeck, and thermal conductivity were found to be approximately 5, 20, and 10 % respectively, resulting in a propagated error in *ZT* of 30%.

High-temperature resonant ultrasound spectroscopy (RUS) measurements to 300 °C were performed on densified samples using a Mangaflux-RUS Quasar 4000 system under flowing argon to minimize oxidation with a frequency range of 0 to 500 kHz with 16.67 Hz step size. Data was analyzed using the Quasar2000 ClyModel software package.

4.4. Compositional and Structural Analyses of $Pr_{3-x}Te_4$

The diffraction pattern for the $Pr_{2.74}Te_4$ sample shown in Figure 4.8 is representative of the other samples. No secondary or oxide phases were detected and the pattern correlated with the previously reported Pr_3Te_4 pattern.[30] Phase homogeneity of the samples was further verified by the use of backscattered electron (BSE) SEM on samples consolidated by SPS. Micrographs for all samples are shown in Figure 4.9. These images were typical of all samples and the uniform contrast reflects the phase homogeneity of the compounds. The dark areas in Figure 4.9

stem from trace amount of residual porosity in the samples and the porosity was calculated to be between 2-5%.

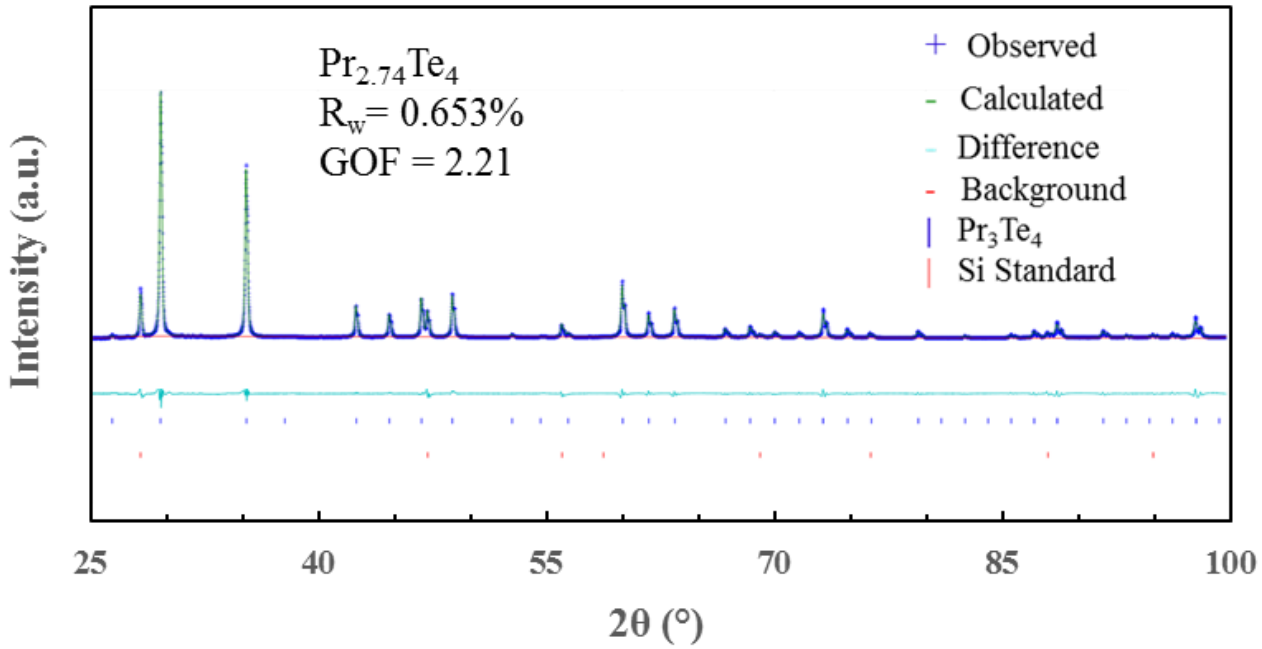

Figure 4.8 PXRD pattern of $Pr_{2.74}Te_4$ mixed with Si as an internal standard. Rietveld refinement was performed and the calculated pattern, difference curve, and theoretical peaks for Pr_3Te_4 and Si are shown.

To determine the composition of each sample, wavelength dispersive X-ray spectroscopy (on sintered samples) and Rietveld analysis (on ground compacts) were employed. The measured and refined values were compared to nominal compositions (Table 4.1). WDS and nominal compositions were in good agreement for all compositions, as were the values calculated from Rietveld for samples near the end-members of the compositional range. Rietveld analysis underestimated the vacancy concentrations for intermediate values. This was attributed to the PXRD scan quality not being high enough to accurately refine the fractional occupancy of the praseodymium site.

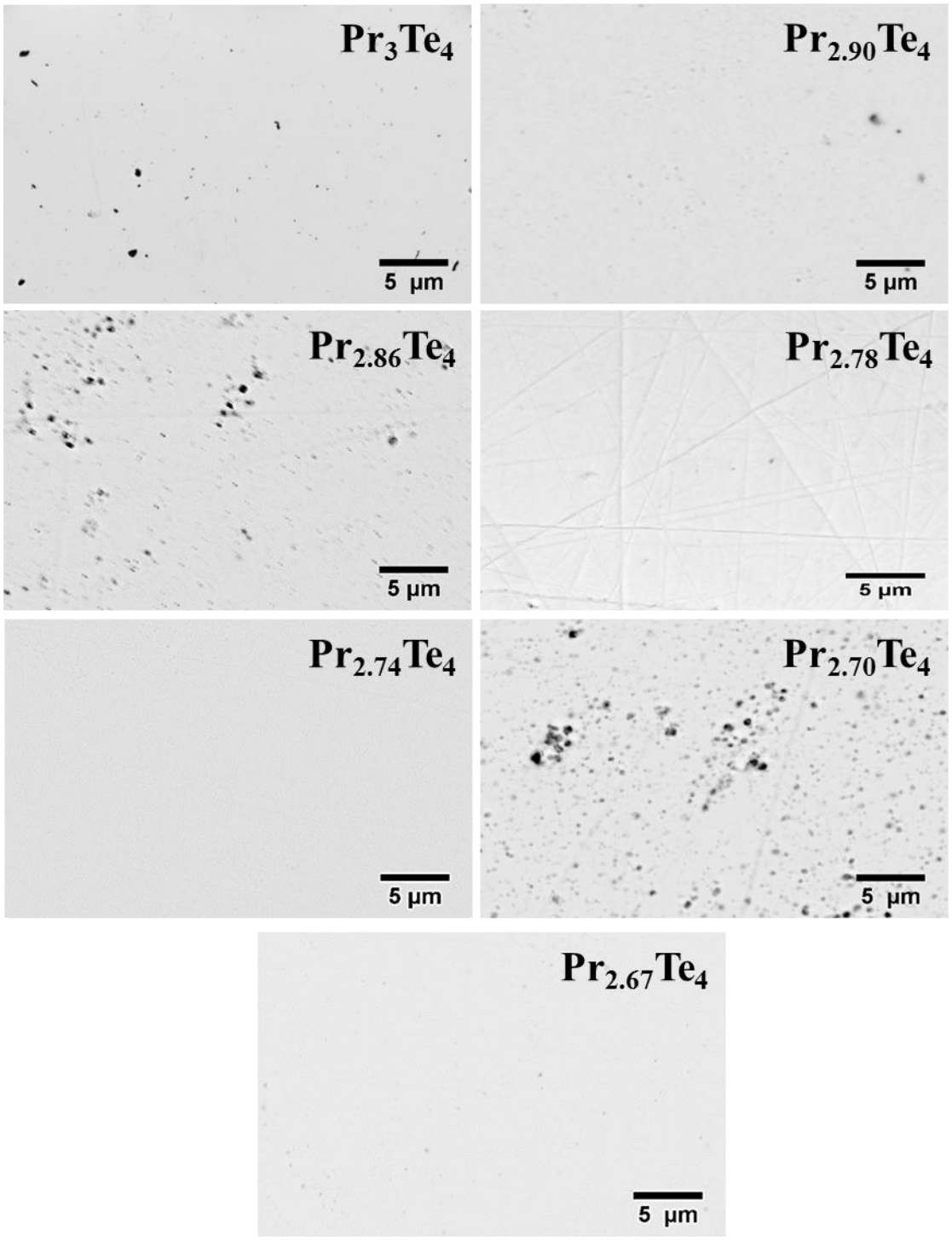

Figure 4.9 BSE SEM images of homogenous, phase pure $Pr_{3-x}Te_4$ compacts. The dark regions are from residual porosity in the samples.

Nominal Composition	WDS Composition	Rietveld Composition
Pr_3Te_4	$Pr_{3.03}Te_4$	$Pr_{2.97}Te_4$
$Pr_{2.90}Te_4$	$Pr_{2.93}Te_4$	$Pr_{2.92}Te_4$
$Pr_{2.86}Te_4$	$Pr_{2.86}Te_4$	$Pr_{2.91}Te_4$
$Pr_{2.78}Te_4$	$Pr_{2.78}Te_4$	$Pr_{2.86}Te_4$
$Pr_{2.74}Te_4$	$Pr_{2.78}Te_4$	$Pr_{2.79}Te_4$
$Pr_{2.70}Te_4$	$Pr_{2.70}Te_4$	$Pr_{2.68}Te_4$
$Pr_{2.67}Te_4$	$Pr_{2.61}Te_4$	$Pr_{2.67}Te_4$

Table 4.1 Nominal, WDS, and Rietveld compositions for $Pr_{3-x}Te_4$.

The lattice parameters for each sample were also refined using Rietveld analysis (Figure 4.10). There was little change in the lattice parameter between samples with minimum and maximum number of vacancies, which is consistent with prior structural investigations of $Pr_{3-x}Te_4$.[30,31] The small change in the lattice parameters of $La_{3-x}Te_4$ is also observed, however the mass density of $La_{3-x}Te_4$ is constant at 6.58 g cm^{-3} whereas that of $Pr_{3-x}Te_4$ changes depending on the vacancy concentration, 7.27 g cm^3 when $x = 0$ and 6.91 g cm^{-3} when $x = 0.33$.[6, 31-33] The difference in the trends in densities as a function of rare-earth atomic vacancies for these two materials is not well understood and warrants further investigation.

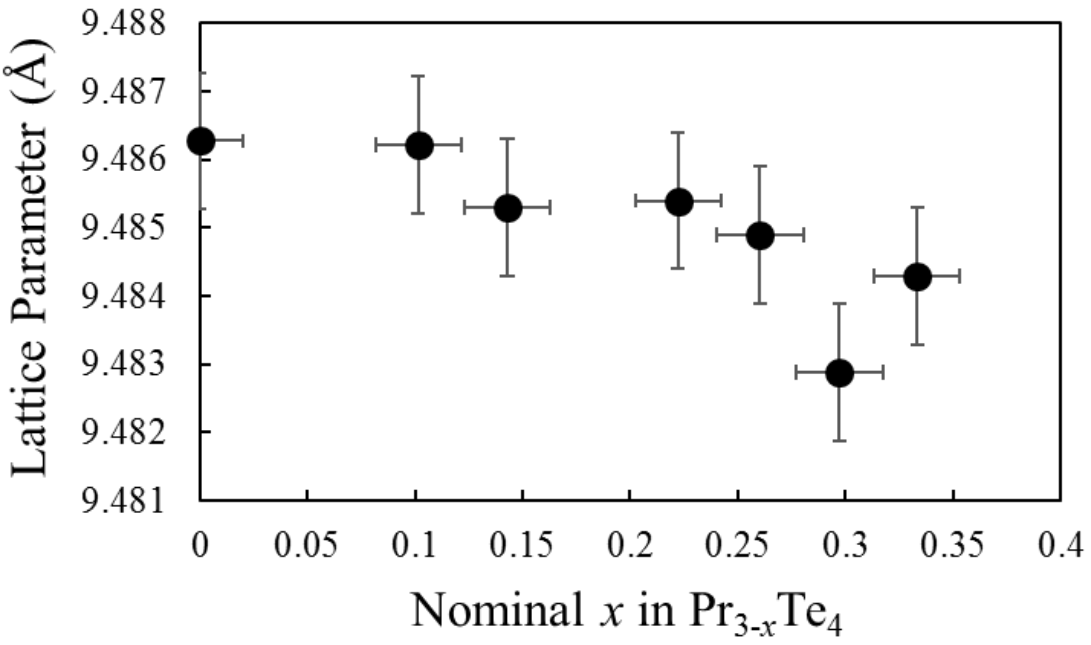

Figure 4.10 Lattice parameters calculated from Rietveld analysis as a function of vacancy concentration. Error bars in the lattice parameters represent the diffractometer limit of ±0.001Å and the error bars in *x* represent a 5% variation in stoichiometry.

4.5. Thermoelectric Properties of $Pr_{3-x}Te_4$

The room temperature carrier concentration was measured using the Hall effect method and these values were compared to the carrier concentrations calculated from the WDS composition (Figure 4.11). Good agreement was observed for samples with vacancy concentrations greater than $x = 0.22$. The carrier concentrations calculated from Hall effect measurements on samples with higher carrier concentrations were unreliable due to low carrier mobililties, approximately 7 cm^{-2} V^{-1} s^{-1}. The low mobility values resulted in a decreased Hall coefficient, which lowered the signal-to-noise ratio and reduced the accuracy of the measurement for higher carrier concentration samples (Figure 4.12).

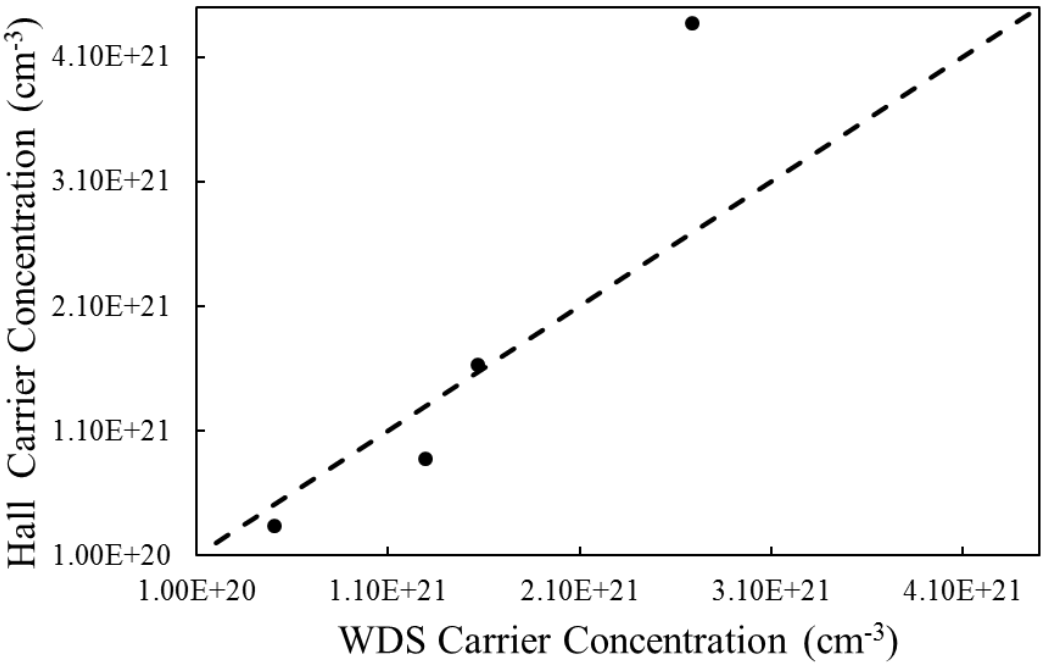

Figure 4.11 A comparison of the measured carrier concentrations with the concentrations calculated using the WDS composition. The theoretical carrier concentration prediction is denoted by the dashed line. Samples with higher carrier concentrations are not shown due to limitations in accurately measuring *n* for low mobility materials.

Electrical resistivity as a function of temperature was measured and compared with values previously reported for $La_{3-x}Te_4$ (Figure 4.13).[5] All samples exhibited behavior expected for a degenerately doped semiconductor where the resistivity increased with increasing temperature. The resistivities of the samples increased with increasing vacancy concentrations due to carrier concentration reductions. The low mobility of this system results in a low Hall coefficient and decreases the accuracy of the measurement by lowering the signal-to-noise ratio. This was apparent from the large spread in the lower vacancy concentration (higher carrier concentration) samples and the increasing accuracy of the measurement as the carrier concentration decreased. Measurements on samples with $x = 0.33$ were conducted, but the high

resistivity caused difficulties in making ohmic contacts between the sample and probe, resulting in inaccurate Van der Pauw resistivity values. The resistivity of the $Pr_{3-x}Te_4$ samples trends well with the values of $La_{3-x}Te_4$ for lower vacancy concentrations. However, at higher vacancy concentrations, the $Pr_{3-x}Te_4$ samples exhibit higher resistivity values than $La_{3-x}Te_4$ with equivalent vacancy concentrations.

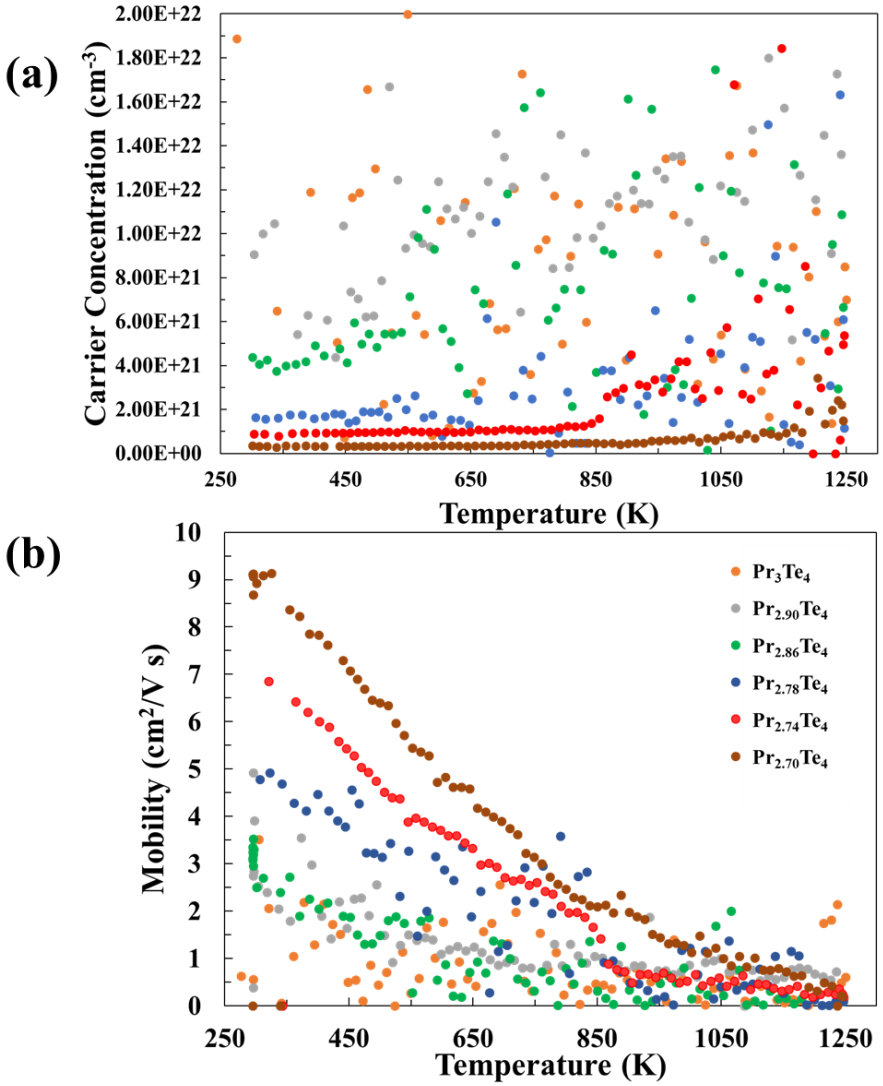

Figure 4.12 (a) High temperature carrier concentration results. The accuracy of the data increases as the carrier concentration decreases due to the increase in the carrier mobility and subsequent increase in the signal-to-noise ratio. (b) Temperature dependent Hall carrier mobility.

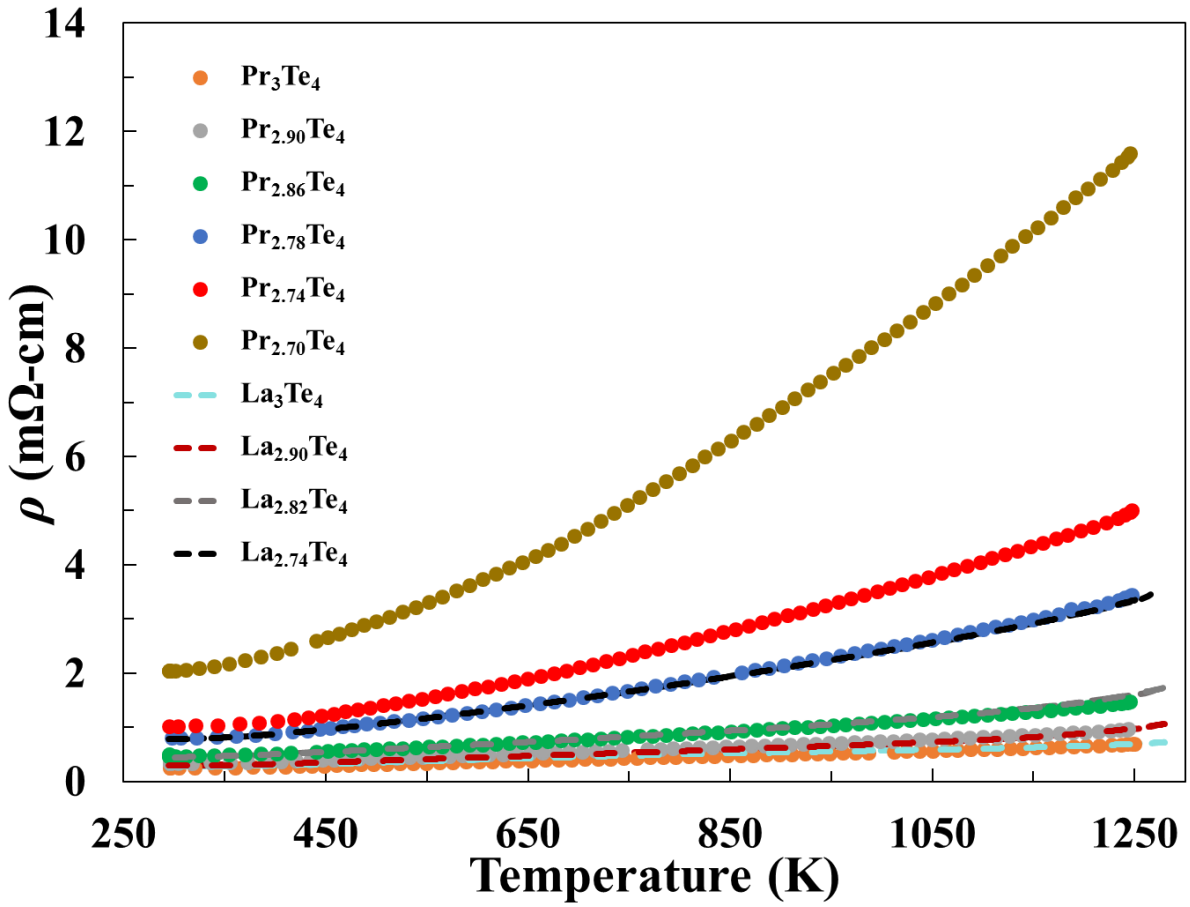

Figure 4.13 Temperature-dependent resistivity of $Pr_{3-x}Te_4$ samples compared to that of $La_{3-x}Te_4$.[5] The samples are indicated by their nominal compositions. The higher vacancy concentration $Pr_{3-x}Te_4$ samples had resistivties much higher than the equivalently vacancy-doped $La_{3-x}Te_4$ samples.

The Seebeck coefficient increased with increasing vacancies due to reductions in carrier concentration (Figure 4.14). Similar to what was observed with the high-temperature resistivities, the $Pr_{3-x}Te_4$ samples with lower vacancy concentrations were found to be similar to those of $La_{3-x}Te_4$. At higher vacancy concentrations the $Pr_{3-x}Te_4$ samples yielded higher Seebeck coefficient values compared to $La_{3-x}Te_4$. Specifically, the $Pr_{2.74}Te_4$ composition exhibited a 25% increase in the Seebeck coefficient when compared to $La_{2.74}Te_4$. At higher vacancy

concentrations, the improved Seebeck coefficient of $Pr_{3-x}Te_4$ resulted in an increased power factor (σS^2) over $La_{3-x}Te_4$ (Figure 4.15)

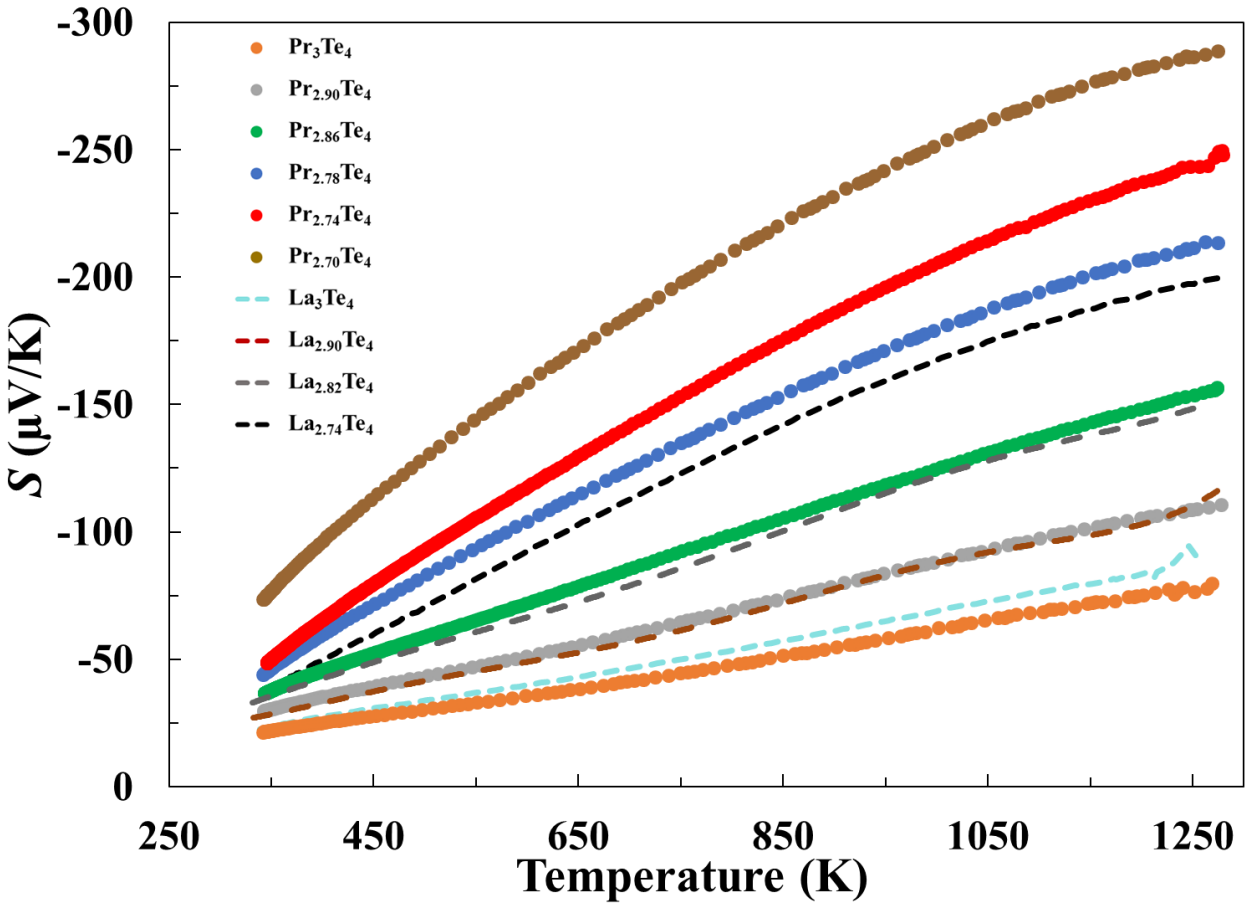

Figure 4.14 Seebeck coefficients as a function of temperature for $Pr_{3-x}Te_4$ and $La_{3-x}Te_4$ samples.[5] $Pr_{3-x}Te_4$ samples exhibited significantly larger Seebeck values compared to $La_{3-x}Te_4$ at higher vacancy concentrations.

An effective mass of $m^* = 3.5m_e$ and $2.13m_e$ were calculated for $Pr_{2.74}Te_4$ and $La_{2.74}Te_4$, respectively, using a single parabolic band model. An effective mass of $2.13m_e$ matches well with previously reported values for $La_{3-x}Te_4$, which range from 1.8 to $2.75m_e$.[5,7,24] The increased effective mass of $Pr_{2.74}Te_4$ over $La_{2.74}Te_4$ is consistent with the observed increase in the Seebeck

coefficient at equivalent vacancy concentrations and supports the hypothesis that the *4f* electrons modified the band structure favorably over that of $La_{3-x}Te_4$.

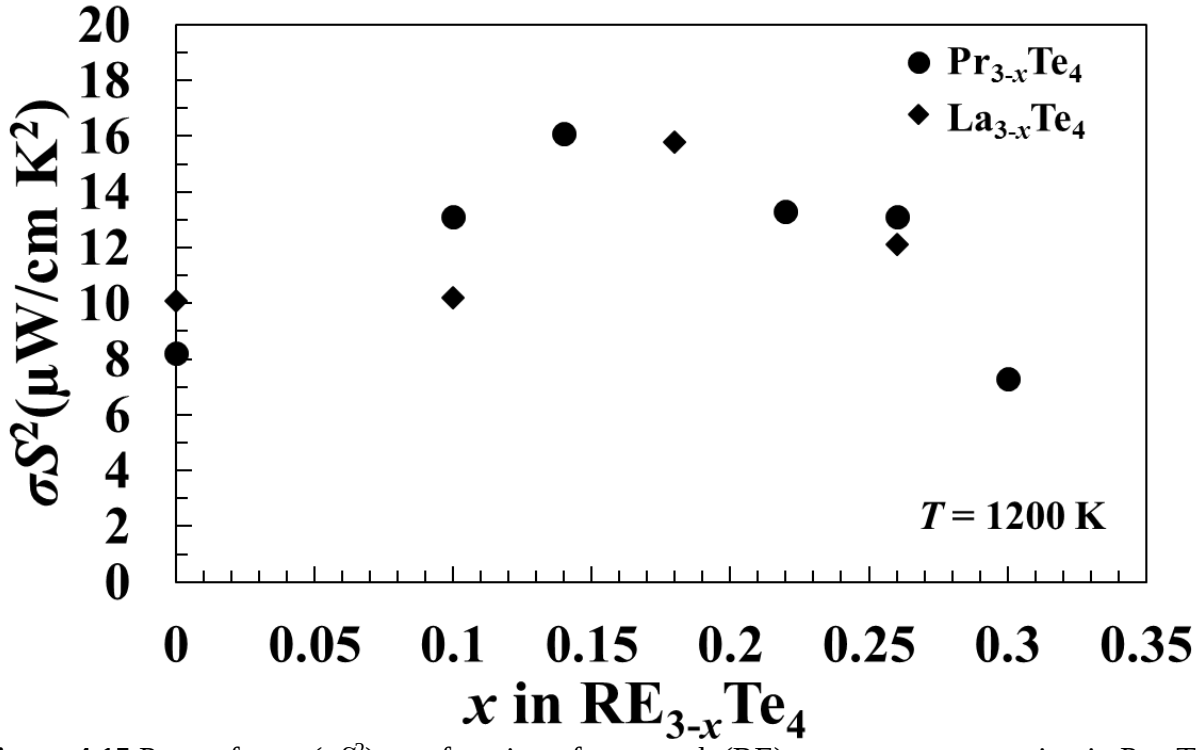

Figure 4.15 Power factor (σS^2) as a function of rare-earth (RE) vacancy concentration in $Pr_{3-x}Te_4$ compared to $La_{3-x}Te_4$ at 1200 K.[5] At higher vacancy concentrations $Pr_{3-x}Te_4$ exhibits an increased power factor over $La_{3-x}Te_4$.

The total thermal conductivity was calculated using the formula, $\kappa = DC_pd$, where D is the measured thermal diffusivity, C_p is the measured heat capacity, and d is sample density. Thermal conductivities range form 5-35 mW cm^{-1} K^{-1}, with the thermal conductivity decreasing with increasing vacancy concentration (Figure 4.16). This was expected as the total thermal conductivity is comprised of two components, the electronic and lattice contributions, $\kappa = \kappa_e + \kappa_L$. Therefore, the increased vacancy concentrations reduced the electronic term as carrier concentration decreased. This behavior is similar to that previously reported on $La_{3-x}Te_4$.[5]

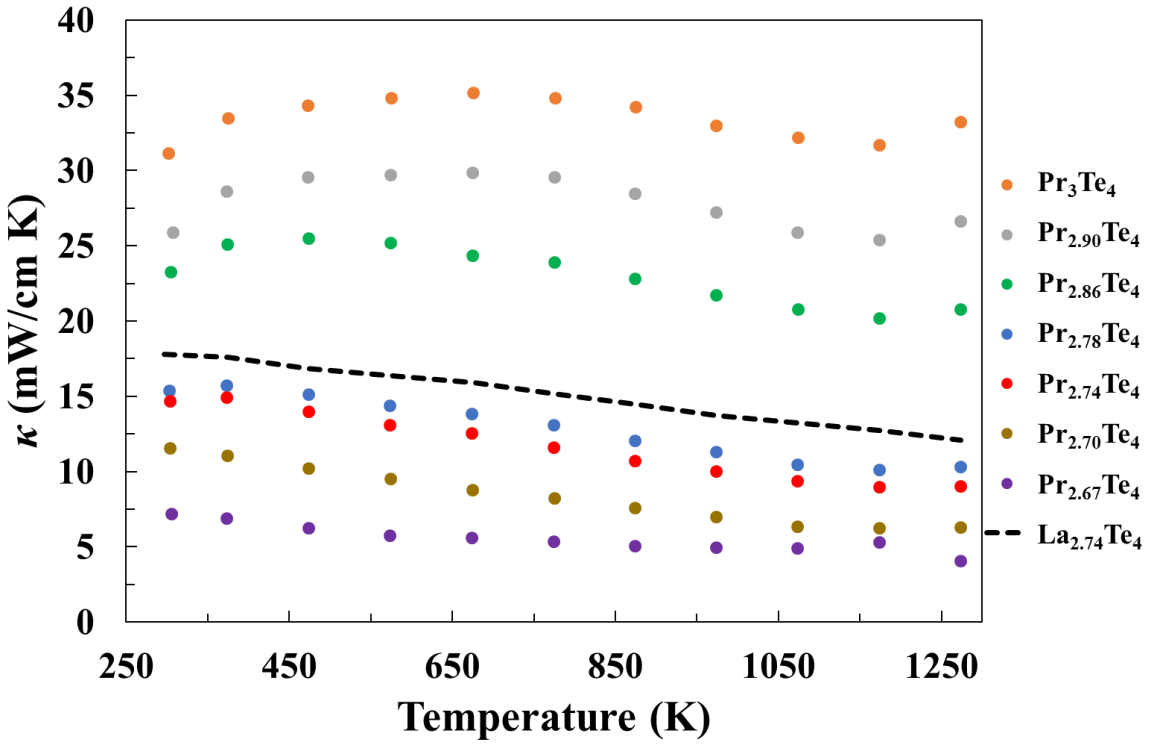

Figure 4.16 Total thermal conductivities of $Pr_{3-x}Te_4$ compared to $La_{2.74}Te_4$.[5] The thermal conductivities decrease with increasing vacancy concentration due to reductions in carrier concentration. $Pr_{2.74}Te_4$ exhibited a 25% reduction in thermal conductivity compared to $La_{2.74}Te_4$.

When samples with equivalent vacancy concentrations were compared, it was found that $Pr_{3-x}Te_4$ samples exhibited a significantly lower thermal conductivity than $La_{3-x}Te_4$. To determine whether the decrease was due to changes in the electronic or lattice contributions, the lattice thermal conductivities were calculated. The lattice thermal conductivity was found by first calculating the electronic contribution using the Wiedemann-Franz law, $\kappa_e = L\sigma T$, where L is the Lorenz number, σ is the electrical conductivity, and T is the absolute temperature. The electronic contribution was then subtracted from the total thermal conductivity. A changing Lorenz number

was used, which was calculated as a function of Seebeck coefficient using the approximation $L = 1.5 + \exp(-|S|/116)$, resulting in Lorenz numbers between 1.5–2.2 x 10^{21} W Ω K^{-1}. [31]

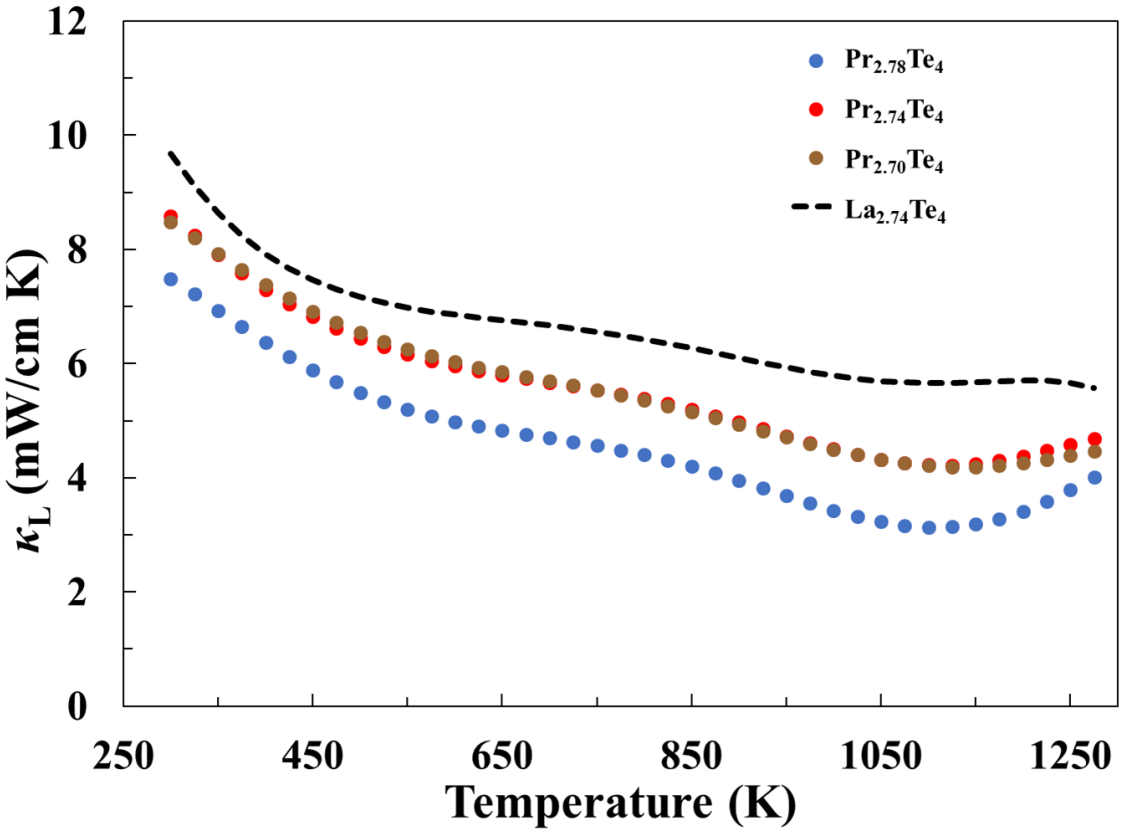

Figure 4.17 Lattice thermal thermal conductivities calculated using the Wiedemann-Franz law. The lattice thermal conductivity of $La_{2.74}Te_4$ is shown for comparison.[5] $Pr_{3-x}Te_4$ samples with higher carrier concentrations were omitted due to strong deviation from the Wiedemann-Franz law.

Figure 4.17 shows the calculated lattice thermal conductivities for samples with vacancy concentrations similar to $La_{2.74}Te_4$. The intrinsically low lattice thermal conductivities result from the complexity of the Th_3P_4 structure, which promotes substantial Umklapp scattering of acoustic phonons.[34] The lattice thermal conductivities for the $Pr_{3-x}Te_4$ samples were similar to one another and lower than that calculated for $La_{2.74}Te_4$ from room temperature to 1275 K. To

investigate the origin of the reduced κ_L in $Pr_{3-x}Te_4$, the elastic moduli and sound velocities of both $La_{2.74}Te_4$ and $Pr_{2.74}Te_4$ were measured from room temperature up to 573 K. The elastic moduli $Pr_{2.74}Te_4$ was found to be slightly lower than $La_{2.74}Te_4$. Combined with the higher density of $Pr_{2.74}Te_4$, this led to a small decrease in the speed of sound (Figure 4.18), which is consistent with the lower κ_L.

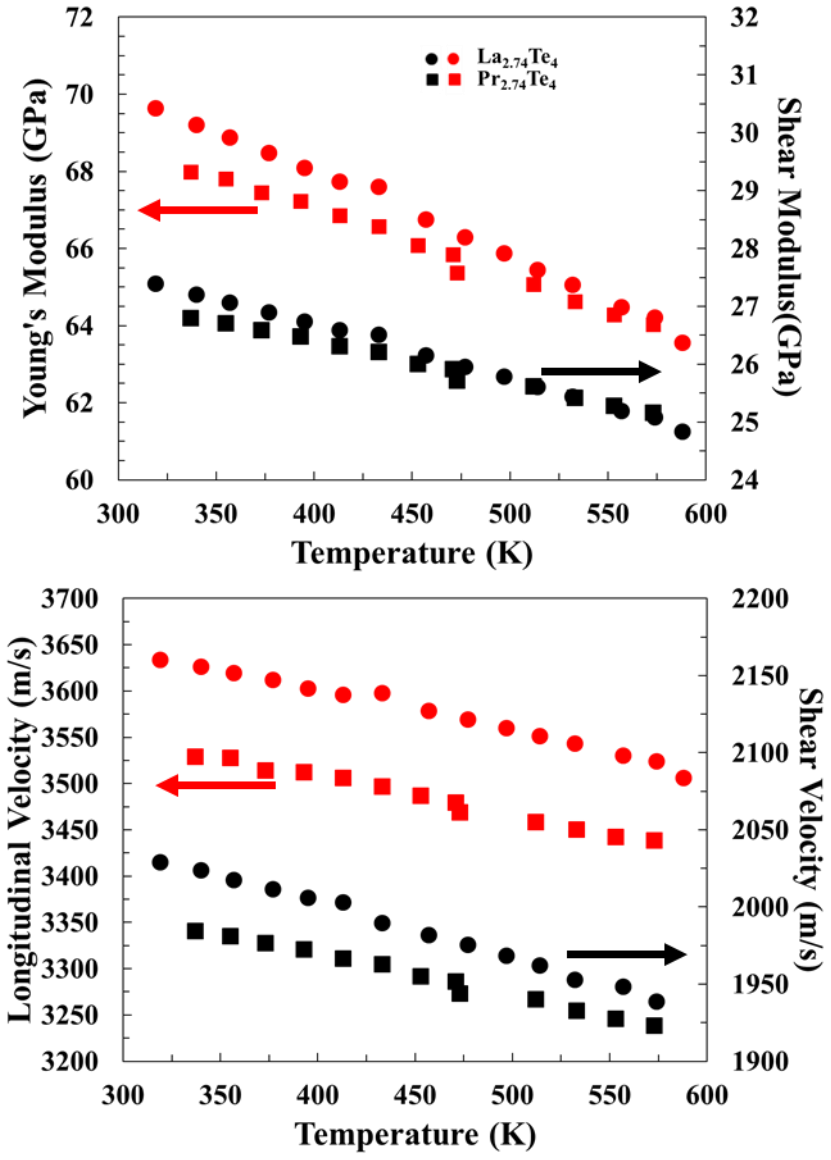

Figure 4.18. Temperature dependent elastic moduli (top) and speed of sound measurements (bottom) of $La_{2.74}Te_4$ and $Pr_{2.74}Te_4$.

ZT increased with increasing vacancy concentration until $x = 0.26$, and then began to decrease (Figure 4.19). A peak *ZT* of 1.7 at 1200 K was achieved for $Pr_{2.74}Te_4$, representing a 50% improvement over the optimized *ZT* of 1.1 reported for $La_{3-x}Te_4$.[5] The improvement to *ZT* resulted from the large increase in the Seebeck coefficient from the electronic states introduced by the *4f* electrons in addition to decreased lattice contributions, which lowered the total thermal conductivity. Propagated error in *ZT* was calculated to be 30%.

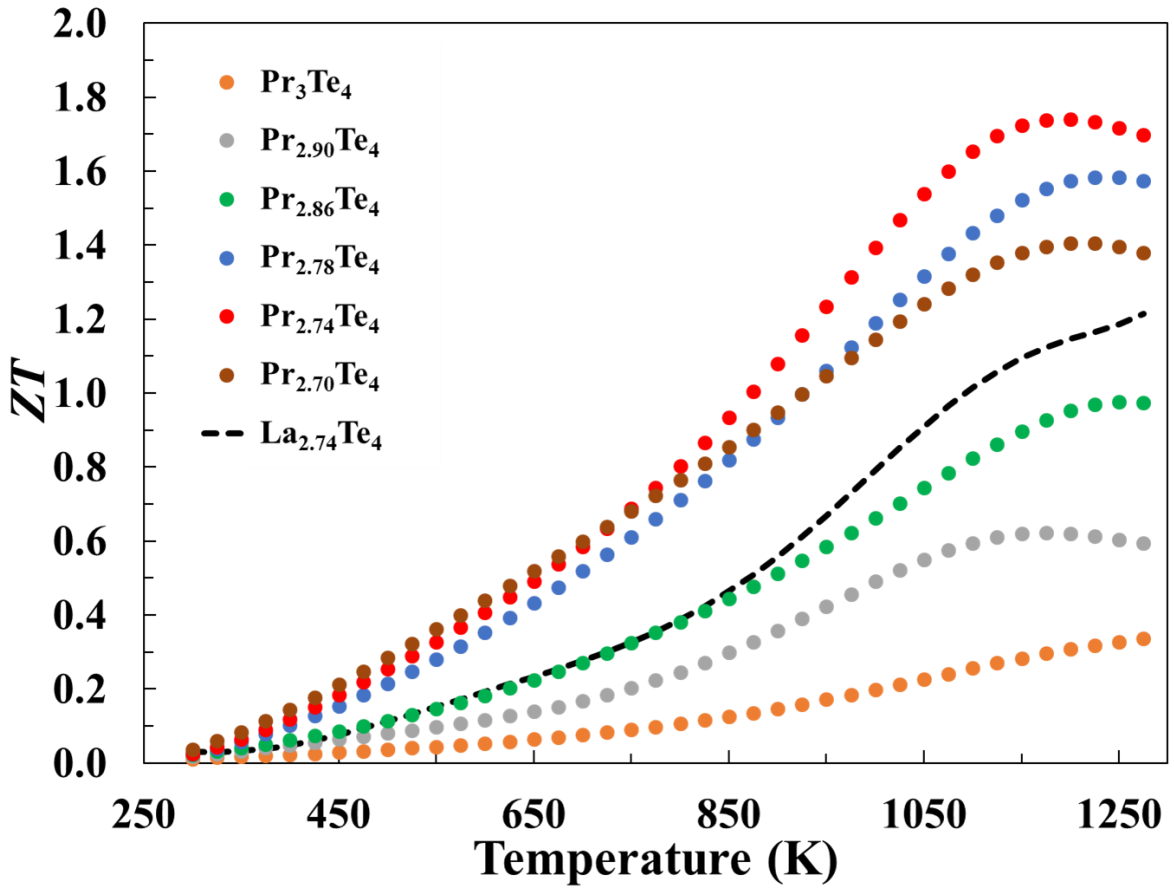

Figure 4.19 Temperature-dependent thermoelectric figure of merit as a function of temperature. The optimized *ZT* for $La_{3-x}Te_4$ is shown for comparison.[5] *ZT* was optimized with a vacancy concentration of $x = 0.26$, achieving a peak value of 1.7 at 1200 K. A 30% error in *ZT* was calculated.

4.6. Conclusions

Density functional theory was used to calculate the density of states and energy band diagram for Pr_3Te_4. It was found that the 4*f* electrons of Pr cause a sharp increase in the density of states near the conduction band edge when compared to $La_{3-x}Te_4$. The increase in the density of states was predicted to improve the Seebeck coefficient of $Pr_{3-x}Te_4$. A series of $Pr_{3-x}Te_4$ samples with varying vacancy concentrations were successfully synthesized using mechanochemical methods. The stoichiometry and phase purity were analyzed through a combination of wavelength dispersive X-ray spectroscopy, BSE SEM, and X-ray diffraction. The electronic and thermal properties were measured and $Pr_{3-x}Te_4$ exhibited a 25% improvement in the Seebeck coefficient over $La_{3-x}Te_4$ at higher vacancy concentrations. Additionally, $Pr_{3-x}Te_4$ was found to have decreased thermal conductivity due to a smaller lattice contribution than $La_{3-x}Te_4$. The increased Seebeck coefficient and reduced thermal conductivity resulted in a peak *ZT* of 1.7 at 1200 K. The successful theoretical prediction and experimental verification of the modified band structure of $Pr_{3-x}Te_4$ due to the *4f* electrons suggests that further improvements can be made by incorporating other rare earth elements.

4.7. References

[1] A. F. May, D. J. Singh, and G. J. Snyder, *Phys. Rev. B,* **2009**, *79*, 153101.

[2] G. D. Mahan and J.O. Sofo, *Proc. Natl. Acad. Sci.*, **1996**, *93*, 7436.

[3] Y. Pei, X. Shi, A. LaLonde, H. Wang, L. Chen, and G. J. Snyder, *Nature,* **2011**, *473*, 66.

[4] T. Vo, P. von Allmen, C. K. Huang, J. Ma, S. Bux, and J-P. Fleurial, *Jour. App. Phys.*, **2014**, *116*, 133701.

[5] A. F. May, J-P. Fleurial, and G. J. Snyder, *Phys. Rev. B*, **2008**, *78*, 125205.

[6] A. F. May, S.K. Bux, J.-P. Fleurial, and G. J. Snyder, Private communication, **2016**.

[7] C. Wood, *Rep. on Prog. in Phys.*, **1988**, *51*, 459.

[8] K. A. Gschneidner, J. F. Nakahara, B. J. Beaudry, and T. Takeshita, *Mat. Res. Soc. Symp. Proc.*, **1987**, *97*, 359.

[9] L. R. Danielson, V. Raag, and C. Wood, in *Intersociety Energy Conversion Engineering Conference*, Miami, FL, **1985**, 531.

[10] A. A. Eliseev, E. I. Yarembash, Y. G. Kuznetsov, E. S. Vigileva, A. A. Reshchikova, and L. I. Anotonoa, *Russ. J. Inorg. Chem.*, **1964**, *9*, 482.

[11] T. H. Ramsey, H. Steinfink, and E. J. Weiss, Inorg. Chem.**, 1965**, *4*, 1154.

[12] S. Baroni, *et al*. *The PWSCF code*, **2012**, http://www.pwscf.org.

[13] W. Kohn and L.J. Sham, *Phys. Rev.*, **1965**, *140*, A1133.

[14] J.P. Perdew, K. Burke, M. Ernzerhof, *Phys. Rev. Lett.* **1996**, *77*, 3865.

[15] V. I. Anisimov, J. Zaanen, and O. K. Andersen, *Phys. Rev. B*, **1991**, *44*, 943.

[16] V. I. Anisimov et al., *Phys. Rev. B,* **1993**, *48*, 16929.

[17] M. Cococcioni and S. de Gironcoli. *Phys. Rev. B,* **2005**, *71*, 035105.

[18] N.A.W. Holzwarth, A.R. Tackett and G.E. Matthews, *Comput. Phys. Commun.*, **2001**, *135*, 329.

[19] A.R. Tackett, N.A.W. Holzwarth and G.E. Matthews, *Comput. Phys. Commun.*, **2001**, *135*, 348.

[20] Tumbleston, J., *et al*, *ATOMPAW* (http://users.wfu.edu/natalie/papers/pwpaw/man.html)

[21] N. Marzari, D. Vanderbilt, A. D. Vita, and M. C. Payne, *Phys. Rev. Lett.*, **1999**, *82*, 3296.

[22] A.Z. Morozkin et. al, *Intermetallics*, **2011**, *19*, 1794.

[23] N. W. Ascroft and N. D. Mermin, *Solid State Physics*, Harcourt College Publisher, NewYork, 1976.

[24] A.F. May, D. Signh, and J. Snyder, Phys. Rev. B 79, 153101 (2009).

[25] N. F. Mott and H. Jones, *The Theory of the Properties of Metals and Alloys*, The Clarendon Press, Oxford, UK, 1936.

[26] B.H. Toby and R.B. Von Dreele, *Journal of Applied Crystallography*, **2013**, *46*, 544.

[27] R.G. Mitarov, V.V. Tikhonov, L.N. Vasil'ev, A.V. Golubkov, I.A. Smirnov, *Phys. Status Solidi A*, **1975**, *30*, 457.

[28] K. A. Borup, E. S. Toberer, L. D. Zoltan, G. Nakatsukasa, M. Errico, J. P. Fleurial, B. B. Iversen and G. J. Snyder, *Rev. Sci. Instrum.*, **2012**, *83*, 123902.

[29] C. Wood, D. Zoltan and G. Stapfer, *Rev. Sci. Instrum.*, **1985**, *56*, 719.

[30] R.G. Mitarov, V.V. Tikhonov, L.N. Vasil'ev, A.V. Golubkov, I.A. Smirnov, *Phys. Status Solidi A*, **1975**, *30*, 457.

[31] E.I. Yarembash, A.A. Eliseev, E.S. Vigileva, and L.I. Antonova, *Inorg. Chem.*, **1967**, *3*.

[32] W. L. Cox, H. Steinfink, and W. F. Bradley, *Inorg. Chem.*, **1966**, *5*.

[33] H.-S. Kim, Z. M. Gibbs, Y. Tang, H. Wang and G. J. Snyder, *APL Mater*., **2015**, *3*, 041506.

[34] J. M. Ma, *Improving the Mechanical Strength and Power Conversion Efficiency of High Temperature Thermoelectrics*, Doctoral Dissertation, University of California, Los Angeles, **2014**

[35] R. G. Mitarov, L. S. Parfen'eva, V. V. Popov, and I. A. Smirnov, *Physics of the Solid State*, **2000**, *42*, 12

Chapter 5: Conclusions and Future Work

5.1. $La_{3-x}Te_4$-Ni Composites

The first topic examined in this work was the role of Ni inclusion size on the CAFE mechanism in $LaTe_{1.46}$-Ni composites. The starting Ni particle size was varied from tens of nanometers to hundreds of microns in diameter and combined with $LaTe_{1.46}$ at an equivalent volume fraction of 15%. The addition of 2.2-3 μm Ni and 150-300 μm Ni particles to $LaTe_{1.46}$ caused the largest decreases in resistivities compared to previous composites, but also had decreased Seebeck coefficients. 5-15 μm Ni had little effect on resistivity resulting in similar values as $LaTe_{1.46}$, but did increase the Seebeck coefficient slightly. The 80-150 nm Ni decreased the resistivity slightly compared to $LaTe_{1.46}$ but increased the Seebeck coefficient by 20%. The thermal conductivities of the 2.2-3 μm and 150-300 μm samples were similar to the baseline composite, but the 5-15 μm and 80-150 nm samples had decreased thermal conductivities below that of $LaTe_{1.46}$. The decrease in thermal conductivity for the 80-150 nm sample is attributed to increased phonon scattering as a result of the much smaller inclusions present only in this sample. The change in properties due to altering the starting particle size of the Ni ultimately resulted in a 66% increase in *ZT* for the 80-150 nm Ni composite, with a peak *ZT* of approximately 1.9 at 1250 K.

Further work is still required to optimize the reduction of the surface oxide on the Ni particles of all sizes, as the oxide layers on each particle may require longer reduction treatments. 15 vol% nickel was used in this study as that loading fraction was identified by Ma, et al., to optimize the thermoelectric properties of the initial $LaTe_{1.46}$-Ni composites.[1] As the properties of the composites differed significantly depending on the starting Ni particle size, optimization of

the volume fraction of nickel for each size should be conducted. Additionally, the role of morphology should be investigated by synthesizing composites with nickel fibers, as fibers have been shown to reduce the volume fraction required for the onset of percolation.[2]

5.2. $La_{3-x}Te_4$-Co Composites

Chapter 3 detailed the investigation of $LaTe_{1.46}$-Co composites to observe if cobalt could be used instead of nickel for the CAFE mechanism. A series of composites with 0-15 vol% cobalt were synthesized and their thermoelectric properties were investigated. The microstructures of the cobalt composites were found to be less homogeneous than the $LaTe_{1.46}$-Ni composites, with segregation between Co-rich and Co-deficient areas as observed through SEM. High-temperature resistivity measurements were conducted and the composites had an increased resistivity values compared to $LaTe_{1.46}$ until 15 vol%. The Seebeck coefficients of the composites were found to be larger than that of the parent material. An 18% improvement in Seebeck was observed between 5-8 vol% cobalt, after which the Seebeck began to decrease above 10 vol% Co. The combination of increased resistivity and Seebeck suggested a reaction was occurring which altered the carrier concentration on the $LaTe_{1.46}$ matrix. An oxide coating on the surface of the cobalt powder is hypothesized to be responsible. Thermal conductivity increased with increasing cobalt concentration above 8 vol%. The *ZT* of all composites except the 15 vol% sample had peak values similar to or greater than that of $LaTe_{1.46}$ due to the increased Seebeck coefficients of the composites. The 5 vol% composite exhibited the greatest increase in *ZT*, achieving a value of 1.5 at 1225 K, representing a 25% improvement over $LaTe_{1.46}$.

The dissimilarities in the microstructures between the cobalt and nickel composites is currently being investigated. The interfaces between both inclusions and the $LaTe_{1.46}$ matrix are being studied using high-resolution transmission electron microscopy (HRTEM) to observe any differences. Additionally, HRTEM of the interfaces will be used to investigate if an oxide layer is present between the cobalt inclusions and $LaTe_{1.46}$. Using lessons learned from the nickel composites in Chapter 2, a study will be conducted where the cobalt powder is first pre-treated to remove the surface oxide and then incorporated into $LaTe_{.146}$ matrix to observe any effects on their thermoelectric properties.

5.3. $Pr_{3-x}Te_4$

The final chapter of this work evaluated the thermoelectric performance of the $Pr_{3-x}Te_4$ system. DFT calculations were performed which showed a sharp peak in the DOS of Pr_3Te_4 near the Fermi level compared to La_3Te_4. This peak is the result of the 4*f* valence electrons of praseodymium, which are absent in lanthanum. The presence of the peak in the DOS was expected to increase the Seebeck coefficient of $Pr_{3-x}Te_4$ over $La_{3-x}Te_4$, possibly enhancing *ZT*. $Pr_{3-x}Te_4$ samples were synthesized with x = 0, 0.1, 0.14, 0.22, 0.26, 0.3, and 0.33 and the thermoelectric transport properties were measured. Increasing the vacancy concentration increased the resistivity and Seebeck coefficient, while decreasing the thermal conductivity, as expected. $Pr_{3-x}Te_4$ samples between x = 0 and 0.14 had electronic properties similar to that of $La_{3-x}Te_4$ with equivalent vacancy concentrations. $Pr_{3-x}Te_4$ samples with vacancy concentrations greater than x = 0.14 exhibited increased resistivities and Seebeck coefficient values compared to the optimized $La_{2.74}Te_4$. The thermal conductivities of samples with vacancy concentrations of x > 0.14 were significantly lower than $La_{2.74}Te_4$ due to a decreased lattice contribution. The

thermoelectric performance of this system optimized $x = 0.26$, with a ZT value of 1.7 as a result of the increased Seebeck coefficient and lower thermal conductivity.

The origins of the lower thermal conductivity of $Pr_{3-x}Te_4$ compared to $La_{3-x}Te_4$ are not yet understood and are currently under investigation at the Jet Propulsion Laboratory. For $Pr_{3-x}Te_4$ to be integrated into future extraterrestrial power sources, the thermomechanical properties will need to be evaluated in addition to its temporal stability at elevated temperatures. Finally, the CAFE mechanism discussed in Chapters 2 and 3 will be applied to $Pr_{3-x}Te_4$ to enhance its thermoelectric and mechanical properties.

5.4. References

[1] J. M. Ma, *Improving the Mechanical Strength and Power Conversion Efficiency of High Temperature Thermoelectrics*, Doctoral Dissertation, University of California, Los Angeles, **2014**

[2] B. Bridge, *Jour. of Mat. Sci. Let,* **1989**, *8*, 102